2-1-2014

Towards efficient photoanodes for solar fuel production

Basamat Saif El Din Shaheen

The American University in Cairo

The Graduate School

Nanotechnology Program

TOWARDS EFFICIENT PHOTOANODES FOR SOLAR FUEL PRODUCTION

A Thesis in
Nanotechnology

by

Basamat Saif el Din Shaheen

Submitted in Partial Fulfillment
of the Requirements
for the Degree of Masters of Science in Nanotechnology

January 2014

ABSTRACT

The solar energy conversion efficiency is a materials-limited process as there is always a trade-off between the light absorption capability of the material and its stability. For solar hydrogen production, for example, wide-bandgap semiconductors are stable but only absorb in the UV region of the light spectrum. Small-bandgap semiconductors, on the other hand, are not stable in aqueous electrolytes. In this thesis, two metal oxide-based photoanode systems were studied in an attempt to find a balance between their optical and photocatalytic properties as well as their stability.

In the first part of the thesis, one-dimensional TiO_2 nanotubes/ZnO core-shell nanostructured electrodes were investigated. Increasing the ZnO shell thickness resulted in different morphological, structural and optical characteristics. The crystallinity of the core nanotubes was found to be a determinant factor in the formation of the TiO_2/ZnO heterojunctions as revealed by the FESEM, GAXRD, XPS and Raman analyses. The TiO_2/ZnO heterojunction showed almost 80% increase in the photoconversion efficiency (7.3%) compared to pure TiO_2 (4.1%) under UV illumination (320-400 nm, 100 mW/ cm^2, 0.5 M Na_2SO_4). The main reasons responsible for the observed enhancement in the photoactivity were discussed.

In the second part of the thesis, Nb_2O_5 – based photoanodes were investigated. The fabrication of Nb_2O_5 ordered structures (nanopores, nanorods, nanochannels and microcones) is achieved by a simple electrochemical method. The microcone structure was the most stable morphology and showed higher absorption ($\lambda \cong 450$ nm) compared to other structures ($\lambda \cong 380$ nm). An *in-situ* approach for the direct synthesis of crystalline Nb_2O_5 microcones at room

temperature is demonstrated for the first time. Also, the successful formation of niobium oxynitride microcones is achieved for the first time as confirmed via XPS, XRD and Raman spectroscopy measurements. The fabricated NbON microcones showed exceptional optical properties with an absorption profile extending to 770 nm.

The thesis of Basamat Saif el Din Shaheen was reviewed and approved*by the following:

Nageh K. Allam
Assistant Professor, The American University in Cairo.
Director, Energy of Materials Laboratory (EML).
Thesis Advisor
Chair of Committee

Hanadi G. Salem
Professor, Materials and manufacturing area, Department of Mechanical Engineering.
Director, Nanotechnology Graduate Program, The American University in Cairo.
Thesis Co-Advisor

Mohamed Serry
Assistant Professor, Department of Mechanical Engineering, The American University in Cairo.

Iman Taha
Associate Professor, Design and Production Engineering Department, Faculty of Engineering, Ain Shams University.

Wael Mamdouh
Assistant Professor, Departement of Chemistry, The American University in Cairo.
Thesis Moderator.

*Signatures are on file in the Graduate School.

TABLE OF CONTENTS

LIST OF FIGURES

LIST OF TABLES

ACKNOWLEDGEMENTS

I would like to express my deep gratitude to my advisor, Dr. Nageh Allam for being a role model to me not only in science but more important on the personal level. On the science level, he was always caring to guide me to develop my skills and experience. He was always updating me by the recent research and opportunities that could improve my understanding and my future career. On the personal level, I learned a lot from his ethics, humility and dedication. Jazak ALLAH Khair for everything, I owe you a lot.

I am also indebted to Dr. Hanadi Salem for accepting to guide me since I was working with her as undergraduate student in my senior project. She helped me to gain practical experience on mechanical fabrication methods. She has also guided me to join the nanotechnology masters program. I would like to thank the members of my thesis committee, Dr. Mohamed Serry, Dr. Iman Taha and Dr. Wael Mamdouh for their gracious participation and for their constructive criticism.

I would like to thank all the members of the Energy Materials Lab for being very helpful and supportive. They taught me the true meaning of a team work that is rare to happen.

The collaboration and the hosting of Dr. Mostafa El Sayed from Georgia Institute of Technology and Dr. Sossina Haile from California Institute of Technology are gratefully acknowledged. They kindly provided me with all the facilities they have in their labs to do some parts of the fabrication and characterization. Financial support from The American University in Cairo is also gratefully acknowledged.

Finally, I owe special gratitude to my parents, my sisters and brothers, my school teachers and my friends for their continuous and unconditional help and support. Special thanks to Nourhan Mahmoud, Asmaa Gamal, Huda Alaa, Mohamed Hamouda, Ali Abdel Hafiz, Ahmad Amer and all the members and students of IHYAA Academy.

DEDICATION

{ قُلْ إِنَّ صَلَاتِي وَنُسُكِي وَمَحْيَايَ وَمَمَاتِي لِلَّهِ رَبِّ الْعَالَمِين }

"Verily, my *Salat* (prayer), my sacrifice, my living, and my dying are for Allah, the Lord of the *'Alamin* (mankind)"

The Noble Qur'an, Surat Al - An'am, Verse [126]

Chapter 1

Introduction and Scope of the Thesis

1.1 Energy Challenge

Energy is the backbone of civilization and a key element in defining the living standards in nations. The industrial revolution in the 18th and 19th centuries was powered by the transition from wood to coal energy. Moreover, the ongoing technological development that started from the 20th century till now is powered by the energy shift from solid coal to liquid petrol. However, the world is currently facing one of its greatest challenges by experiencing depletion of fossil fuels. Being dependant mainly on the support of fossil fuels for years creates the world's energy challenge with three main aspects [1]:

1. **The depletion of fossil fuels is going fast**

It is estimated that the world can have about 150 to 400 years of coal and 40 to 80 years for oil and 60 to 160 years of natural gas [2]. However, increasing the world population and the energy demands for high standard living shortens the time over which fossil fuels can last. In terms of cost, it is clearly observed that the prices of energy are increasing such that they became unaffordable in many countries.

2. **The oil wars**

Nations always have fight wars over needed resources as water and food. The same holds for energy resources, the world has seen several wars in the oil-rich countries that cost many lives for the sake of controlling the dwindling pile of fossil fuels until they vanish.

3. Environmental pollution

Burning fossil fuels is accompanied by several sources of pollution. Approximately, 80 % of the produced carbon dioxide comes from burning fossil fuels. Carbon dioxide (CO_2) is a greenhouse gas that traps heat emitted by earth. The increase in the concentration of CO_2 is consequently coupled with increase in earth's average temperature that has its dangerous impacts on the rise of sea levels and the expansion of subtropical deserts. In addition, other pollutants including cadmium, mercury, arsenic, nitrogen oxides, sulfur, and beryllium vapors are emitted with the combustion of fossil fuels.

This energy situation was firstly referred to as the *Terawatt challenge* in 1992 by Professor Rick Smalley, winner of Nobel Prize in chemistry [2]. This study directed the world towards searching for renewable sources of energy to replace the existing sources of fossil fuels. It was concluded by recent studies that this is the way of facing the energy challenge as shown in **Figure 1-1**. The renewable sources need to possess various factors to be as efficient as fossil fuels; importantly having high energy density, being safe, portable and easily stored. In addition, they need to be clean to limit the pollution hazards that the world is facing nowadays. Solar radiation, wind, geothermal and waves are examples of renewable and clean sources of energy. However, the sun is the ultimate renewable source as it gives energy of 3×10^{24} joules/ year to the earth, which is about 10,000 times the current energy consumption of the whole world [1]. **Figure 1-2** shows the amount of the energy that can be supplied by the renewable and non-renewable sources of energy to fulfill the world's demand in 2050.

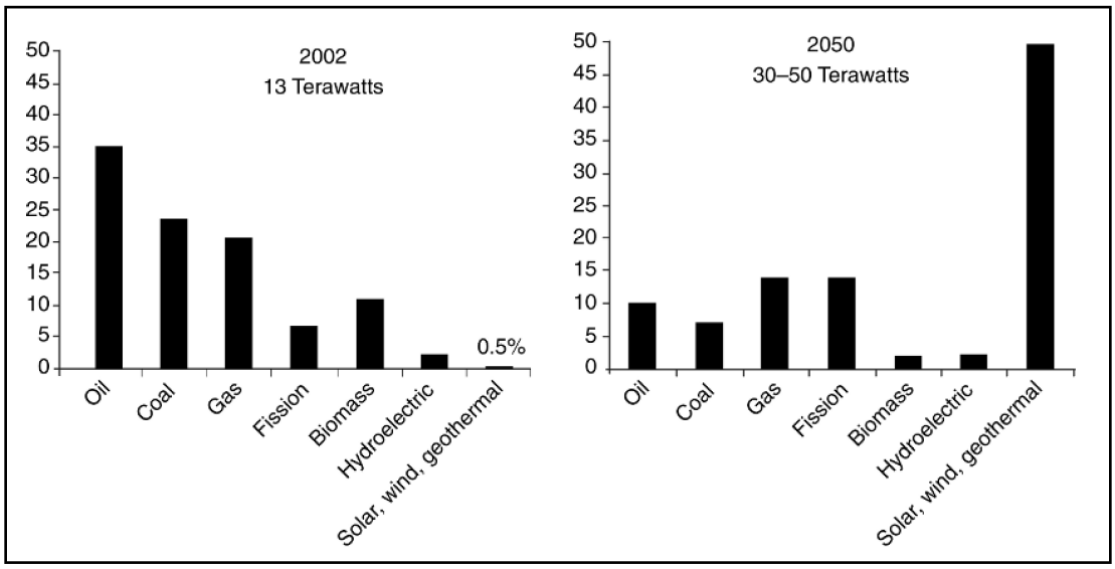

Figure 1-1: The terawatt renewable energy challenge; the energy mix has to switch from the panel on the left to the panel on the right to cap CO_2 levels at safe limits [3].

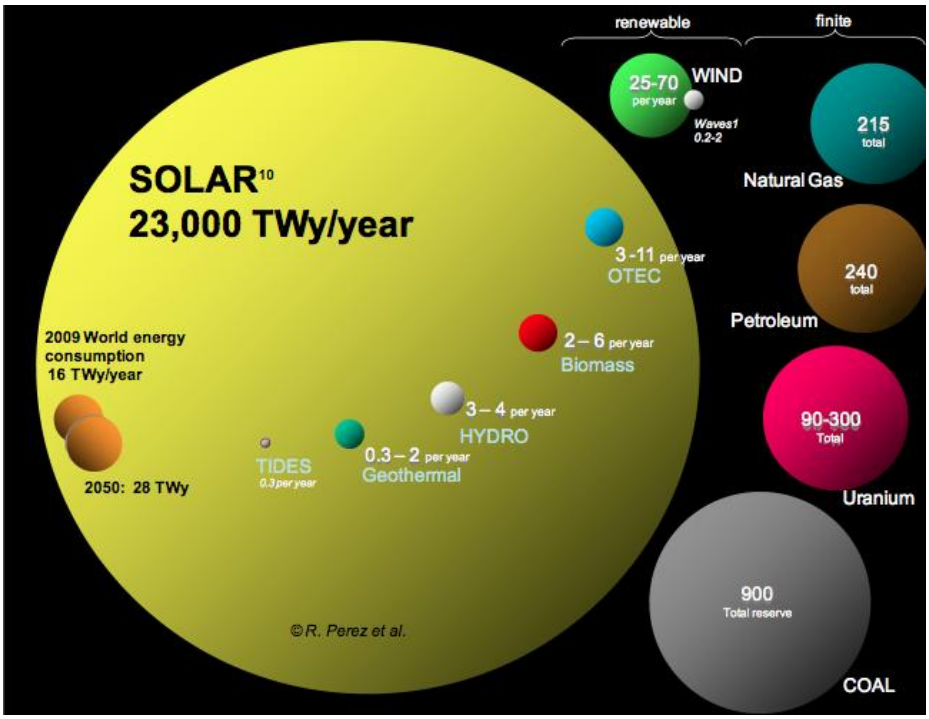

Figure 1-2: Comparison of the amount of energy that can be supplied from the various sources compared to the energy demand in year 2050 [4].

1.2 Hydrogen Fuel

Hydrogen (H) is the simplest of atoms consisting of one proton and one electron. As an atom, hydrogen is very reactive to form molecular pairs (H_2). It is the most abundant element in the universe and the third most abundant in earth. It forms a combustible mixture when being mixed with an oxidant as air. Like electricity, hydrogen is not a primary source of energy as its production require energy, however it is an energy carrier. A very attractive property of hydrogen as a fuel is that it has the highest energy content per unit mass of any fuel. For example, on a weight basis, hydrogen has nearly three times the energy content of gasoline (141.6 MJ/kg versus 47.3 MJ/kg) as shown in **Table 1-1**.

Table 1-1: Comparison of hydrogen to other fuels [1]

Fuel	LHV (MJ/kg)	HHV (MJ/kg)	Stoichiometric Air/Fuel Ratio (kg)	Combustible Range (%)	Flame Temperature (°C)	Min. Ignition Energy (MJ)	AutoIgnition Temperature (°C)
Methane	50.0	55.5	17.2	5–15	1914	0.30	540–630
Propane	45.6	50.3	15.6	2.1–9.5	1925	0.30	450
Octane	47.9	15.1	0.31	0.95–6.0	1980	0.26	415
Methanol	18.0	22.7	6.5	6.7–36.0	1870	0.14	460
Hydrogen	119.9	141.6	34.3	4.0–75.0	2207	0.017	585
Gasoline	44.5	47.3	14.6	1.3–7.1	2307	0.29	260–460
Diesel	42.5	44.8	14.5	0.6–5.5	2327		180–320

Hydrogen is required for many applications as shown in **Figure 1-3**. In the application of transportation, hydrogen is more attractive than electricity [5]. That is because it can be more easily stored and transported in gaseous, liquid or metal hydride forms. It is utilized directly in vehicles by fuel cells producing water as the only byproduct with the least emissions of CO_2 compared to other fuels as shown in **Figure 1-4**.

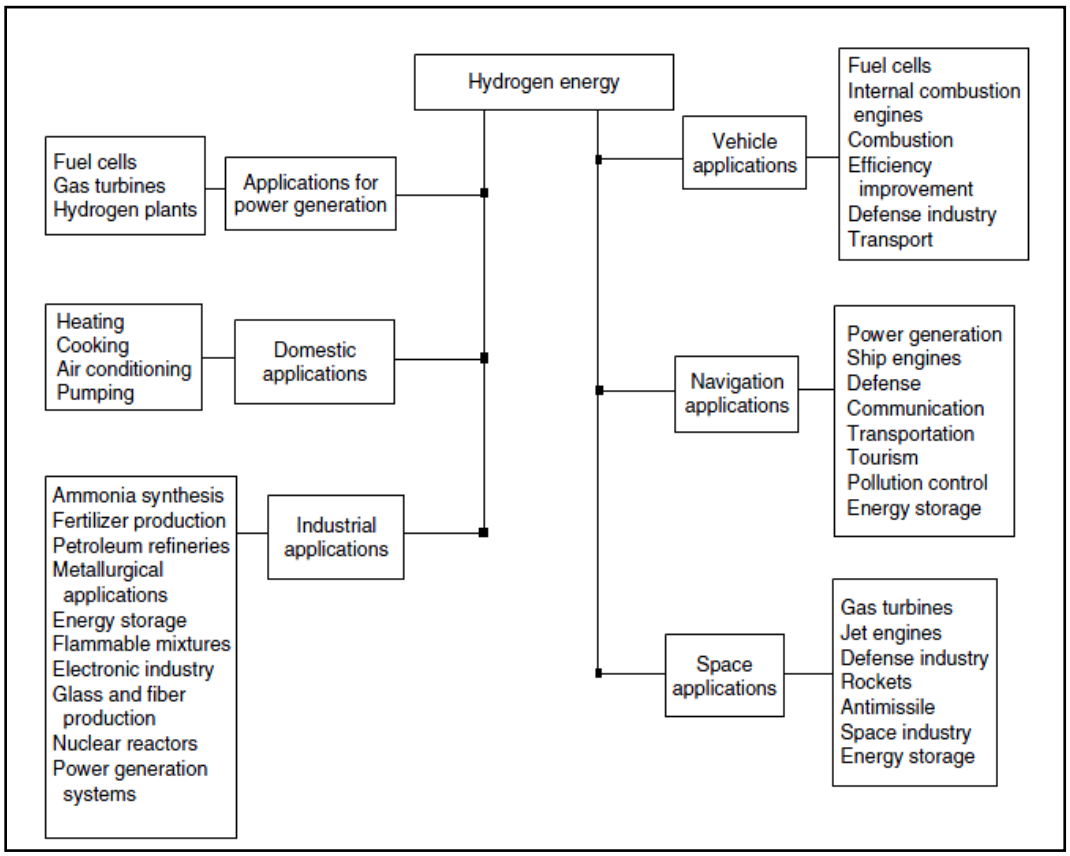

Figure 1-3: Application areas of hydrogen [6].

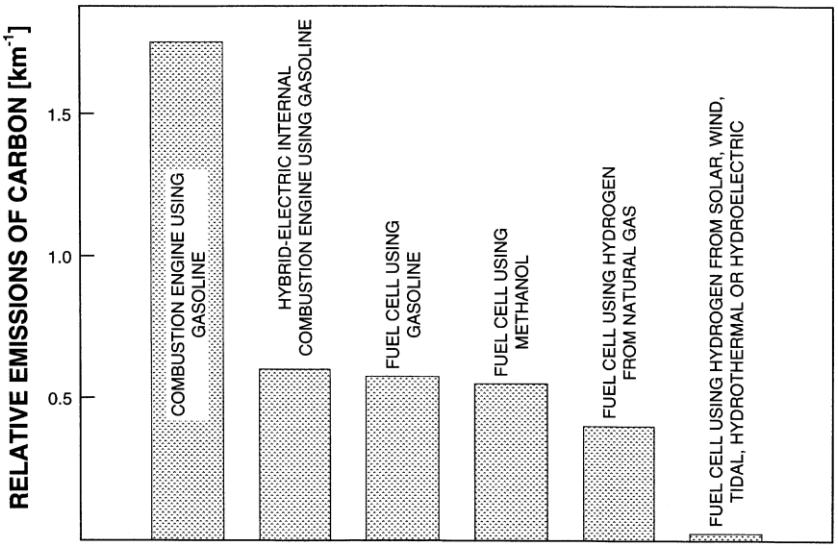

Figure 1-4: Relative emission of carbon units per km for vehicles powered by today's internal combustion engine using gasoline compared to vehicles powered by fuel cells [7].

There are various methods to produce hydrogen that have being used for decades [8]. It can be produced from fossil fuels through chemical conversion of hydrocarbons and from nuclear energy. However, these methods will not be effective as they depend on non-renewable sources. On the other hand, hydrogen can be produced from renewable sources such as biomass. However, this method is accompanied by CO_2 emissions similar to the fossil fuel pathway. Therefore, hydrogen can be only considered a renewable, environmentally-friendly fuel and an ideal energy carrier if it is produced from clean and renewable source of energy. There is a large body of literature confirming that the solar energy route for hydrogen production is the most promising one to pursue, as it will be explained in the following section [9].

1.3 Hydrogen from Solar - Water Splitting

Solar energy is presently converted into electricity and heat using devices such as solar cells (photovoltaics) or black absorbers (solar thermal energy). Other way for solar energy harvesting is to convert it into chemical fuels. Water is the most abundant source of hydrogen on the planet. However, hydrogen is strongly bonded to oxygen and a minimum energy of 1.229 eV (at 25°C, 1 bar) is required for splitting water into hydrogen and oxygen. Electrolysis of water to generate hydrogen and oxygen has a history of more than 200 years [9]. It is the simplest of all the water-splitting techniques and comparatively efficient. The net reaction is:

$$H_2O \text{ (liquid/vapor)} + \text{electrical energy} \rightarrow H_2\,(g) + \tfrac{1}{2}\,O_2\,(g) \qquad (1.3.1)$$

Here comes the challenge to get the energy needed, or part of it, from a renewable energy source. By fact, solar energy is the largest carbon-free resource amongst the other renewable energy sources. Therefore, solar energy coupled with electrolysis, solar water photoelectrolysis, appear to be the most logical solution pathway. In 1990, the world's first solar-powered hydrogen production plant became operational, at Solar-Wasserstoff-Bayern, a research and testing facility in southern Germany.

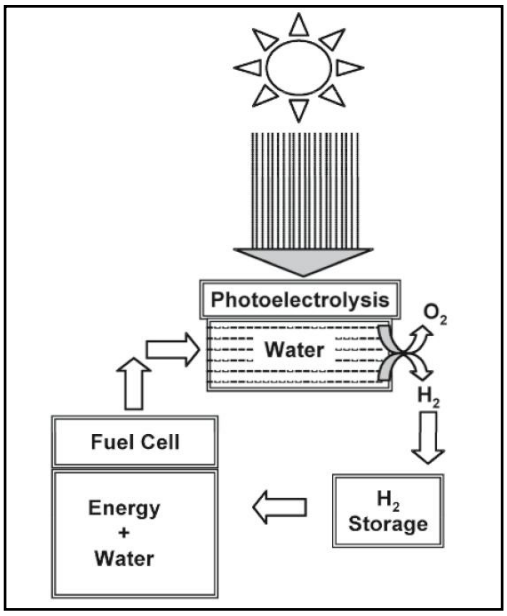

Figure 1-5: Solar hydrogen production via photoelectrolysis, with enormous potential for providing a renewable and clean energy carrier [1].

In a similar methodology, plants naturally make solar-chemical conversion through the photosynthesis process to produce their food. Therefore, solar water – splitting for hydrogen production is termed *artificial photosynthesis* as shown in **Figure 1-6**. Water is transparent to the wavelengths constituting the solar spectrum. Therefore, photocatalytic or photoelectrochemical splitting of water requires an agent (semiconductor, dye, or chromophore) capable of first absorbing sunlight and generating electron-hole pairs. Honda and Fujishima in 1972 firstly reported the concept of

photoelectrochemical cells (PEC) using titanium dioxide (TiO_2) as photoanode and platinum (Pt) as a cathode immersed in aqueous electrolyte [10]. The solar radiation absorbed by TiO_2 results in the evolution of oxygen at the anode and hydrogen at the cathode. The setup of their PEC is shown in **Figure 1-7**. Although TiO_2 showed better stability in aqueous solutions than other semiconductors as silicon (Si) and gallium arsenide (GaAs), the energy conversion efficiency was only 0.1 %. This low efficiency is now understood based on the properties of semiconductors along with the mechanism of the solar-water splitting as will be discussed in chapter 2.

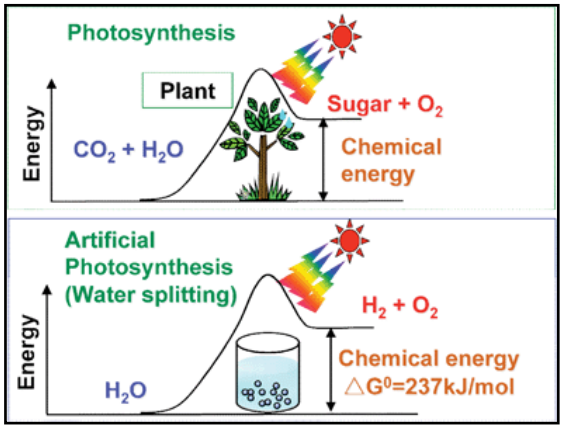

Figure 1-6: Natural and artificial photosynthesis for solar - fuel conversion [11].

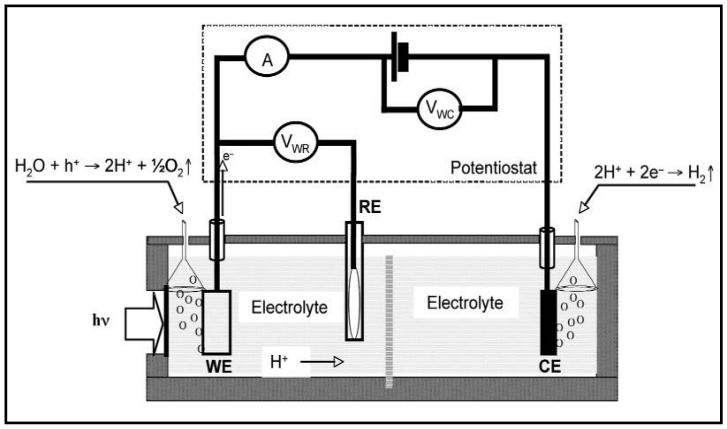

Figure 1-7: Schematic representation of a conventional three-electrode photoelectrochemical cell showing: WE = working electrode, RE = reference electrode, CE = counter electrode. If the working electrode is an n-type semiconductor and the counter electrode is a metal, then oxygen evolution occurs at the WE and hydrogen evolution occurs at the CE [1].

Despite the low efficiency reported by Honda and Fujishima, they opened the doors for more investigations in a new and fascinating to improve the properties of metal oxide semiconductors for hydrogen production via solar-water splitting. This thesis is one of those efforts.

1.4 Scope and Objectives of the Thesis

As it will be explained in chapter 2, enhancing the performance of photoelectrodes for solar-hydrogen conversion through water splitting has two key factors:

(1) Maximizing the light absorption by lowering the band gap.

(2) Minimizing the charge carrier's recombination and promoting fast charge transport.

In wide band gap metal oxide semiconductors, these two factors are usually competitive. With the aim to reach a balance and to understand the effect of structure, morphology and nitrogen doping, two systems were studied: TiO_2 – ZnO heterostructure and Nb-O-N microcones.

Chapter 2 gives an overview of the terminologies used throughout the thesis, such as the concepts of solar radiation, water–splitting reaction and semiconductors in photoelectrolysis.

Chapter 3 reviews the relevant literature on TiO_2-ZnO heterostructures and NbO_2-based systems.

Chapter 4 describes the experimental procedure and conditions used for the preparation and characterization of the studied systems.

Chapter 5 presents the results concerning the TiO_2-ZnO heterostructure based on analysis of the morphology, structure and optical properties. Their photoelectrochemical behavior is also discussed.

Chapter 6 discusses the results concerning the Nb_2O_5–based systems from three aspects: (1) fabrication of different morphologies by anodization process, (2) *in-situ* crystallization during anodization, and (3) the formation of niobium oxynitride materials with enhanced optical properties. The effects of the *in-situ* crystallization and the oxynitride formation on the photoelectrochemical properties in water-splitting are also discussed.

Chapter 7 highlights the important conclusions from the study and suggests some plans for further work.

References

1. Grimes, C. A.; Varghese, O. K.; Ranjan, S. *"Light, Water, Hydrogen"*. Springer: NewYork, USA **2008**.
2. Zini, G.; Tartarini, P. *"Solar Hydrogen Energy Systems Science and Technology for the Hydrogen Economy"*. Springer: Verlag Italia **2012**.
3. Rajeshwar, K.; McConnell, R.; Licht, S. *"Solar Hydrogen Generation. Toward a Renewable Energy Future".* Springer: NewYork, USA **2008**.
4. http://v3solar.com/about-us/market/. Retrieved on the 13th of December 2013.
5. Midilli, A.; Dincer, I.; Rosen, M. A. On hydrogen and hydrogen energy strategies: I: current status and needs. *Renewable Sustainable Energy Rev.* **2005**, 9, 255-271.
6. http://www1.eere.energy.gov/hydrogenandfuelcells/tech_validation/h2_manual.html. Hydrogen fuel cell engines and related technologies, 2001. Retrieved on 13th of December 2013.
7. The Economist Technology, Quarterly, March 25, 2001. p.29.
8. Gupta, R. B. *"Hydrogen Fuel Production, Transport, and Storage"*. CRC Press, USA **2009**.
9. Krol, R.; Gra¨tzel, M. *"Photoelectrochemical Hydrogen Production".* Springer New York, USA, 2012.
10. Fujishima, A. K.; Honda, K. Photoelectrolysis of water using titanium dioxide. *Nature* **1972**, 238, 37738.
11. Kudo, A.; Miseki, Y. Heterogeneous photocatalyst materials for water splitting. *Chem. Soc. Rev.* **2009**, 38**,** 253-278.

Chapter 2

Background

In this chapter, the fundamental background used in the experimental work and the analysis of the results in this thesis is reviewed; including basics about the solar radiation, solar water-splitting reaction and metal oxide semiconductors. The niobium-oxygen system is presented with attention to the structure and the electronic properties of niobium oxides. Finally, concepts about the plasma sputtering technique used for the deposition of thin films are illustrated.

2.1 Solar Radiation

The Sun emits a continuous flow of electromagnetic energy generated by its internal nuclear fusion processes. Solar irradiance (kW/m^2) is the electromagnetic power the earth receives from the sun per unit surface area. Solar radiation (kWh/m^2) represents the electromagnetic energy per unit surface area. The solar radiation spectrum is composed of different wavelengths that are displayed in **Figure 2-1**. The intensity of the solar radiation absorbed by the surface varies depending on the geographical coordinates, the day of the year, the different positions of the sun, the mass of the air through which the radiation travels and the meteorological conditions. Any loss in radiation depends on the thickness of the atmosphere it passes through as it is being absorbed or scattered by air particles and dust. Therefore, in order to properly consider the effect caused by the thickness of the atmosphere through which the solar radiation travels, the Air Mass (AM) index is defined as [1]:

$$AM = P / P_0 \text{ Sin } \theta \qquad [2.2.1]$$

where P is the atmospheric pressure, P_0 is the reference pressure of 0.1013 MPa and θ is the sun's elevation angle with respect to the horizon. For a global reference to be used in laboratory tests, AM is set to be 1.5 corresponding to inclination of the flat absorber surface by an angle of 37^o from the horizon, which corresponds to average conditions in 48 contiguous states of the United States. The standard AM 1.5 spectrum is normalized to give 1000 W/m^2 as radiation that reaches sea level at high noon in a clear sky.

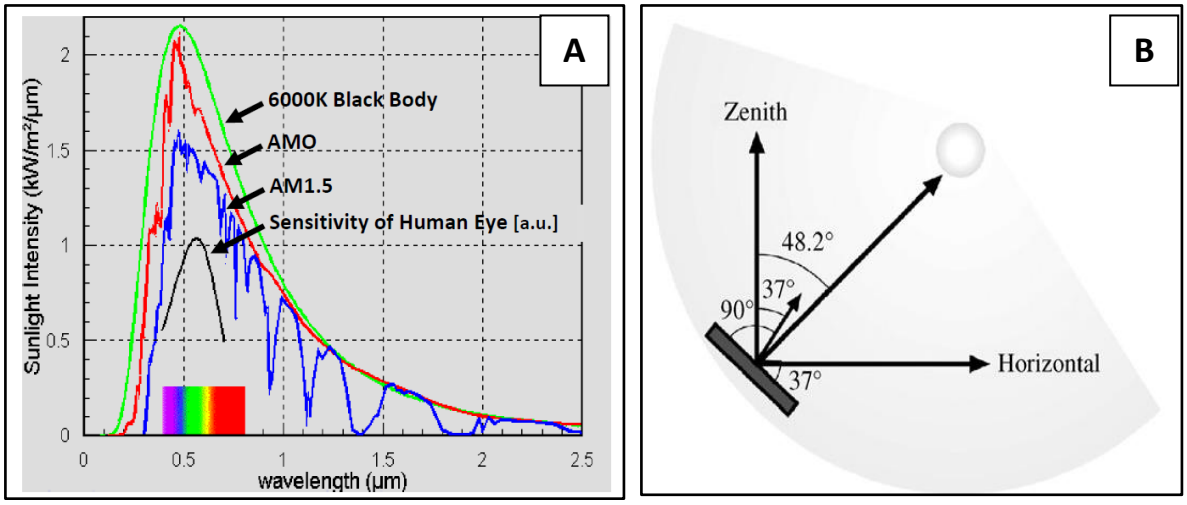

Figure 2-1: (A) Solar radiation intensity (6000 K black body) compared to solar spectrum at AM 0 (radiation on the outer surface of the atmosphere) and AM 1.5 and (B) Configuration for AM 1.5 solar illumination [2-3].

2.2 Photoelectrochemical Water – Splitting

The reaction of water splitting into hydrogen and oxygen at standard ambient temperature and pressure is a non-spontaneous process. It is accompanied by positive

change in Gibb's free energy (ΔG = 238 kJ mol^{-1}). According to Nernst equation, external bias (V) can be applied to enforce the reaction to occur.

$$H_2O \text{ (liquid/vapor)} + \text{electrical energy} \rightarrow H_2\,(g) + \tfrac{1}{2}\,O_2\,(g),\ \Delta G = n\,F\,V_{rev} \qquad [2.2.2]$$

where n is the number of electrons involved in the reaction and F is Faraday's constant. Theoretically, V_{rev} is calculated to be 1.229 V_{NHE}. However, a bias of ≈ 1.6 V is required experimentally to allow the reaction to occur due to the various resistances included in the cell. In photoelectrolysis water splitting, the target is to have a system that utilizes light energy to obtain sufficient electricity for the reaction to take place with minimum external bias.

One type of water photoelectrolysis cells (PEC) is composed of n-type semiconductor electrode (photoanode) and a metal cathode immersed in an aqueous electrolyte subject to a light source. The mechanism for water-splitting is described as follows [4]:

1- Light energy greater than or equal to the band gap of the photoanode is absorbed leading to intrinsic ionization that causes the excitation of electrons to the conduction band and the formation of holes in the valence band.

$$2h\nu \rightarrow 2e^- + 2h^+ \qquad [2.2.3]$$

where h is Planck's constant, ν the frequency, e^- the electron, and h^+ is the hole.

2- Oxidation of water by the photo-generated holes at the photoanode/ electrolyte interface into gaseous oxygen and hydrogen ions.

$$2h + H_2O \text{ (liquid)} \rightarrow \frac{1}{2}\,O_2 \text{ (gas)} + 2H^+ \qquad [2.2.4]$$

3- The hydrogen ions migrate through the electrolyte to the cathode to be reduced by the electrons into hydrogen gas.

$$2H^+ + 2e^- \rightarrow H_2 \text{ (gas)} \quad [2.2.5]$$

Accordingly, the overall reaction of water splitting in a PEC is expressed as:

$$2h\nu + H_2O \text{ (liquid)} \rightarrow \frac{1}{2} O_2 \text{ (gas)} + H_2 \text{ (gas)} \quad [2.2.6]$$

As pure water is a poor conductor, aqueous electrolytes containing ionized salts are usually being used to enhance the migration of charges. The mechanism is illustrated in **Figure 2-2** in terms of the energy diagrams and the flow of charges between the photoanode semiconductor, electrolyte and metal cathode. **Figure 2-2 (a)** shows the band diagram of the n-type semiconductor and the metal. The Fermi level of the electrolyte lies between the two water splitting redox potentials (H^+/H_2 and O_2/H_2O) depending on the concentration of hydrogen and oxygen [5]. At equilibrium in dark as shown **in Figure 2-2 (b)**, electrons flow from the n-type semiconductor to the electrolyte to equilibrate the Fermi level leading to the formation of a region at the interface that is depleted from electrons called *depletion layer*. The equilibrium between the Fermi levels of the semiconductor and the electrolyte leads to band bending. Negative ions from the electrolyte gets attracted to this positive layer forming a thin layer called Helmholtz layer. The following equation represents the width of the depletion layer (W_d):

$$W_d = \lambda_D \left(\frac{2\, e|U - Ufb|}{kT} - 1\right)^{1/2} \quad [2.2.7]$$

where λ_D is the distance at which charge separation can occur known as the *Debye length*, U is the applied voltage, U_{fb} is the flat band potential, k is Boltzmann's constant

and T is the absolute temperature. The Debye length can be determined from the following equation:

$$\lambda_D = (\epsilon_r \ \epsilon_0 \ k\,T / N_D \ e^2)^{1/2} \qquad [2.2.8]$$

where ϵ_r is the relative permittivity, ϵ_0 is the permittivity of free space, and N_D is the concentration of the charge carriers. Upon illumination, **Figure 2-2 (c)**, the absorbed photons cause the generation of charge carriers that reduce the band bending. The generated charge carriers are separated by the electric field established in the depletion layer. Electrons move towards the bulk while the holes migrate towards the electrolyte in the case of n-type photoanodes that generate photovoltage but no current flows. The maximum Fermi energy is the flat band potential, which is lower than the H^+/H_2 potential indicating that the water-splitting reaction cannot occur except by applying an external bias. In **Figure 2-2 (d)**, the applied bias causes the raise in the Fermi energy of the metal electrode above the H^+/H_2 potential allowing the hydrogen evolution reaction to take place.

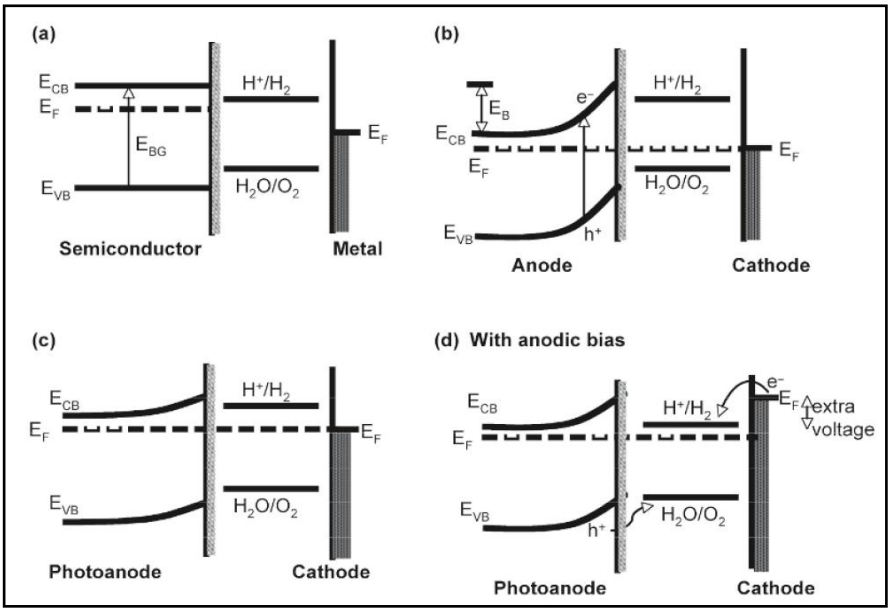

Figure 2-2: The energetic diagram of PEC with n-type semiconductor photoanode and metallic electrode; (a) initial condition before contacts, (b) equilibrium after contact in dark, (c) after illumination and (d) with applied bias on illumination [6].

2.3 Material Requirements

The need to apply external bias upon the use of wide band gap metal oxide semiconductors reduces the efficiency of the solar-hydrogen conversion. As illustrated, the solar water-splitting reaction and the semiconductor-electrolyte interaction undergo several steps that combine physical and chemical concepts. Therefore, there are some material requirements that needed to be achieved. Some of these material aspects that related to the scope of the thesis are illustrated in the following sections.

2.3.1 Band gap

The band gap is the smallest energy difference between the top of the valence and the bottom of the conduction bands. For higher absorption of light energy from the solar spectrum, the optimum band gap is required to be nearly equal to 2 eV. In this case, the

semiconductor can absorb sunlight up to a wavelength of 620 nm according to the following equation:

$$E = \frac{hc}{\lambda} \quad [2.2.9]$$

where E is the photon energy (the semiconductor will absorb only photons that have equal or greater energy than its band gap), h is Planck's constant, c is the speed of light and λ is the light wavelength. Since most of the metal oxide semiconductors have wider band gap, doping and mixed oxides were proposed as techniques to optimize the band gap.

2.3.2 Corrosion and Photo-corrosion Resistance

Semiconductors are required to be stable in aqueous environments during the photoelectrochemical process. Otherwise, their properties will deteriorate as a result of electrochemical corrosion that can be represented by the following equations:

$$AB + Z\,h \rightarrow A^{+Z} + B + \Delta G_a \quad [2.2.10]$$

$$AB + Z\,e^{-} \rightarrow B^{-Z} + A + \Delta G_C \quad [2.2.11]$$

where AB is a semiconductor, Z is the number of electrons or holes, ΔG_a and ΔG_C are the free energy change at the anode and the cathode, respectively. Then, the free enthalpy of oxidation $E_{p,d}$ and the free enthalpy of reduction $E_{n,d}$ can be related as:

$$E_{p,d} = \frac{\Delta Ga}{Z\,N\,A} \quad [2.2.12]$$

$$E_{n,d} = \frac{\Delta Gc}{Z\,N\,A} \quad [2.2.13]$$

To be stable in aqueous electrolytes, the semiconductors should fulfill the following criteria:

$E\ (O_2/\ H_2O) < E_{\ p,\ d}$ [2.2.14]

$E\ (H^+/\ H_2) > E_{\ n,\ d}$ [2.2.15]

where $E\ (H^+/\ H_2)$ is the energy of the redox couple $H^+/\ H_2$, and $E\ (O_2/\ H_2O)$ is the energy of the redox couple $O_2/\ H_2O$. Therefore, the lower band gap is not only important, but along with the band positions corresponding to the redox energy of the water splitting reaction are essential requirements. In **Figure 2-3**, the conduction and valence bands of some metal oxide semiconductors are shown corresponding to the energy of the redox couples $H^+/\ H_2$ and $O_2/\ H_2O$. The pH of the aqueous electrolyte also affects the band positions as it can be observed for TiO_2 in **Figure 2-4**.

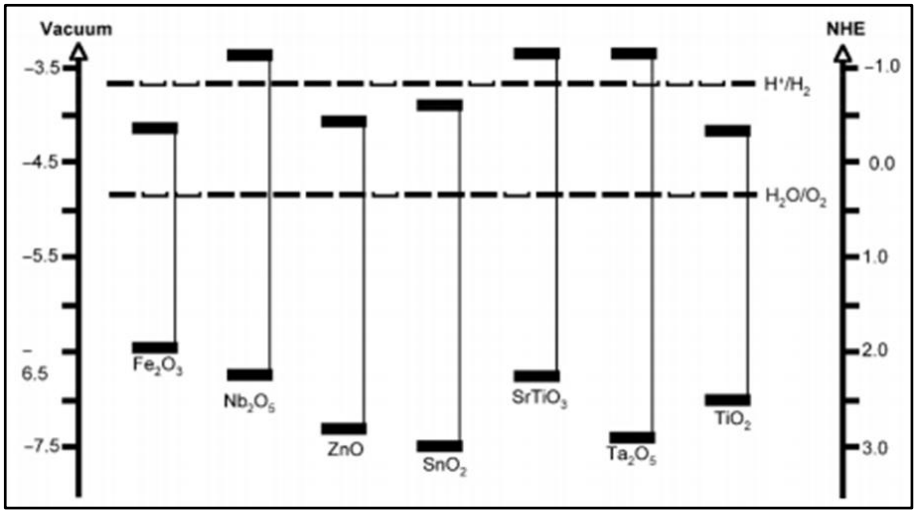

Figure 2-3: The band diagram of some metal oxide semiconducturs with respect to vacuum level and nomal hydrogen electrode level in electrolyte of pH 7 [8].

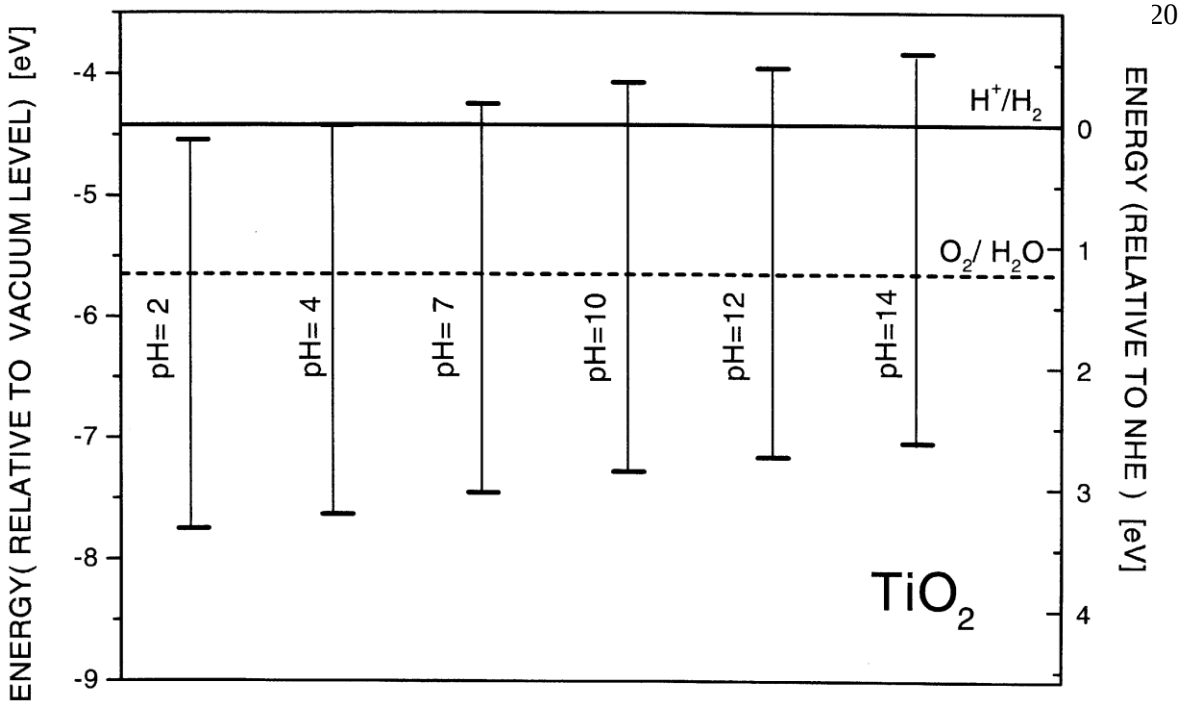

Figure 2-4: The effect of electrolyte pH on the band energies of TiO_2 with respect to vacuum level and normal hydrogen electrode level [8].

2.3.3 Structure

As illustrated, the energy of the band gap and the positions of bands are important for determining the amount of photon energy that can be absorbed to generate charge carriers. However, any electron exists in the conduction band is in a meta-stable state and will eventually stabilize to a lower energy position in the valence band. The excited electrons return back to fill the associated hole in a process called recombination. The separation and fast transport of charges to reach the surface before their recombination and the reactivity of the surface to promote the chemical reactions can be controlled by the bulk and surface properties of the material as shown in **Figure 2-5**. In turn, the bulk and surface properties are greatly affected by the preparation method that defines the structure and the morphology. Differences in the structure and the morphology can

contribute to the discrepancies in the performance of photoelectrodes of the same material.

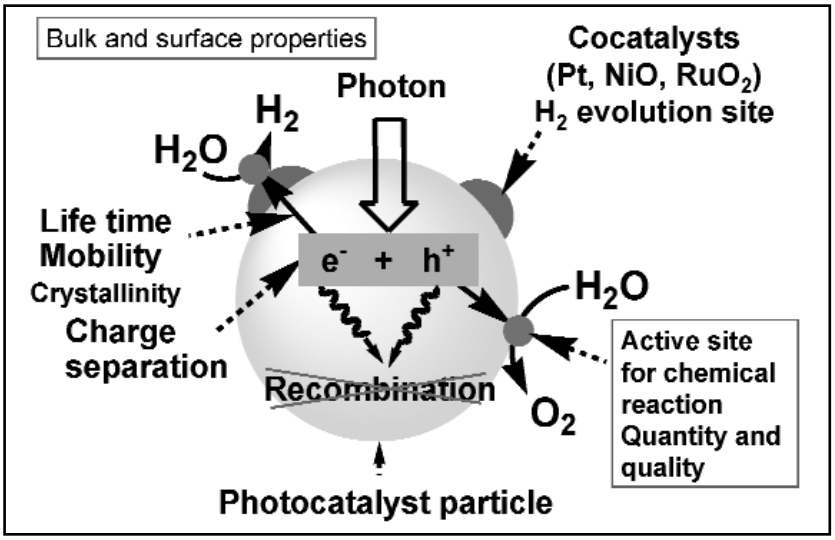

Figure 2-5: Schematic of the bulk and surface properties required to minimize recombination of the photogenerated electrons and holes and provide active sites for the redox reactions [9].

Concerning the structure, high quality material with low density of defects is required for efficient charge transfer and reduction of the electron-hole recombination. In addition, crystallinity is essential to reduce the probability of recombination. The trapping sites arise in the bulk material as a result of various defects such as vacancies, impurities, dislocations and grain boundaries. At the surface, the crystal structure of the material is severely disrupted. Dangling bonds are a result of unsatisfied valence on the surface atoms. Hence, the material's surface may be considered a high recombination site. The recombination of charges through bulk and surface defects and their separation and transport to the aqueous electrolyte are competitive processes as shown in **Figure 2-6**.

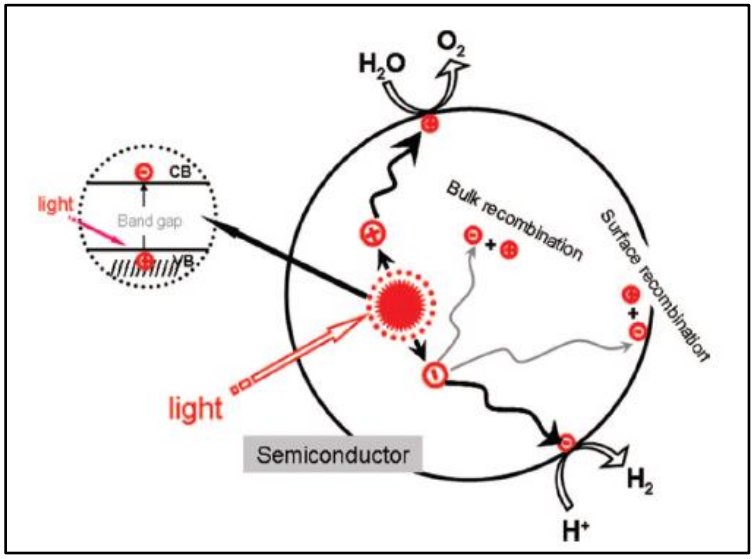

Figure 2-6: Separation and recombination of photogenerated charge carriers in semiconductors [10].

Concerning the morphology, micro and nano–sized materials became attractive because of their high surface-to-volume ratio that provides large surface area for the chemical reactions to take place. However, a trade-off appears in this case as the high surface area can increase the surface recombination as discussed previously.

Ordered one-dimensional micro- and nano- structures offer enhancements over planar structures through decoupling the directions of light absorption and charge carrier collection. In planar structures, the direction of light absorption is the same as the direction of charge carrier collection as shown in **Figure 2-7 A**. For high absorption in planar structures, the material thickness is required to be large. However, this will increase the distance that need to be travelled by the minority carriers (holes in the case of n-type semiconductor) to reach the surface where the chemical reaction takes place. Therefore, the thick planar structure increases the light absorption but the charge recombination is also increased especially if the material has high density of defects. In one-dimensional structures as nanotubes and nanorods, the direction of light absorption is along the length while the minority charge

carriers transport to the surface occurs through the width as shown in **Figure 2-7 B**. In nanomaterials, the thickness is in the range of few nanometers so the distance required to be travelled by the minority carriers to the surface is much less.

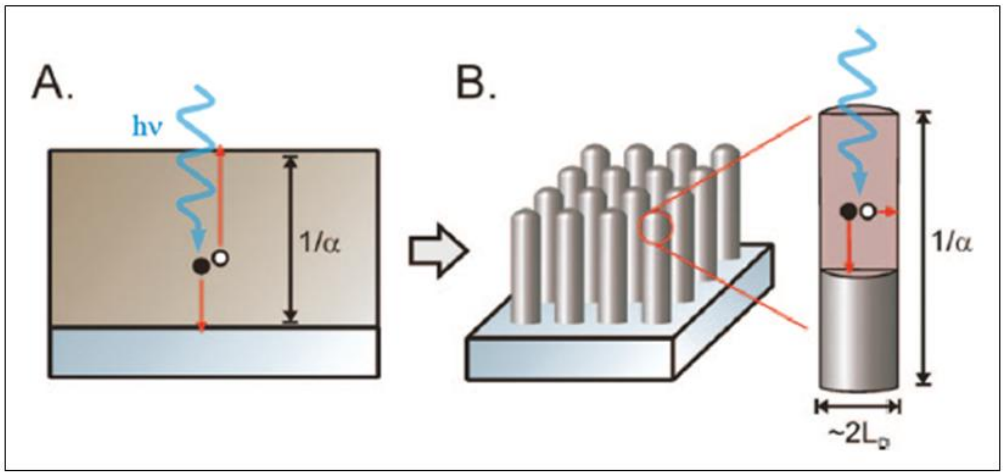

Figure 2-7: The directions of light absorption and charge carrier collection in (A) planar structure and (B) ordered one dimensional structure [10].

The distance that the minority carriers can travel before recombination is known as the diffusion length (L_D).

$$L_D = (D\,\Gamma)^{1/2} \qquad [2.2.16]$$

where D is the diffusion coefficient and Γ is the lifetime of the minority carriers. In order to achieve high performance, the material thickness needs to be equal to the diffusion length, which is a challenging task in the fabrication of some materials.

Other important requirements that motivate researchers to study metal oxide semiconductors are their availability and low cost compared to silicon-based semiconductors. In summary, there are several requirements to develop efficient materials for photoelectrochemical water-splitting, the key factors for functioning are:

(1) Suitable band gap (≈ 2 eV) and band positions to maximize light absorption in the visible region with good stability.

(2) Fast charge transport and fewer defects to minimize bulk and surface recombinations.

A trade-off between these two key factors usually exists in wide band gap metal oxide semiconductors. Therefore, studies are continuing to reach the balance that can result in an optimum efficiency.

2.4 Efficiency

The efficiency of the solar-to-hydrogen conversion is a ratio of the output power generated from the photoelectrochemical cell to be used in the water-splitting chemical reactions to the input light power [11]. The following equation represents the efficiency (η) assuming that all the photogenerated charges are consumed in the chemical reactions:

$$\eta = I\,(1.23 - V_{bias}) / (J_{light} \times A) \qquad [2.2.17]$$

where I is the photocurrent, 1.23 V is the theoretical potential required for water-splitting, V_{bias} is the applied external voltage, J_{light} is the light irradiance (W/m^2), and A is the irradiated area (m^2).

Another way to express the quantum efficiency is known as incident photon-to-current conversion efficiency (IPCE), which measures the amount of photogenerated electrons that are collected at the contact per irradiated photon on the surface of the photoelectrode:

$$IPCE = (1240 \times I_{PH}) / (\lambda \times P_{light}) \qquad [2.2.17]$$

where I_{PH} is the photogenerated current density, λ is the incident light wavelength, P_{light} is the photon flux (W/m^2) and 1240 is unit correction factor. For the laboratory scale, to simulate the AM 1.5 solar radiations, different types of lamps can be used as the xenon lamp. The maximum the critical efficiency that can be reached according to the band gap of the semiconductor material is shown in **Figure 2-8**.

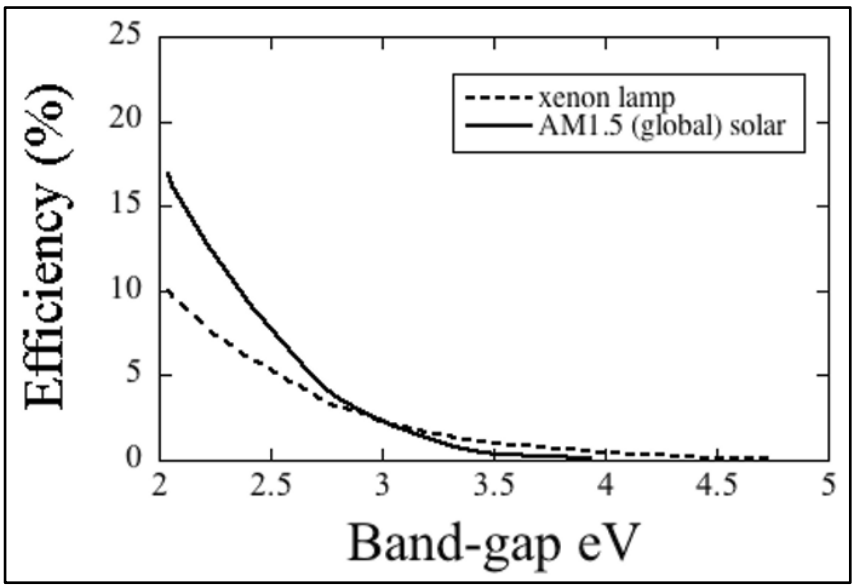

Figure 2-8: Maximum efficiency possible depending upon semiconductor band gap, under xenon arc lamp and AM1.5 solar illuminations [12].

2.5 Niobium Oxides

Niobium was discovered in 1801. It is a transition metal belonging to group 5 and period 5 with an atomic number of 41 and an electronic configuration [Kr] $4d^4\ 5s^1$. The electronic properties of niobium and its compounds are defined by the d-electrons. Chemically, niobium is very resistant to corrosion in acids (ex. HCl, H_2SO_4, HNO_3) and many other organic and inorganic compounds but it can be attacked by HF. It is a soft and ductile refractory metal with BCC crystal structure. It has a wide variety of

applications including uses in super-alloys, superconductors, optical glasses, nuclear reactors, capacitors, piezoelectric devices, batteries, cutting tools, bone implants, and space devices.

Niobium forms, with small atomic anions as nitrogen, carbon and sulfur, very stable alloys. In addition, it has high affinity and binding energy to oxygen [13]. Compounds of niobium, oxygen and other metals also offer rich chemistry [13]. The niobium – oxygen system is of high complexity due to the large number of possible oxides and the wide variety of their structures and properties. **Figure 2-9** shows part of the niobium-oxygen phase diagram [13]. Stoichiometric niobium oxides, NbO, NbO_2 and Nb_2O_5 are among the most studied forms due to their stability. However, there are numerous metastable forms. For instance, three suboxides, NbO*x*, NbO*y*, and NbO*z*, were studied with different oxygen concentrations [14]. Moreover, there exists a series of phases between NbO_2 and Nb_2O_5 having the formula $Nb_{3n+1}O_{8n-2}$ (where n = 5, 6, 7, 8).

The density of conduction electrons decreases from Nb to its oxides. However, NbO still has high room-temperature conductivity [14-15]. Thus, it is used as anode material in electrolytic capacitors [16]. NbO_2 is an n-type semiconductor because of the oxygen vacancies with a small bandgap of 0.7 eV at room temperature [17]. However, it exhibits a semiconductor-metal transition at a temperature of 1081 K as its rutile crystal structure is distorted [27-28]. Nb_2O_5 is an n-type semiconductor with wide band gap that varies from 3.3 to 3.9 eV according to its crystal structure [18-19]. Schultze *et al.* reported a bandgap of 5.2 eV for passive films [20]. Brayner *et al.* reported the increase in bandgap from 3.4 to 4.2 eV as the size of the Nb_2O_5 nanoparticles decrease below 4 nm due to quantum-size effect [21].

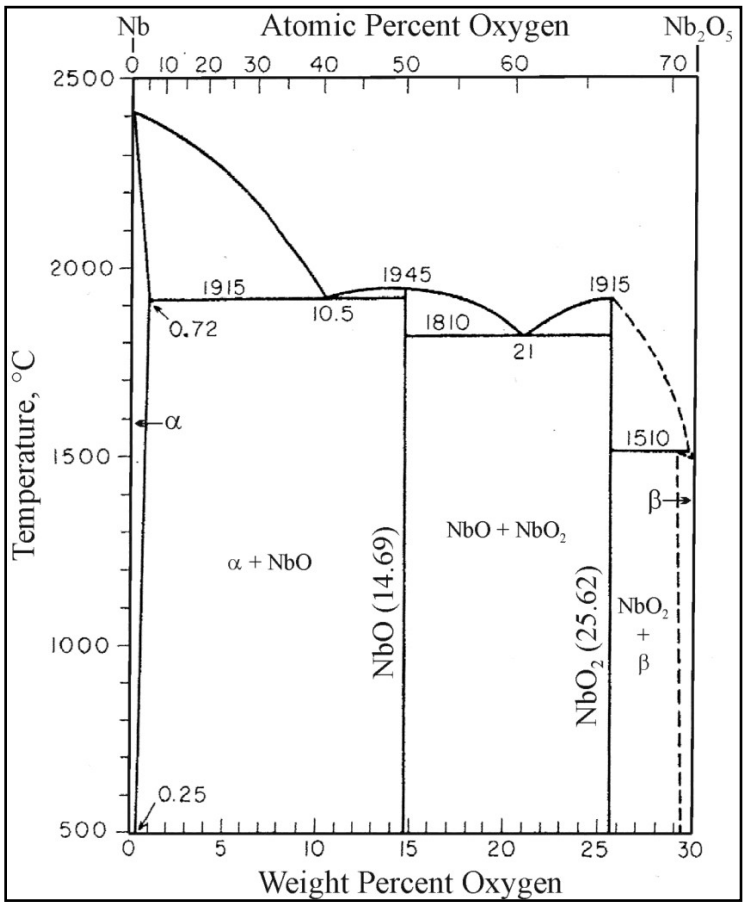

Figure 2-9: Niobium-Oxygen phase diagram [13].

There are no less than 15 polymorphs reported in literature for Nb_2O_5 [22-23]. The low temperature phase (T-Nb_2O_5) forms orthorhombic crystal whose Nb atoms are mainly surrounded by seven or six O atoms forming pentagonal bipyramids or distorted octahedrons, respectively, while the few remaining Nb atoms are coordinated to nine O atoms in interstitial sites [24]. The high temperature phase (H-Nb_2O_5) is formed in a monoclinic structure and it is considered the most stable polymorph with insulating properties [24]. **Table 2-1** shows a summary of some properties of different Nb_2O_5 polymorphs. The occurrence of a certain polymorph depends on the preparation methods

and annealing conditions. **Figures 2-10** shows some transformations from amorphous Nb_2O_5 to different polymorphs as reported in literature [25]. There are also different sub-stoichiometric Nb_2O_{5-y} metastable phases ($0 < y < 1$) that have n-type semiconductivity [26]. Due to the chemical stability and the richness in structures and properties, Nb_2O_5 was studied for various applications from catalysis to solar cells, sensors, optical glasses, microelectronics and biomaterials [27-29]. However, limited studies have discussed the photocatalytic application of Nb_2O_5 in water–splitting reaction and limited studies discussed the effect of the different polymorphs on the properties [30].

Table 2-1: The crystal structure of some polymorphs of Nb_2O_5

Polymorph	**Crystal Structure**
TT Nb_2O_5	Pseudohexagonal
TNb_2O_5	Orthorhombic (Space group D2h 9 – Pbam)
M Nb_2O_5	Tetragonal (Space group D4h 17 – I4/mmm)
N Nb_2O_5	Monoclinic (Space group C2h 3 – C2/m)
P Nb_2O_5	Tetragonal (Space group $D4^{10}$ – $I4_122$)
H Nb_2O_5	Monoclinic (Space group C21 – P2, C2h1 – P2/m)

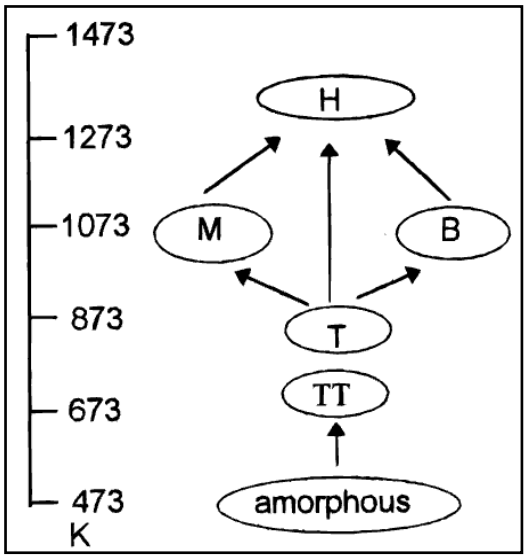

Figure 2-10: Transformation of Nb_2O_5 polymorphs at different temperatures [25].

2.6 Plasma Sputtering Technique

In principle, sputtering is one of the physical mechanisms in which atoms are ejected from the surface of a material when that surface is struck by sufficiency energetic particles as shown in **Figure 2-11**. It was developed by Langmuir in 1952 as a fabrication method for the deposition of thin films after the discovery of the principle in 1852. External voltage is applied between two electrodes, a cathode (the target material) and an anode (substrate material). This system is placed in a chamber filled with inert gas as argon so as not to form any chemical reactions. In some applications in which oxide or nitride films are needed, reactive gas is added with the argon as oxygen or nitrogen to form chemical compound with the deposited film (reactive sputtering) [31]. The applied electric field causes the acceleration of free electrons that in turn colloid in elastically with the atoms of the inert gas. As a result, the gas atoms undergo excitation and ionization creating what is called plasma. Gas excitation causes the formation of discharge glow and the gas atoms are ionized into positive ions and other free electrons that repeat the process of bombarding the gas atoms. The positive ions are accelerated towards the cathode colliding with the atoms of the target material. The atoms that are locked out from the target are transported to the substrate. The process continues to form a film of the target material on the substrate. When the target material is conductive, the resulting charges from the collision of the positive ions can move freely preventing any charge buildup.

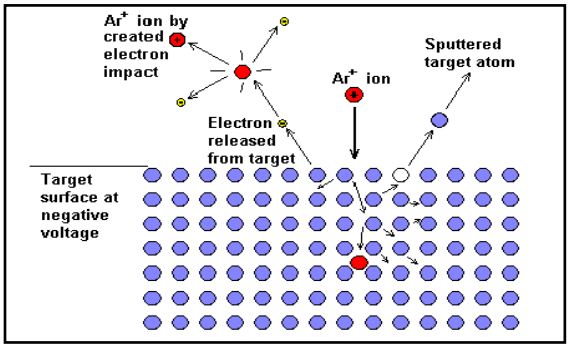

Figure 2-11: Sputtering principle [32].

However, if the material is an insulator, the conduction band will not allow free charge movement. As the ions bombard the surface atoms, their charge will remain localized and over time the charge will build up, making it impossible to further bombard the surface so that the sputtering process stops. In order to prevent this, alternating current issued at a high frequency so that the ions (heavier than the electrons) cannot follow the switching fast enough and only electrons hit the surface to neutralize charge. Hence, sputtering can be powered by direct current (DC sputtering) or radio frequency source (RF sputtering) according to the type of the target material [31]. **Figure 2-12** shows the components of each system.

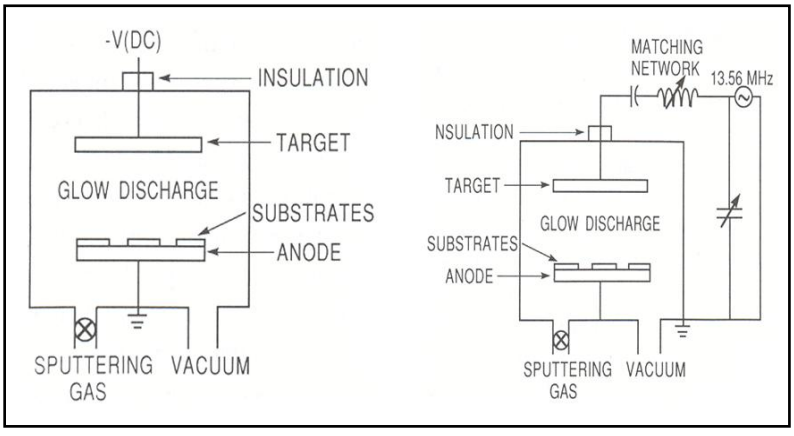

Figure 2-12: Components of (left) DC and (right) RF sputtering systems [33].

Several parameters control the sputtering process and the resulting film as the chamber pressure, the applied power, the distance between the target and the substrate, the material of the target and the substrate and the temperature of the substrate.

References

1. Zini, G.; Tartarini, P. *"Solar Hydrogen Energy Systems Science and Technology for the Hydrogen Economy"*, Springer: Verlag Italia **2012**.
2. Sekuler, R.; Blake, R. *"Perception"*, Alfred A. Knopf Inc, New York, **1985**.
3. Kudo, A. Photocatalysis and solar hydrogen production. *Pure and Applied Chemistry* **2007**, 79, 1917–1927.
4. Nozik, A. J.; Memming, R. Physical chemistry of semiconductor-liquid interfaces. *J. Phys. Chem.* **1996**, 100, 13061-13078.
5. Li, Y.; Zhong, J. Z. Hydrogen generation from photoelectrochemical water splitting based on nanomaterials. *Laser Photonics Rev.* **2010**, 4, 517–528.
6. Bak, T.; Nowotny, J.; Rekas, M.; Sorrell, C. C. *Int. J. Hydrogen Energy* **2002**, 27, 991.
7. Walter, M. G.; Warren, E. L.; McKone, J. R.; Boettcher, S. W.; Mi, Q.; Santori, E. A.; Lewis, N. S. Solar Water Splitting Cells. *Chem. Rev.* **2010,** *110*, 6446–6473.
8. Nowotny, J.; Sorrell, C.C.; Bak, T.; Sheppard, L.R. Solar-hydrogen: Unresolved problems in solid-state science. *Solar Energy* **2005**, 78, 593–602.
9. Maeda, K. Photocatalytic water splitting using semiconductor particles: History and recent developments. *Journal of Photochemistry and Photobiology C: Photochemistry Reviews* **2011**, 12, 237– 268.

10. Thursfield, A.; Metcalfe, I. S.; Kruth, A.; Irvine, J.T.S. *"Defect chemistry and transport in metal oxides. Metal oxides: chemistry and applications".* CRC Press, Taylor and Francis Group: FL, USA, **2006**.
11. Linsebigler, A. L.; Lu, G.; Yates, J. T. Photocatalysis on TiO_2 Surfaces: Principles, Mechanisms, and Selected Results. *Chem. Rev.***1995**, *95*, 735.
12. Chen, X.; Shen, S.; Guo, L.; Mao, S. S. Semiconductor-based Photocatalytic Hydrogen Generation. *Chem. Rev.* **2010,** 110, 6503–6570.
13. Grundner, M. XPS and AES studies on oxide growth and oxide coatings on niobium. *Journal of Applied Physics* **1980**, 51, 397 – 405.
14. Elliott, R. P. Columbium-Oxygen System. Trans. Am. *Soc. Metals* **1960**, 52.
15. Turzhevsky, S. A.; Novikov, D. L.; Gubanov, V. A.; Freeman, A. J. Electronic structure and crystal chemistry of niobium oxide phases. *Phys. Rev. B* **1994**, 50, 3200–3208.
16. Niebuhr, J. Die niederen Oxide des Niobs. *Journal of the Less Common Metals* **1966**, 11, 191–203.
17. Rao, C. N. R.; Wahnsiedler, W. E.; Honig, J. M. Plasma resonance in TiO, VO and NbO. *Journal of Solid State Chemistry* **1970**, 2, 315–317.
18. Hulm, J. K. C.; Jones, K.; Hein, R. A.; Gibson, J. W. Superconductivity in the TiO and NbO systems. *Journal of Low Temperature Physics* **1972**, 7, 291-307.
19. Krishna M. G.; Bhattacharya, A. K. Thickness and Oxygen Pressure Dependent Optical Properties of Niobium Oxide Thin Films. *Int. J. Mod. Phys. B* **1999**, 13, 411-418.

20. Schultze, J. W.; Lohrengel, M. M. Stability, reactivity and breakdown of passive films. Problems of recent and future research. *Electrochimica Acta* **2000,** 45, 2499–2513.

21. Brayner, R.; Bozon-Verduraz, F. Niobium pentoxide prepared by soft chemical routes: morphology, structure, defects and quantum size effect. *Phys. Chem. Chem. Phys.* **2003**, 5, 1457-1466.

22. Marucco, J. F. Thermodynamic study of the system NbO_2-Nb_2O_5 at high temperature. *Journal of Solid State Chemistry*, **1974**, 10, 211–218.

23. Naito, K.; Kamegashira, N.; Sasaki, N. Phase equilibria in the system between NbO_2 and Nb_2O_5 at high temperatures. *Journal of Solid State Chemistry* **1980**, 35, 305-311.

24. Kato, K.; Tamura, S. Die Kristallstruktur von T-Nb_2O_5. *Acta Cryst.* 1975, B**31**, 673-677**.**

25. Schäfer, H.; Bergner, D.; Gruehn, R. Chemistry of the elements of Niobium and Tantalum LXXI. The thermodynamic stability of the seven phases existing between 2.00 and 2.50 O/Nb. *Z. Anorg. Allg. Chem.* **1969**, 365, 31-50.

26. Nowak, I.; Ziolek, M. Niobium Compounds: Preparation, Characterization, and Application in Heterogeneous Catalysis. *Chem. Rev.* **1999,** *99,* 3603-3624.

27. Zhao, Y.; Zhou, X.; Ye L.; Chi, S.; Tsang, E. Nanostructured Nb_2O_5 catalysts. *Nano Reviews* **2012**, 3, 17631 – 17642.

28. Tanabe, K. Catalytic application of niobium compounds. *Catalysis Today* **2003**, 78, 65–77.

29. Ko, E. I.; Weissman, J. G. Structures of niobium pentoxide and their implications on chemical behavior. *Catal. Today* **1990**, *8*, 27-36.

30. Tzbergar, F.; Eismanm, N.; Rrya, A.; Erkenblit, M. Chemistry of the Group VB Pentoxides.VI. The Polymorphism of Nb_2O_5. *J. Am. Chem. Soc.* **1957**, 79, 2039–2043.

31. Seshan, K. *"Handbook of Thin-Film Deposition Processes and Techniques".* Noyes Publications / William Andrew Publishing: USA **2002**.

32. Kirschbrown, J. RF/ DC Magnetron Sputtering. 2007. http://www.unc.edu/~justink/RFDC_Sputtering.pdf. Retrieved on 13th of December, 2013.

33. http://faculty.kfupm.edu.sa/phys/kuhaili/TSF/sputtering.pdf. Retrieved on 13th of December, 2013.

Chapter 3

Review of Relevant Literature

3.1 TiO_2 – ZnO Photoanodes

Of particular interest, TiO_2 is being widely investigated due to its advantageous properties such as low cost, abundance, stability and vectorial charge transfer [1]. On the other hand, due to its direct wide band gap, large excitation binding energy, excellent optical properties and low cost, zinc oxide (ZnO) has been considered as another candidate material in solar energy harvesting systems, exhibiting comparable efficiency to TiO_2-based systems [2]. However, despite those good attributes of both oxide systems, a long-standing challenge still remains in reducing the high recombination rates of photogenerated charge carriers in both TiO_2 and ZnO. To this end, many trials have been made to overcome such limitation, including surface doping [3], passivation and decoration [4, 5], however with marginal success.

Motivated by the high electron mobility in ZnO (~0.1–0.001 $cm^2\ V^{-1}\ s^{-1}$ in nano-particle film and >100 $cm^2\ V^{-1}\ s^{-1}$ in bulk) and the negative shift in its valence (VB) and conduction band (CB) potentials [6] compared to those of TiO_2, many researchers aimed at studying the combination of ZnO and TiO_2 to achieve hybrid properties [7-10].

In the application of dyes' photo-degradation, Kostedt *et al.* showed that the methods of heating TiO_2-ZnO mixed oxides affects the band gap values as shown in **Figure 3-1** [7].

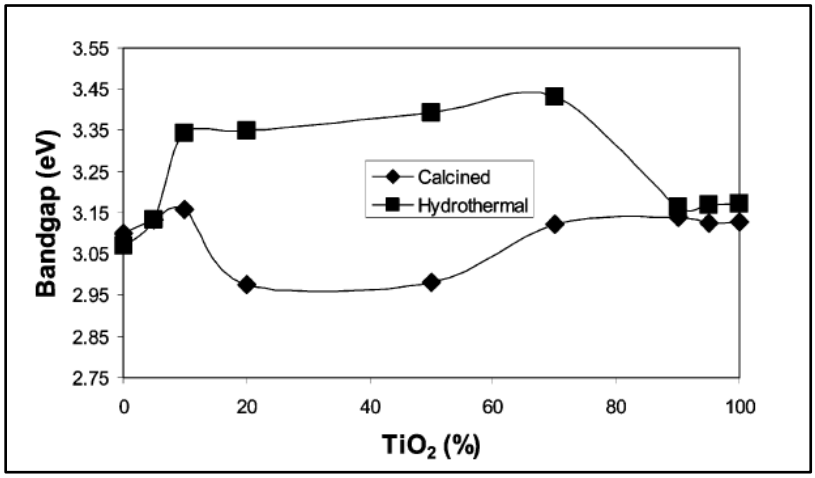

Figure 3-1: The band gap values for TiO_2-ZnO mixed oxide nanoparticles heated by two different methods; calcinations and hydrothermal [7].

In transparent Zn-doped TiO_2 films prepared by pulsed DC magnetron co-sputtering method using Ti and Zn mixed target, W. Zhang *et al.* showed that the photocatalytic degradation of methyl orange did not show noticeable difference in low concentrations of ZnO. However, the photocatalytic activity showed an abrupt decrease as the concentration of ZnO increases as shown in **Figure 3-2**, which was related to the decrease in the crystallinity as the ZnO concentration increases [8].

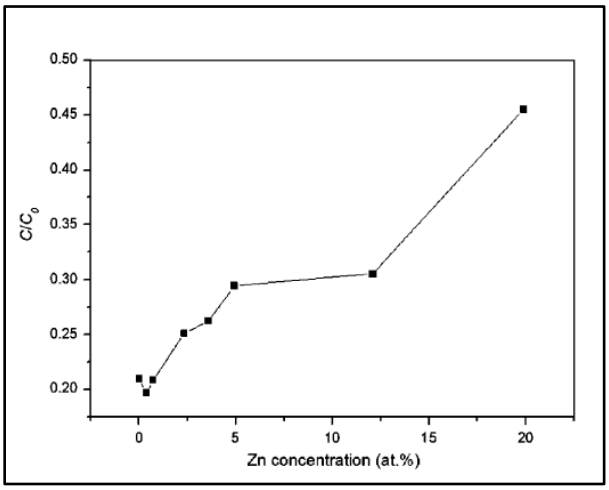

Figure 3-2: The change in the concentration of methyl orange corresponding to the amount of zinc doped in TiO2 films after irradiation for 180 min [8].

On the other hand, Liao *et al.* reported higher photocatalytic activity for TiO_2-ZnO composite nanoparticles in the degradation of methyl orange compared to that for TiO_2 nanoparticles formed without Zn addition [9]. The optimum molar ratio of TiO_2 to ZnO was found to be 1:0.25 while more addition of Zn resulted in decrease for the photocatalytic activity [9]. Zhang *et al.* showed the enhancement in the photo-oxidation reaction of phenol by coating ZnO tetrapod structure with TiO_2 nanoparticles compared to bare ZnO tetrapods, although it was lower than that of commercial TiO_2 nanoparticles (P-25) as shown in **Figure 3-3** [10]. The authors explained that the valence band of TiO_2 is more positive than that of ZnO so it is more powerful in the oxidation of phenol, which can't be favored in other reactions as the photo-degradation of methylene blue [10]. In addition, it was explained that the tetrapod tips were large in dimensions to allow the migration of the holes to the surface [10]. Therefore, important conclusions can be drawn from this study that the photoactivity is related to the type of reaction and that the structure plays an important role.

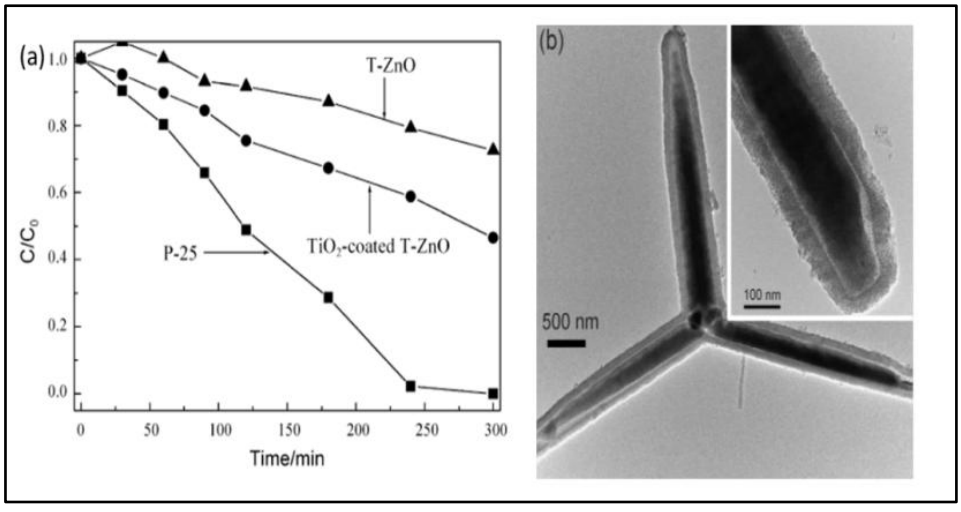

Figure 3-3: TiO_2 nanoparticles coating on ZnO tetrapods; (a) is the concentration change in phenol over different photocatalysts and (b) shows TEM image of a single ZnO tetrapod [10].

He *et al.* studied the photocatalytic activity of ZnO nanorods coated with TiO_2 nanoparticles formed by chemical synthesis in the degradation of methylene blue [11]. The enhancement in the photocatalytic activity was ascribed to the enhanced charge separation as the electrons transfer from the conduction band of ZnO to that of TiO_2 while the holes transfer from the valence band of TiO_2 to that of ZnO as shown in **Figure 3-4** so that the recombination of electron-hole pairs is reduced. As the previous studies, the authors pointed to the effect of the homogeneity and the thickness of coating on the photocatalytic performance.

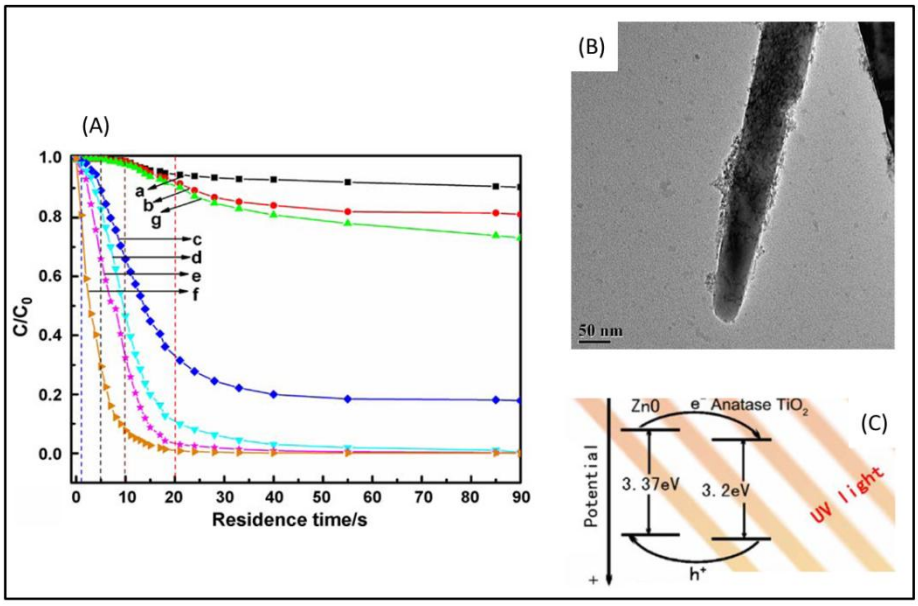

Figure 3-4: ZnO nanorods deposited with TiO_2 nanoparticles for photodegradation of methylene blue; (A) is the concentration change by (c) pristine ZnO nanorods, (d-f) one, two, three and six layers of TiO_2 on ZnO nanorods, (B) is TEM image of TiO_2-ZnO nanorod and (C) is the proposed mechanism of charge separation in the system [11].

With the same explanation of the enhanced charge separation in coupling TiO_2 and ZnO heterostructure, Prabakar *et al.* reported improved performance for dye-

sensitized solar cells of ZnO nanorods and nanoflowers coated with TiO_2 shell formed by solution method as shown in **Figure 3-5** [12].

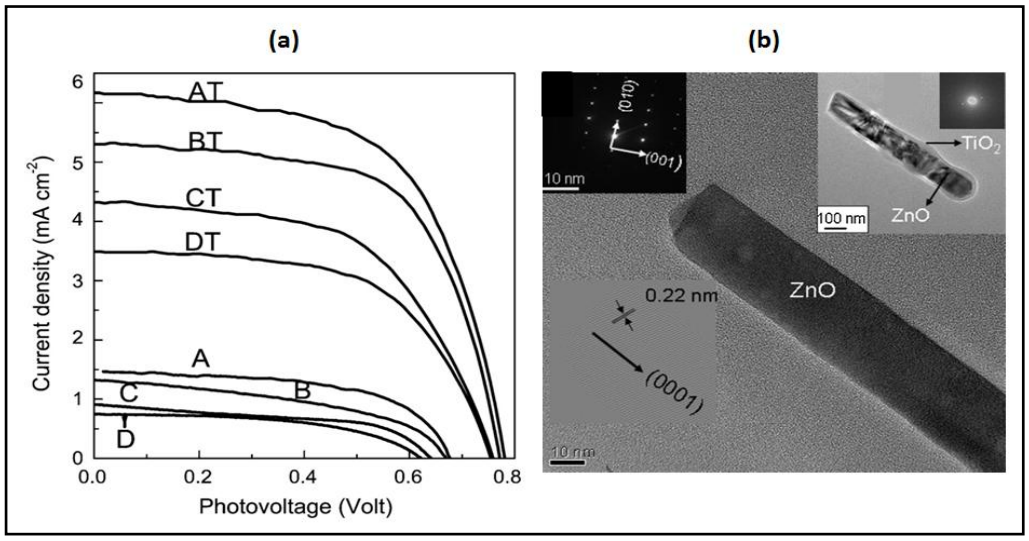

Figure 3-5: DSSC of ZnO nanorods and nanoflowers coated with TiO_2 shell; (a) I–V Characteristics of ZnO nanorod (A, B) and nanoflowers (C, D) and TiO_2thin film encapsulated ZnO nanorod (AT, BT) and nanoflower (CT, DT) DSSCs and (b) is TEM image of single ZnO nanorod with TiO_2 shell [12].

For solar-water splitting application, ZnO nanowires with ultrathin shell of TiO_2, deposited by atomic layer deposition method as shown in **Figure 3-6**, produced a photocurrent of 0.5 mA/cm^2 under simulated AM 1.5 sunlight, which is 25 % higher than that of bare ZnO nanowires [13]. Liu *et al.* illustrated that the TiO_2 shell allowed the photoreaction to occur in strongly alkaline solution without stability problems by removing hole traps [13]. The thermal annealing of the material showed further increase in the photocurrent to 0.7 mA/ cm^2 [13].

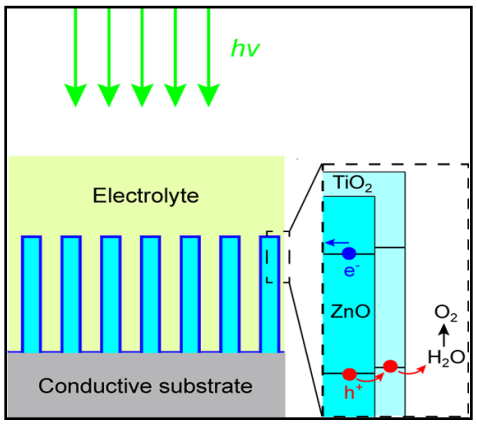

Figure 3-6: Schematic of ZnO nanowires with ultrathin TiO_2 shells used for water splitting reaction [13].

Pan et al. fabricated TiO_2 nanobelt/ZnO nanorod composite photoelectrodes with flower-like and/or grass-like microstructures via solution methods as shown in **Figure 3-7 (A)** [14]. For the flower-like composite, the ZnO nanorods disperse on TiO_2 nanobelt films, while for the grass-like one, ZnO nanorods grow disorderly like grass on the TiO_2 nanobelt film surface. It was found that the grass-like TiO_2 nanobelt/ZnO nanorod sample has the biggest light absorption, but the flower-like TiO_2 nanobelt/ZnO nanorod photoelectrode has the highest photocurrent density as shown in **Figure 3-7 (B)** [14]. Therefore, it was concluded that the water-splitting properties was related to photogenerated electron−hole separation efficiency, not the absorption difference. The authors further explained that TiO_2 nanobelts and ZnO nanorods have a better electrical contact in the flower-like heterostructure as shown in **Figure 3-8 (a)**. This allows quick transfer of photoelectrons from the TiO_2 nanobelt into the ZnO nanorod and reduces the probability of recombination between the photogenerated electrons and holes. On the other hand, only a few ZnO nanorods grow on the surface of TiO_2 nanobelts in the grass-

like nanostructure as shown in **Figure 3-8 (b)**, resulting in weaker electrical contact and higher possibility of recombination [14].

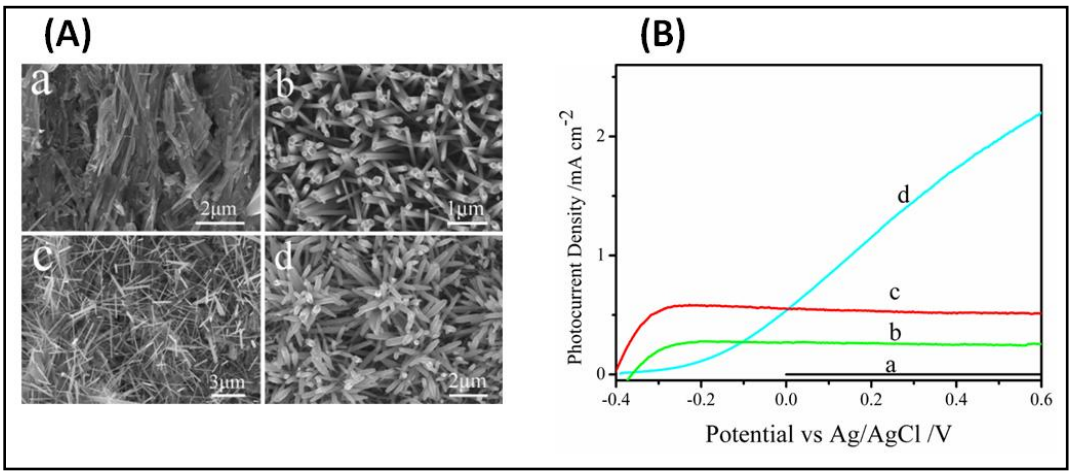

Figure 3-7: TiO_2 nanobelt/ZnO nanorod composite photoelectrodes. (A) FESEM images of TiO_2 nanobelt photoelectrode (a), ZnO nanorod photoelectrode (b), grass-like TiO_2 nanobelt/ZnO nanorod composite photoelectrode (c) and flower-like hierarchical TiO_2 nanobelt/ZnO nanorod heterogeneous photoelectrodes (d). (B) Dark scan curve of ZnO nanorod, grass-like, and flower-like TiO_2 nanobelt/ZnO nanorod photoelectrodes (a); photocurrent density/potential curves of ZnO nanorod photoelectrode (b), grass-like TiO_2 nanobelt/ZnO nanorod photoelectrode (c), and flower-like TiO_2 nanobelt/ZnO nanorod photoelectrode (d) in 0.5 M Na_2SO_4 electrolyte under xenon lamp irradiance of 120 mW cm^{-2} [14].

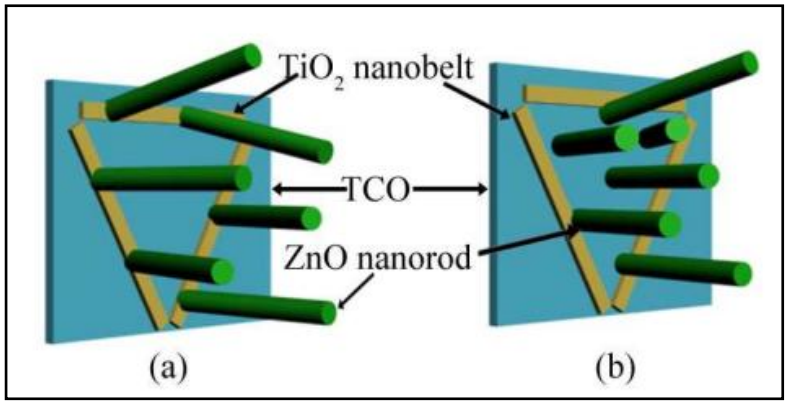

Figure 3-8: Schematic diagrams for the structure of the flower-like TiO_2 nanobelt/ ZnO nanorod photoelectrode (a) and grass-like TiO_2 nanobelt/ZnO nanorod photoelectrode (b), respectively [14].

Being ordered and strongly interconnected, the nanotubular architecture eliminates randomness of the grain network and enhances electrical connection. The nanotube architecture has a large surface area that enables intimate contact with the electrolyte. Additionally, the morphological parameters of the architecture can be precisely controlled. Xiao fabricated one dimensional TiO_2-ZnO heterostructure by first forming TiO_2 nanotubes by anodization and then using pyrolysis for the addition of ZnO nanoparticles in the interior and exterior surfaces of the TiO_2 nanotubes at different percentages [15]. The photocurrent response of the heterostructure showed an increase by approximately double that of the blank TiO_2 nanotubes with a good stability in the aqueous solution [15]. **Figure 3-9** summarizes the fabrication, morphology and photocatalytic measurements of the TiO_2-ZnO heterostructure reported by Fang-Xing Xiao [15]. It can be observed from the FESEM images that the TiO_2 nanotubes were not completely covered with the ZnO nanocrystals.

In addition, Lin *et al.* reported the photocatalytic activity of n-p-n heterojunction made of a shell of TiO_2 that covered ZnO nanorods with interface layer made of p-type Zn^{+2} doped Ti_2O_3 by hydrothermal procedure [16]. The use of the n-p-n heterostructure in the photocatalytic degradation of methyl orange showed increase by nearly 3 times compared to bare ZnO nanorods and TiO_2 nanoparticles [16]. This study pointed to the role of the interface layer in core – shell structures [16].

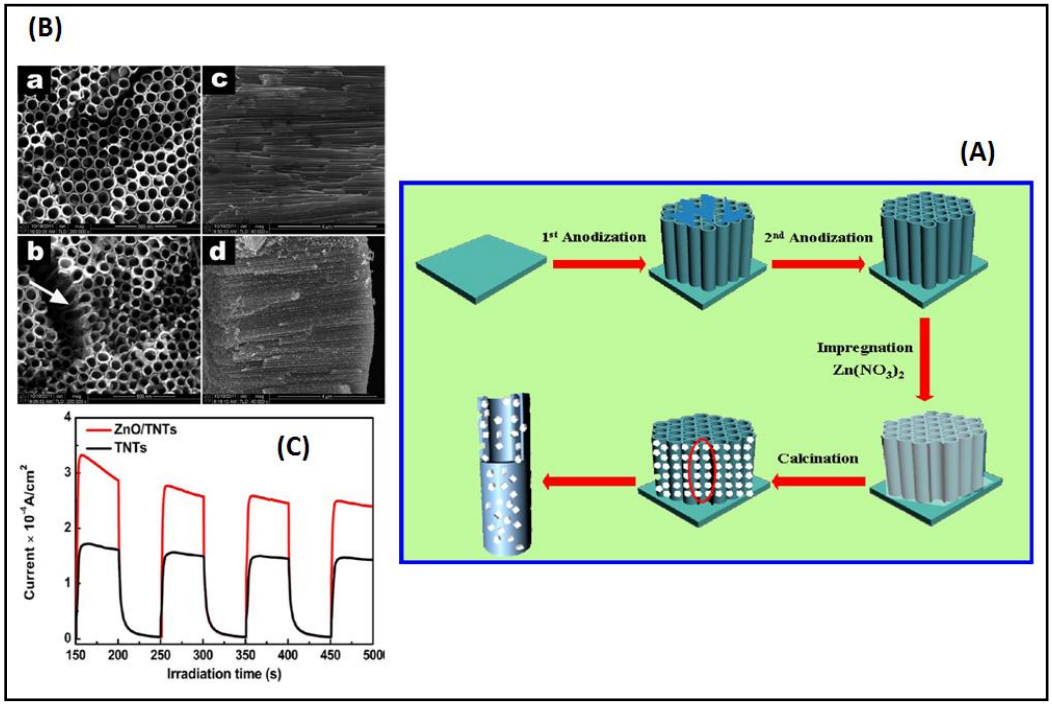

Figure 3-9: TiO_2 nanotubes- ZnO heterostructure synthesized by (A) two –step anodization to form TiO_2 nanotubes followed by pyrolysis for the ZnO decoration, imaged by FESEM as shown in (B): a and c are top and cross sectional views for TiO2 nanotubes while b and d are top and cross sectional views of TiO_2-ZnO heterostructure, respectively. The photocatalytic activity measured in 0.1 M Na_2SO_4 solution under UV light without external bias for TiO_2 nanotubes- 15 % ZnO heterostructure is shown in (C). [15].

To understand the charge dynamics, Naseri *et al.* studied the photoelectrochemical activity of ZnO/ TiO_2 and TiO_2/ ZnO nanolayers fabricated by sol-gel method under visible irradiation [17]. Combining TiO_2 and ZnO nanolayers showed enhancement over the single layers. However, the TiO_2/ ZnO nanolayer showed higher photocatalytic activity and longer electron life time compared to the ZnO/ TiO_2 nanolayer as shown in **Figure 3-10** [17]. The authors explained that the higher surface ratio and roughness of the TiO_2/ ZnO nano-layer as measured by AFM promotes the easier transfer of holes and hence the life time and the photoactivity increases [17].

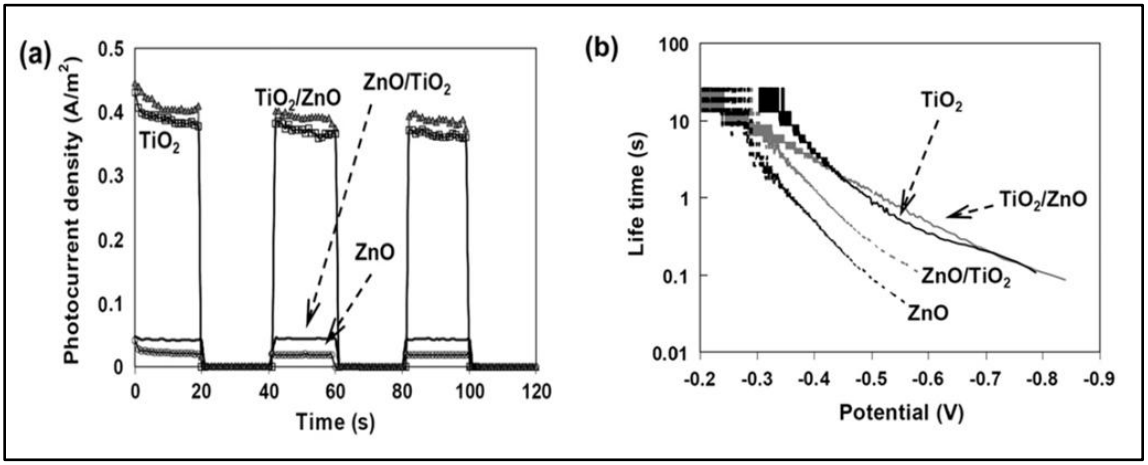

Figure 3-10: Photoelectrochemical properties of ZnO/ TiO_2 and TiO_2/ ZnO nanolayers; (a) is the photocurrent density versus time for the synthesized nanolayer thin films at fixed 0.5 V potential and (b) is the calculated life time of the electrons [17].

In summary, the previous studies attributed the enhanced photocatalytic activity of TiO_2/ZnO heterojunctions to the modification of their electronic states. The transfer of photogenerated electrons from the CB of ZnO to the CB of TiO_2, along with the transfer of photogenerated holes from the VB of TiO_2 to that of ZnO, was used to explain the observed enhancement of electron–hole pair's separation and lifetime as shown in **Figure 3-11** [18-19]. Moreover, Schrauben *et al.* showed that the efficient charge carriers dynamics is accompanied by H^+ transfer [20], which is an advantage in the water oxidation process ($2H_2O = O_2 + 4H^+ + 4e^-$), avoiding the high energy chemical intermediates.

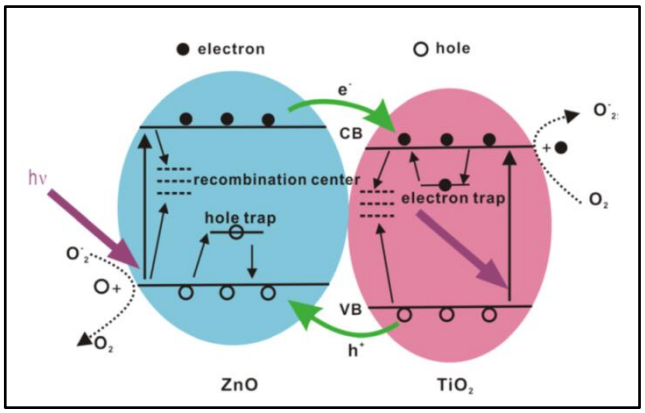

Figure 3-11: Schematic of the band gap energy and the mechanism of charge separation in TiO2-ZnO heterostructure [19].

However, the use of TiO_2/ZnO powders and thin films, the most investigated forms, suffer from recycling and/or stability problems, especially under the application of electric field. It can also be noticed from the above literature survey that there are still contradiction between the results showing enhancements and others showing decrease in the photoactivity compared to the bare materials. This is believed to be due to the different fabrication methods that in turn affects the morphology, homogeneity and crystallinity of the heterostructure. Also, most investigated junctions so far are made of ZnO core and TiO_2 shell, based on the fact that TiO_2 is more stable than ZnO in aqueous electrolytes, with the opposite junctions (ZnO/TiO_2, core-shell) being rarely reported.

3.2 Niobium Oxide-based Photoanodes

3.2.1 Fabrication of Niobium Oxides by Anodization

Anodization of valve metals including aluminum, titanium, zirconium, hafnium, and tantalum is well investigated [21 – 26]. Successful procedures were found to result in well-developed, self-organized structures as nanotubes, nanorods and nanowires. Although, niobium is one of the valve metals, the reported procedures to fabricate self-ordered structures of niobium oxides so far are limited. Porous and comparably thin morphologies were the most obtained ordered structures of niobium oxides. Wei *et al.* explained that the difference between metals that can form nanotubes from its oxides (ex. Ti, Zr, Hf) and metals (ex. Nb) that form pores in terms of the ability to form electrolyte – soluble layers between the porous oxide cells [27]. Thus, changes in the anodization parameters can result in different morphologies [27]. In this section, some of the anodization reports on niobium are reviewed.

Niobium oxide thin film was fabricated by anodization followed by the study of their properties and theory of formation [28]. Ono *et al.* studied the effect of pH and temperature in the anodized films of Nb_2O_5 [29]. This study showed that the film thickness, structure and dielectric properties vary with the change of the pH and the electrolyte temperature changes [29].

Nanoporous films of niobium oxide were also fabricated by anodization at different voltages, temperatures and H_3PO_4 – HF electrolyte concentrations [30-31]. Adding a surfactant to the H_3PO_4 – HF electrolyte was reported to produce more regular and longer niobium oxide nanopores [32]. Among the various applications of the nanoporous structure of niobium oxide, detecting DNA hybridization and hydrogen gas sensing are the most widely used applications [33-34].

As mentioned before, the one-dimensional organized structure is of more interest in solar energy and electronic applications. Lee *et al.* showed the fabrication of highly aligned Nb_2O_5 nanochannels through anodization in hot glycerol electrolyte [35]. The proposed application for the nanochannels in that study was as supercapacitor electrodes [35]. The effect of the temperature was also discussed by Ou *et al.* to increase the oxide thickness through increasing the ion diffusion rate during anodization [36]. They fabricated Nb_2O_5 nano-veins with rough surfaces that promoted their use in dye sensitized solar cells providing more dye-loading sites than TiO_2 nanotubes with similar thickness [36]. Other studies reported the anodization of niobium films sputtered on fluorine doped tin oxide (FTO) glass to form transparent nanochannels structures of Nb_2O_5 [37-38]. The

transparent structure is more beneficial for optical systems as solar cells and electrochromic devices.

Other reports used modified configurations of the anodization process. Duplex niobium oxide film composed of thick porous and barrier oxide layers was reported by Kim *et al.* [39]. The duplex layer was formed by anodization at current mode (galvanostatic anodization). Rodrigues *et al.* reported the formation of Nb_2O_5 nanorods and nanotubes by cathodic electrosynthesis of Nb metal in H_3PO_4 and HF electrolyte [40]. However, those formed nanostructures were not well aligned on the Nb substrate.

Among the various nanostructures, studies for the niobium anodization resulted in the fabrication of niobium oxide microstructures. Karlinsey reported the first study on the fabrication of Nb_2O_5 microcones with nanometer-sized tips in HF aqueous electrolytes [41]. They used those structures as bioactive materials [42-43]. It was pointed in these studies that the addition of a small amount of sodium fluorite to the HF electrolyte produced crystal of Nb_2O_5 orthorhombic phase [42-44]. Zhao *et al.* showed that the formation and the distribution of microcones were affected by the HF electrolyte concentration and anodization time [45]. Because of the rough surface, Oikawa *et al.* the surface wettability for water and oil of Nb_2O_5 microcones anodized in glycerol electrolytes [47]. In another study for the surface wettability of porous Nb_2O_5 microcones anodized in hot glycerol electrolyte, Yang *et al.* showed that the water concentration in the electrolyte affects the angle of the tip, which in turn affects the super hydrophobic properties of the microcones [48]. There were different explanations proposed for the growth mechanism of Nb_2O_5 microcones formed in hot glycerol electrolytes [47-48] as

shown in **Figure 3-12**. The effects of the glycerol electrolyte temperature and the anodization time on the fabrication and the crystallization of branched nanofibrous microcones were studied by Yang *et al.* [43]. The authors explained that the crystalline oxide microcones were nucleated at anodizing time of 500-750 seconds after the chemical dissolution of initial amorphous oxide layer was formed at the starting of the process of anodization [43]. Recently, Nb_2O_5 microcones composed of nanowires were studied for dye sensitized solar cells due to their rough surfaces [48]. The authors showed that the efficiency of the cells changed with the anodization parameters that control the morphology [48]. **Figure 3-13** shows some of the morphologies obtained from niobium anodization.

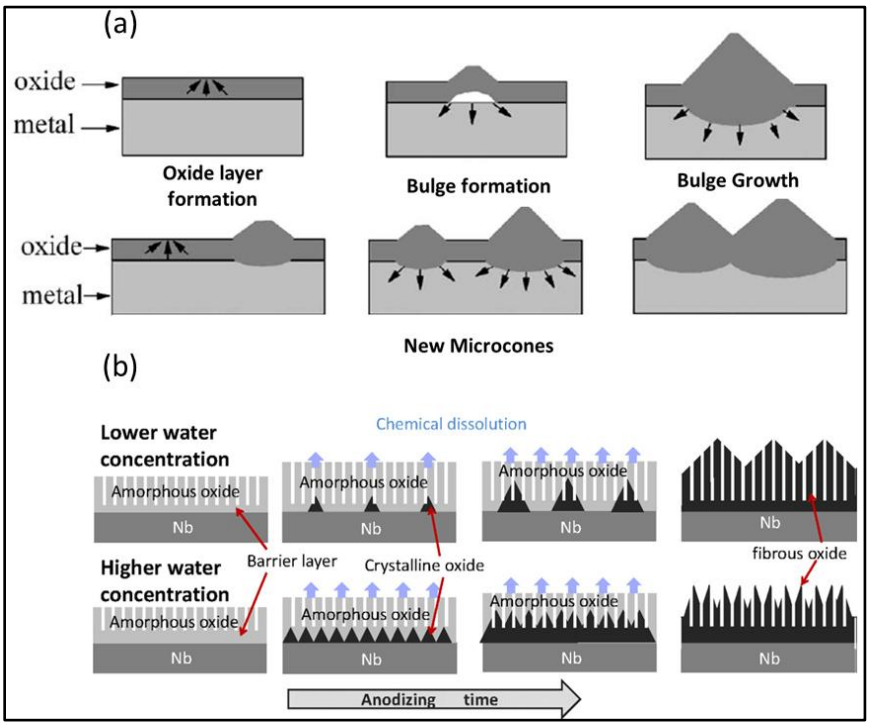

Figure 3-12: The growth mechanism of Nb_2O_5 microcones in glycerol electrolytes proposed by (a) J. Zhao *et al.* and (b) S. Yang *et al.* [47-48].

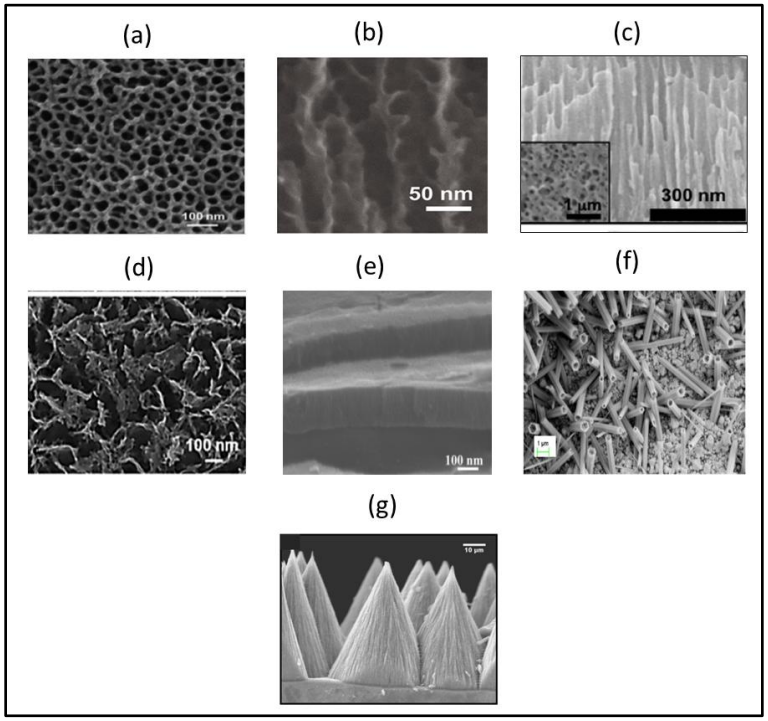

Figure 3-13: Different Nb_2O_5 structures obtained by anodization (a) nanoporous [35], nanoveins [37], nanochannels [38], nanostructures [39], duplex films [40], nanotubes [41] and microcones [43].

In summary, the anodization process is considered a cost-effective and facile method for the fabrication of various structures of niobium oxides including films, nanopores, nanochannels, nanorods, nanotubes and microcones. Each structure can be convenient for a certain application than the other structures. Therefore, the variety of structures formed by anodization opens the way to various uses of niobium oxide materials. Therefore, more studies are required to develop these structures and produce new ones along with investigating the mechanism, parameters and applications of these structures.

3.2.2 Niobium Oxynitrides

As mentioned in chapter two, efficient photocatalysts are required to absorb the visible light with longer wavelengths. The band gaps of stable metal oxides are usually too large to absorb light in the visible region [49]. A reason for this wide band gap can be the low energy of the valence band that is derived from the 2p orbitals of the oxygen atoms [50]. Metal nitrides can solve the problem by raising the position of the valence band as the 2p orbitals of nitrogen atoms have higher potential energy. However, nitrides suffer from the poor stability in aqueous solutions, hence their photocatalytic activity cannot be maintained for long time [51]. For optimizing the reduction in the band gap and the stability in aqueous solutions, metal oxynitrides are proposed as promising photocatalysts. In oxynitrides, the substitution of some O^{-2} by N^{-3} is thought to cause the hybridization of the O 2p orbitals with the N 2p orbitals leading to narrower bandgap by raising the valence band position [52]. The difference in the band gap structure between metal oxides and oxynitrides is illustrated in **Figure 3-14**.

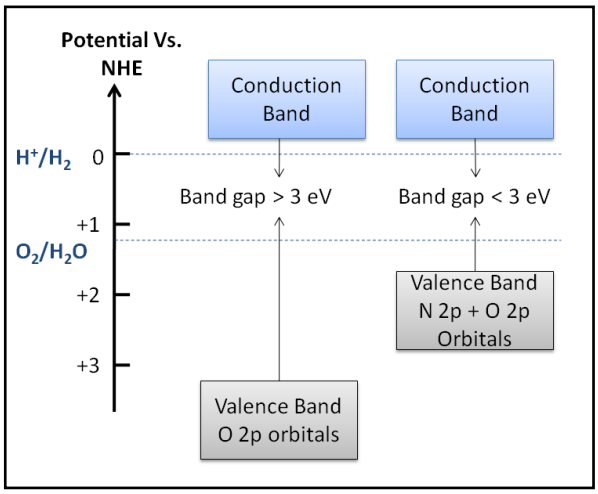

Figure 3-14: Schematic band structure of wide band gap metal oxide and metal oxynitride with reduced band gap.

Several studies have been investigating metal oxynitride photocatalysts for water splitting such as titanium, zinc-germanium, and tantalum [53-57]. Moreover, metal oxynitrides with perovskite structures were investigated for the same application offering Z-scheme system to suppress recombination reactions [58-59]. Most of the oxynitrides that were developed have anionic vacancies that make them n-type semiconductors. The possible combinations of cations and the different oxygen - to - nitrogen ratios offer infinite number of oxynitride materials. Therefore, experimental studies are accompanied by computational work to predict and offer more understanding for the properties of oxynitrides. Wu *et al.* had theoretically studied 68 binary nitrides, 1503 ternary oxynitrides and 1377 quaternary oxynitrides [60].

There are several physical and chemical methods used for the synthesis of metal oxynitrides. One of the most common and facile methods for nitrogen doping is thermal ammonolysis. In this process, the solid oxide material reacts with ammonia gas at constant flow rate at specific temperature and for certain duration. Ammonia decomposes due to the high temperature forming active nitriding species as N, NH and NH_2 as well as H_2 that forms H_2O with the lattice oxygen [58].The formation of the thermodynamically stable H_2O, which is removed continuously by the ammonia flow to prevent the back reaction, and the entropy increase are the driving forces to form oxynitrides [58].

The available literature about niobium oxynitrides is very limited and it is rare in the water splitting field. Schwartz *et al.* showed the formation of niobium oxynitride that had a face-centered cubic structure by thermal annealing of Nb_2O_5 powder in a mixture of gases (20 % NH_3/He) at high temperatures (754 – 900 ^{0}C) and a flow rate of 1000 cm^3/min [61]. Matylitskaya *et al.* explained that thermal annealing of niobium oxide in an

atmosphere of molecular nitrogen did not form oxynitrides because the niobium oxide phases hinder the diffusion of nitrogen [62]. There are different perovskite niobium oxynitride structures that have been reported. Kanade *et al.* fabricated niobium zirconium oxynitride photocatalyst by thermal ammonolysis of $Nb_2Zr_6O_{17}$ powder at 800 ^{0}C reduced the band gap from 3.1 eV to 2.14 eV [63]. Maeda *et al.* studied the photocatalytic application of $SrNbO_2N$ particles [64]. $CaNbO_2N$, $SrNbO_2N$, $BaNbO_2N$, and $LaNbON_2$ were examined by Siritanaratkul *et al.* [65]. Recently, niobium oxynitride films were formed from anodized oxide films (165 nm) by annealing in ammonia (200 cm^3/ min) at temperature range from 450 to 600 ^{0}C for duration range from 5 to 60 minutes [66]. In this study, the authors showed that films annealed at 450 ^{0}C for 20 min produced the highest IPCE% among the films annealed at the other conditions [66]. The XRD spectra for the films annealed in ammonia revealed the generation of multi niobium oxide phases (orthorhombic Nb_2O_5 and tetragonal NbO_2) [66]. In addition, the XPS results showed the presence of NbN in oxynitride films formed at 450 ^{0}C and it is present in higher amount in films annealed at 600 ^{0}C [66]. **Figure 3-15** shows the morphology, the XPS and the IPCE results of the fabricated oxynitrides. It is observed that the photocurrent is about 13 µA for the oxynitride film formed by annealing in ammonia at 450 ^{0}C for 20 minutes.

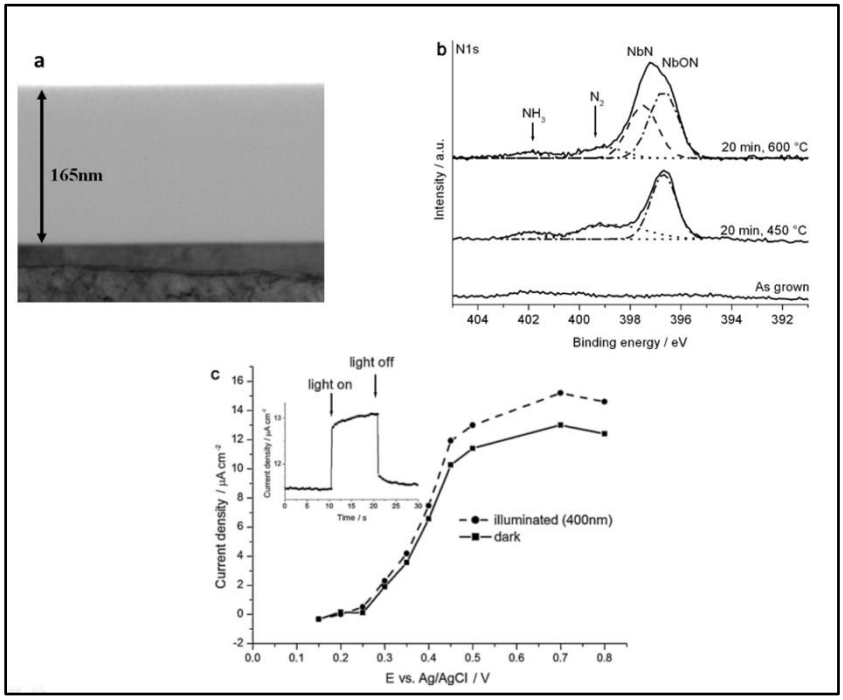

Figure 3-15: Niobium oxynitride thin films as reported by Ruffa *et al.* examined by (a) FESEM, (b) XPS and their photocurrent in 0.1 M Na_2SO_4 solution at 0.5 V is shown in (c) [66].

Although oxynitrides showed higher photocatalytic activity relative to the oxides, their efficiency is still low compared to the expectations drawn from the large band gap reduction. The sequence of the photocatalytic water splitting reactions, explained in chapter 2 can be summarized as: (1) the photocatalyst generates photoexcited electron – hole pair upon absorption of photons with equivalent or higher energy than its band gap, (2) the electron and hole carriers then migrate separately to the surface to create the reaction field and (3) finally, the separated charge carriers cause the oxidation and reduction reactions of water [67-68]. Step 3 is promoted by using a co-catalyst as platinum. However, steps 1 and 2 depend strongly on the structure and the properties of the photocatalyst. The lattice and surface defects as anion vacancies and reduced species

can be the cause that the first two steps be inefficient. For step 1; defects can alter the band structure and block the excitation of electron-hole pairs while for step 2; defects can act as recombination sites stopping the migration of the carriers to undergo step 3 [59-60]. Therefore, a photocatalyst with minimum defects and good crystallinity is required.

For niobium oxynitrides, **Table 3-1** provides the traditional and Kröger-Vink notations of defects in Nb_2O_5 and N-doped Nb_2O_5 systems.

Table 3-1: Traditional and Kröger-Vink notations of defects in Nb_2O_5 and N-doped Nb_2O_5 systems.

Traditional Notation	**Description**	**Kröger-Vink Notation**
Nb_{Nb}^{+5}	Nb^{+5} ion in niobium lattice site	Nb_{Nb}^{x}
Nb_{Nb}^{+4}	Nb^{+4} ion in niobium lattice site	e'
V_{Nb}	Niobium vacancy	V_{Nb}''''
Nb_i^{+4}	Nb^{+4} in an interstitial site	$Nb_i^{\bullet\bullet\bullet\bullet}$
Nb_i^{+5}	Nb^{+5} in an interstitial site	$Nb_i^{\bullet\bullet\bullet\bullet\bullet}$
O_O^{-2}	O^{-2} ion in an oxygen lattice site	O_O^{x}
V_O	Oxygen vacancy	$V_O^{\bullet\bullet}$
O_O^{-}	O^{-} ion in an oxygen lattice site	$h^{\bullet}$
N_O^{-3}	N^{-3} ion in an oxygen lattice site	N_O'''
N_i^{-3}	N^{-3} ion in an interstitial site	$N_i^{\bullet\bullet\bullet}$

Based on the above notations, the basic defect equations in Nb_2O_5 can be written as:

$$O_O^{x} \Longleftrightarrow V_O^{\bullet\bullet} + 2\,e' + \frac{1}{2}O_2$$

$$2\,Nb_{Nb}^{x} + 5\,O_O^{x} \Longleftrightarrow 2\,Nb_i^{\bullet\bullet\bullet\bullet} + 8\,e' + \frac{5}{2}O$$

$$2\,Nb_{Nb}^{x} + 5\,O_O^{x} \Longleftrightarrow 2\,Nb_i^{\bullet\bullet\bullet\bullet\bullet} + 10\,e' + \frac{5}{2}\,O_2$$

$$O_2 \Longleftrightarrow V_{Nb}'''' + 5\,h^{\bullet} + 2\,O_O^{x}$$

$$nil \Longleftrightarrow e' + h^{\bullet}$$

In oxynitrides, some nitrogen ions either substitute oxygen ions or be placed in interstitial sites. The substitution of N^{-3} for O^{-2} can be written, using Kröger-Vink notation, as:

$$Nb_3N_5 \xrightarrow{Nb_2O_5} N_O''' + Nb_{Nb}^{x} + V_{Nb}''''$$

Moriya *et al.* reviewed that in the process of thermal ammonolysis; several causes for the defects can be identified [68]:

(1) Nitridation Conditions: If the process of nitridation is carried out at severe conditions of temperature, flow rate and duration, the material can turn from oxynitride into nitride or a mixture of both. At extreme conditions, the nitride might decompose. Therefore, finding and controlling the optimum conditions for forming stable and pure oxynitride is critical.

(2) Nitridation Homogeneity: A difference in the degree of nitriding the material oxide can occur due to the difference in the contact between the material oxide structure and the reduced NH_3 radicals. Uniform NH_3 flow is required to reach good nitridation homogeneity as much as possible.

(3) Structure Homogeneity: Lattice defects can be formed due to the crystal structure transformation from oxide to oxynitride during nitridation. The substitution of oxygen by nitrogen makes the lattice rigid by enhancing the covalent bonding within it.

Based on the previous literature, oxynitrides are promising photocatalysts but still need more investigations. It can be observed that ordered structures of niobium oxynitrides have not been studied. In addition, most of the studies focused on niobium perovskite oxynitrides although the full understanding of pure niobium oxynitrides is not reported.

References

1. Grimes, C. A.; Mor, G. K. *TiO_2 Nanotube Arrays: Synthesis, Properties, and Applications*; Springer: New York, **2009**.
2. Hassan, N. K.; Hashim, M. R.; Allam, N. K. ZnO nano-tetrapod photoanodes for enhanced solar-driven water splitting. *Chem. Phys. Lett.***2012**, 549, 62–66.
3. Hamedani, H. A.; Allam, N. K.; Garmestani, H.; El-Sayed, M. A. Electrochemical Fabrication of Strontium-Doped TiO_2 Nanotube Array Electrodes and Investigation of Their Photoelectrochemical Properties. *J. Phys. Chem. C* **2011**, 115, 13480–13486.
4. Wei, Y.; Ke, L.; Kong, J.; Liu, H.; Jiao, Z.; Lu, X.; Du, H.; Sun, X. W. Enhanced photoelectrochemical water-splitting effect with a bent ZnO nanorod photoanode decorated with Ag nanoparticles. *Nanotechnology* **2012**, 23, 235401–235408.
5. Jankulovska, M.; Barceló, I.; Lana-Villarreal, T.; Gómez, R. Improving the Photoelectrochemical Response of TiO_2 Nanotubes upon Decoration with Quantum-Sized Anatase Nanowires. *J. Phys. Chem. C***2013**, 117, 4024–4031.
6. Bellingeri, E.; Marré, D.; Pallecchi, I.; Pellegrino, L.; Siri, A. High mobility in ZnO thin films deposited on perovskite substrates with a low temperature nucleation layer. *S. Appl. Phys. Lett.***2005**, 86, 012109–0121011.
7. Kostedt, W. L.; Ismail, A. A.; Mazyck, D. W. Impact of Heat Treatment and Composition of ZnO−TiO_2 Nanoparticles for Photocatalytic Oxidation of an Azo Dye. *Ind. Eng. Chem. Res.***2008**, 47, 1483−1487.

8. Zhang, Q.; Fan, W.; Gao, L. Anatase TiO_2 nanoparticles immobilized on ZnO tetrapods as ahighly efficient and easily recyclable photocatalyst. *Applied Catalysis B: Environmental* **2007**, 76, 168–173.
9. He, Z.; Li, Y.; Zhang, Q.; Wang, H. Capillary microchannel-based microreactors with highly durable ZnO/TiO2nanorod arrays for rapid, high efficiency and continuous-flow photocatalysis. *Applied Catalysis B: Environmental* **2010**, 93, 376–382.
10. Prabakara, K.; Son, M.; Kim, Y.; Kim, H. TiO2 thin film encapsulated ZnO nanorod and nanoflower dye sensitized solarcells, *Materials Chemistry and Physics***2011**, 125, 12–14.
11. Liu, M.; Nam, C.; Black, C. T.; Kamcev, J.; Zhang, L. Enhancing Water Splitting Activity and Chemical Stability of Zinc Oxide Nanowire Photoanodes with Ultrathin Titania Shells. *J. Phys. Chem. C* **2013**, 117, 13396−13402.
12. Liao, D. L.; Badour, C. A.; Liao, B. Q. Preparation of nanosized TiO_2/ZnO composite catalyst and its photocatalytic activity for degradation of methyl orange. *J. Photochem. Photobiol. A* **2008**, 194, 11−19.
13. Lei, Y.; Zhao, G.; Liu, M.; Zhang, Z.; Tong, X.; Cao, T. Fabrication, Characterization, and Photoelectrocatalytic Application of ZnO Nanorods Grafted on Vertically Aligned TiO2 Nanotubes. *J. Phys. Chem. C* 2009, *113*, 19067–19076.
14. Pan, K.; Dong, Y.; Zhou, W.; Pan, Q.; Xie, Y.; Xie, T.; Tian, G.; Wang, G. Facile Fabrication of Hierarchical TiO_2 Nanobelt/ZnO Nanorod Heterogeneous

Nanostructure: An Efficient Photoanode for Water Splitting. *ACS Appl. Mater. Interfaces* ***2013***, 5, 8314−8320.

15. Xiao, F. –X. Construction of Highly Ordered ZnO–TiO_2 Nanotube Arrays (ZnO/TNTs) Heterostructure for Photocatalytic Application.*ACS Appl. Mater. Interfaces***2012**, 4, 7055−7063.
16. Lin, L.; Yang, Y.; Men, L.; Wang, X.; He, D.; Chai, Y.; Zhao, B.; Ghoshroyb, S.; Tang, Q. A highly efficient TiO_2@ ZnO n–p–n heterojunction nanorod Photocatalyst. *Nanoscale* **2013**, 5, 588–593.
17. Naseri, N.; Yousefi, M.; Moshfegh, A. Z. A comparative study on photoelectrochemical activity of ZnO/TiO2and TiO2/ZnO nanolayer systems under visible irradiation, *Solar Energy* 2011, 85, 1972–1978.
18. Zheng, L. R.; Zheng, Y. H.; Chen, C. Q. Network Structured SnO_2/ZnO Heterojunction Nanocatalyst with High Photocatalytic Activity. *Inorg.Chem.***2009**, 48, 1819−1852.
19. Wu, J.; Li, H.; Liu, Y.; Xie, C. Photoconductivity and trap-related decay in porous TiO2/ZnO Nanocomposites. *J. Appl. Phys.* **2011**, 110, 123513-123520.
20. Schrauben, J. N.; Hayoun, R.; Valdez, C. N.; Braten, M.; Fridely, L.; Mayer, J. M. Titanium and Zinc Oxide Nanoparticles Are Proton-Coupled Electron Transfer Agents. *Science* **2012**, 336, 1298–1300.
21. Lee, W. *The anodization of aluminum for nanotechnology applications;* Springer: US, **2011**.

22. Prakasam, H. E.; Shankar, K.; Paulose, M.; Varghese, O. K.; Grimes, C. A.A New Benchmark for TiO_2 Nanotube Array Growth by Anodization. *J. Phys. Chem. C* **2007**, 111, 7235-7241.

23. Chen, C.; Fang, D.; Luo, Z. Fabrication and Characterization of Highly-Ordered Valve-Metal Oxide Nanotubes and Their Derivative Nanostructures. *Reviews in Nanoscience and Nanotechnology*, **2012**, 1, 229-256.

24. Su, Z.; Zhou, W.; Jiang, F.; Hong, M. Anodic formation of nanoporous and nanotubular metal oxides. *J. Mater. Chem.***2012,** 22**,** 535-544.

25. Allam, N. K.; Feng, X. J.; Grimes, C. A. Self-Assembled Fabrication of Vertically Oriented Ta_2O_5 Nanotube Arrays, and Membranes Thereof, by One-Step Tantalum Anodization, *Chem. Mater.* **2008**, *20,* 6477–6481.

26. Tsuchiya, H.; Schmuki, P. Self-organized high aspect ratio porous hafnium oxide prepared by electrochemical anodization. *Electrochemistry Communications***2005**, 7, 49–52.

27. Wei, W.; Lee, K.; Shaw, S.; Schmuki, P. Anodic formation of high aspect ratio, self-ordered Nb_2O_5 nanotubes. *Chem. Comm.***2012**, 48, 4244-4246.

28. Draper, P. H. G.; Harvey, J. The structure of anodic films-I. An electron diffraction examination of the products of anodic oxidation on tantalum, niobium and zirconium. *Acta Metallurgica* **1963**, 11, 873-879.

29. Ono, S.; Kuramochi, K.; Asoh, H. Effects of electrolyte pH and temperature on dielectric properties of anodicoxide films formed on niobium. *Corrosion Science* **2009**, 51, 1513–1518.

30. Choi, J.; Lim, J. H.; Lee, S. C.; Chang, J. H.; Kim, K. J.; Cho, M. A. Porous niobium oxide films prepared by anodization in HF/H_3PO_4, *Electrochimica Acta* **2006**, 51, 5502–5507.

31. Choi, J.; Lim, J. H.; Lee, J.; Kim, K. J. Porous niobium oxide films prepared by anodization–annealing–anodization. *Nanotechnology* **2007**, 18, 055603 – 055609.

32. Yoo, J. E.; Choi, J. Surfactant-assisted growth of anodic nanoporous niobium oxide with a grained surface, *Electrochimica Acta* **2010**, 55, 5142–5147.

33. Choi, J.; Lim, J. H.; Rho, S.; Jahng, D.; Lee, J.; Kim, K. J. Nanoporous niobium oxide for label-free detection of DNA hybridization events, *Talanta* **2008**, 74, 1056–1059.

34. Abdul Rani, R.; Zoolfakar, A. S.; Ou, J. Z.; Field, M. R.; Austin, M.; Kalantar-zadeh, K. Nanoporous Nb_2O_5 hydrogen gas sensor. *Sensors and Actuators B* **2013**, 176, 149– 156.

35. Lee, K.; Yang, Y.; Yang, M.; Schmuki, P. Formation of Highly Ordered Nanochannel Nb Oxide by Self-Organizing Anodization, *Chem. Eur. J.* **2012**, 18, 9521 – 9524.

36. Ou, J. Z.; Rani, R. A.; Ham, M. H.; Field, M. R.; Zhang, Y.; Zheng, H.; Reece, P.; Zhuiykov, S.; Sriram, S.; Bhaskaran. M.; Kaner, R. B.; Kalantar-zadeh, K. Elevated Temperature AnodizedNb_2O_5: A Photoanode Material with Exceptionally Large Photoconversion Efficiencies. *ACS Nano* **2012**, 6, 4045–4053.

37. Barredo-Damas, S.; Lee, K.; Kirchgeorg, R.; S´anchez-Tovar, R.; Schmuki, P. Transparent Self-Ordered Niobium-Oxide Nanochannel Layers Formed on

Conducting Glass by Total Anodization of Thin Metal Films in Glycerol/Phosphate Electrolyte. *ECS Electrochemistry Letters* **2013,** 2, C4-C6.

38. Abdul Rani, R.; Zoolfakar, A. S.; Jian Zhen Ou, Kadir, R. A.; Nili, H.; Latham, K.; Sriram, S.; Bhaskaran, M.; Zhuiykov, S.; Kanerad, R. B.; Kalantar-zadeh, K. Reduced impurity-driven defect states in anodized nanoporous Nb_2O_5: the possibility of improving performance of photoanodes, *Chem. Commun.* **2013**, 49, 6349 – 6351.
39. Kim, H., Yoo, J. E.; Park, J., Seo, E. W., Choi, J. Formation of Niobium Oxide Film with Duplex Layers by Galvanostatic Anodization. Bull. Korean Chem. Soc. 2012, 33, 2675 – 2678.
40. Rodrigues, C.;Tacconi, N. R.;Chanmanee, W.;Rajeshwar, K. Cathodic Electrosynthesis of Niobium Oxide One-Dimensional Nanostructures with Tailored Dimensions. *Electrochem. Solid-State Lett.* **2010**, 13, B69-B72.
41. Karlinsey, R. L. Preparation of self-organized niobium oxide microstructures via potentiostatic anodization, Electrochemistry Communications 2005, 7, 1190–1194.
42. Oikawa, Y.; Minami, T.; Mayama, H.; Tsujii, K.; Fushimi, K.; Aoki, Y.; Skeldon, P.; Thompson, G.E.; Habazaki; H. Preparation of self-organized porous anodic niobium oxide microcones and their surface wettability. Acta Materialia 2009, 57, 3941–3946.
43. Yang, S.; Aoki, Y.; Habazaki, H. Effect of electrolyte temperature on the formation of self-organized anodic niobium oxide microcones in hot phosphate–glycerol electrolyte. *Applied Surface Science* 2011, 257, 8190– 8195.

44. Yang, S.; Habazaki, H.; Fujii, T.; Aoki, Y.; Skeldon, P.; Thompson, G. E. Control of morphology and surface wettability of anodic niobium oxide microcones formed in hot phosphate–glycerol electrolytes. *Electrochimica Acta* **2011**, 56, 7446– 7453.

45. Karlinsey, R. L.; Hara, A. T.; Yi, K.; Duhn, C. W. Bioactivity of novel self-assembled crystalline Nb_2O_5 microstructures in simulated and human salivas. *Biomed. Mater* **2006**, 1, 16–23.

46. Zhao, J.; Wang, X.; Xu, R.; Mi, Y.; Li, Y. Preparation and Growth Mechanism of Niobium Oxide Microcones by the Anodization Method. *Electrochemical and Solid-State Letters* **2007**, 10, C31-C33.

47. Karlinsey, R. L. Self-assembled Nb2O5 microcones with tailored crystallinity. *J Mater Sci* **2006**, 41, 5017–5020.

48. Jeong, B.-Y.; Jung, E. H. Micro-Mountain and Nano-Forest Pancake Structure of Nb2O5 with Surface Nanowires for Dye-Sensitized Solar Cells. *Met. Mater. Int.* **2013**, 19, 617-62.

49. Maeda, K.; Domen, K. New Non-Oxide Photocatalysts Designed for Overall Water Splitting under Visible Light. *J. Phys. Chem. C* **2007**, 111, 7851-7861.

50. Scaife, D. E. Oxide Semiconductor in Photoelectrochemical Conversion of Solar Energy. *Solar Energy* **1980**, 25, 41-54.

51. Yokoyama, D.; Hashiguchi, H.; Maeda, K.; Minegishi, T.; Takata, T.; Abe, R.; Kubota, J.; Domen, K. Ta_3N_5 photoanodes for water splitting prepared by sputtering. *Thin Solid Films* **2011**, 519, 2087–2092.

52. Asahi, R.; Morikawa, T.; Ohwaki, T.; Aoki, K.; Taga, Y. Visible-Light Photocatalysis in Nitrogen-Doped Titanium Oxides. *Science* **2001**, 293, 269-271.

53. Torres, G. R; Lindgren, T.; Lu, 1. J.; Granqvist, C., -G. 1.; Lindquist, S., -E. Photoelectrochemical Study of Nitrogen-Doped Titanium Dioxide for Water Oxidation. J. Phys. Chem. B ***2004***, 108, 5995-6003.

54. Allam, N. K.; Poncheri, A. J.; El-Sayed, M. A. Vertically Oriented Ti-Pd Mixed Oxynitride Nanotube Arrays for Enhanced Photoelectrochemical Water Splitting. *ACS Nano* **2011**, 6, 5056-5066.

55. Lee, Y.; Terashima, H.; Shimodaira, Y.; Teramura, K.; Hara, M.; Kobayashi, H. Domen, K.; Yashima, M.; Zinc Germanium Oxynitride as a Photocatalyst for Overall Water Splitting under Visible Light. *J. Phys. Chem. C* **2007**, 111, 1042-1048.

56. Abe, R.; Higashi, M.; Domen, K. Facile Fabrication of an Efficient Oxynitride TaON Photoanode for Overall Water Splitting into H_2 and O_2 under Visible Light Irradiation. *J. AM. CHEM. SOC.* **2010**, 132, 11828–11829.

57. Ebbinghausa, S. G.; Abichta, H.-P.; Dronskowskib, R., Mullera, T.; Rellerc, A. Weidenkaff, A. Perovskite-related oxynitrides – Recent developments in synthesis, characterisation and investigations of physical properties. *Progress in Solid State Chemistry* **2009**, 37, 173–205.

58. Maeda, K. Z‐Scheme Water Splitting Using Two Different Semiconductor Photocatalysts. *ACS Catal*. **2013**, 3, 1486−1503.

59. Finazzi, E.; Valentin, C. D. First-Principles Study of Nitrogen Doping at the Anatase TiO_2 (101) Surface Electronic Structure, Chemical Bonding, and High-Pressure, *J. Phys. Chem. C* **2007**, 111, 9275-9282.

60. Wu, Y.; Lazic, P.; Hautier, G.; Persson, K.; Ceder, G. First principles high throughput screening of oxynitrides for water-splitting photocatalysts. *Energy Environ. Sci.* **2013,** 6**,** 157-168.

61. Schwartz, V.; Oyama, S. T. Study of Niobium Oxynitride: Synthesis, Characterization, and Reactivity. *Chem. Mater.* **1997**, 9, 3052-3059.

62. Matylitskaya, V. A.; Bock, W.; Kolbesen, B. O. Nitridation of niobium oxide films by rapid thermal processing, *Anal. Bioanal.Chem* **2008**, 390, 1507-1515.

63. Kanadea, K.G.; Baega,, J. -O.; Kalec, B.B.; MiLeea, S.; Moona, S. –J.; Kong, K.-J. Rose-red color oxynitride $Nb_2Zr_6O_{17-x}N_x$: A visible light photocatalyst to hydrogen production, *International Journal of Hydrogen Energy* **2007**, 32, 4678 – 4684.

64. Maeda, K.; Higashi, M.; Siritanaratkul, B.; Abe, R.; Domen, K. $SrNbO_2N$ as a Water-Splitting Photoanode with a Wide Visible-Light Absorption Band. *J. Am. Chem. Soc.* **2011**, 133, 12334–12337.

65. Siritanaratkul, B.; Maeda, K.; Hisatomi, T.; Domen, K. Synthesis and Photocatalytic Activity of Perovskite Niobium Oxynitrides with Wide Visible-Light Absorption Bands. *Chem. Sus. Chem.* **2011**, 4, 74–78.

66. Ruffa, T.; Hahna, R.; Killiana, M.S.; Asohb, H.; Onob, S.; Schmuki, P. Visible light photo response from N-doped anodic niobium oxide after annealing in ammonia atmosphere, *Electrochimica Acta* **2012**, 62 402–407.

67. Maeda, K. (Oxy) nitrides with d0-electronic configuration as photocatalysts and photoanodes that operate under a wide range of visible light for overall water splitting. *Phys. Chem. Chem. Phys.* **2013**, 15, 10537-10548.

68. Moriya, Y.; Takata, T.; Domen, K. Recent progress in the development of (oxy) nitride photocatalysts for water splitting under visible-light irradiation. *Coordination Chemistry Reviews* **2013**, 257, 1957–1969.

Chapter 4

Experimental Methods and Materials

4.1 Materials and Supplies

Titanium and Niobium metal foils with thickness 0.25 mm and purity of 99.95 % were purchased from Alfa Aesar. Sputtering targets of Ti, Zn, and ZnO were purchased from Sigma Aldrich with purity 99.99 %. Anhydrous Ammonia gas cylinders were purchased from Airgas company. Sputtering and Nitridation processes were done in collaboration with Georgia Institute of Technology and California Institute of Technology.

4.2 Potentiostatic Anodization

Prior to anodization, Ti and Nb foils were ultrasonically cleaned in acetone, ethanol and finally in distilled water. The anodization electrochemical cell was constructed from Platinum foil (counter electrode) and cleaned Ti or Nb foil (working electrode). Both electrodes were immersed in fluoride-containing electrolytes at room temperature (approximately 22°C). Constant voltage was applied between the two electrodes using Agilent E3612A DC power supply. After anodization, the samples were rinsed thoroughly with acetone and distilled water and then were left to dry in air. **Figure 4-1** shows the anodization setup.

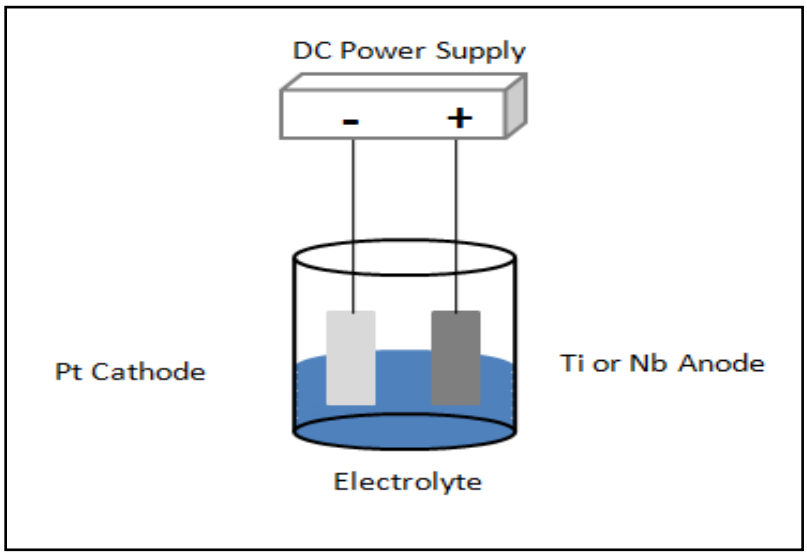

Figure 4-1: The anodization setup using two-electrode electrochemical cell.

4.3 Plasma Sputtering

Based on the explanation of the sputtering technique in chapter 2, RF sputtering technique was used to cover the TiO_2 nanotubes with a shell of ZnO layer as it is not a good electric conductor. The TiO_2 nanotubes grown on Ti film were used as the substrate in Denton Discovery RF/DC Sputterer with a target made of ZnO. The sputtering chamber was filled with argon and oxygen atmosphere at a flow rate of 20 sccm. The argon gas was used to create the plasma and oxygen was pumped into the chamber to promote the formation of the zinc oxide shell on the TiO_2 nanotubes. The chamber was vacuumed to a pressure of 4×10^{-5}Torr while the pressure of the chamber was kept at 6 mTorr during sputtering. To form various thicknesses of ZnO shells at 125 watt, the time of sputtering was altered to be 18, 35 and 53 minutes. The two main steps for the fabrication of the TiO_2/ZnO core – shell structure are shown in the **Figure 4-2**.

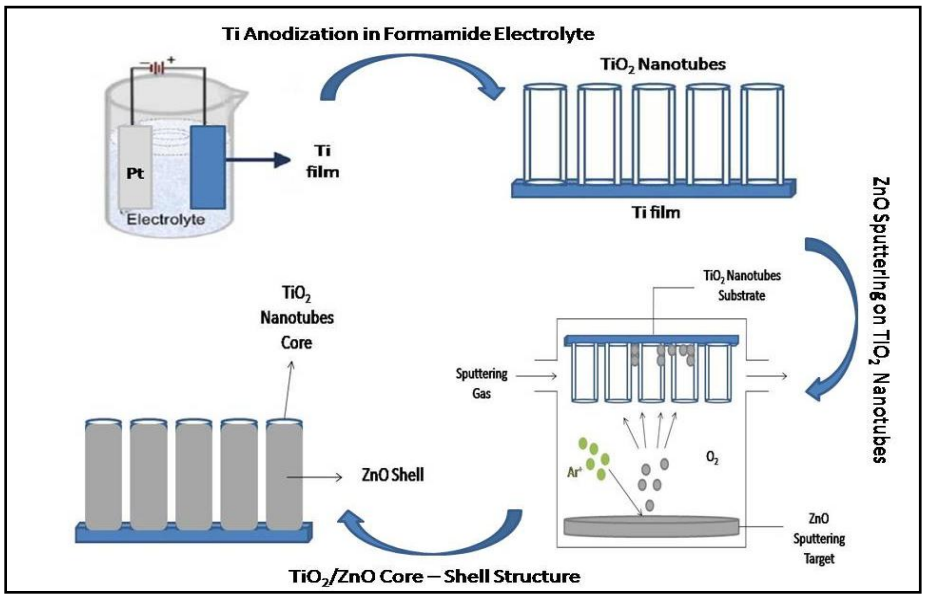

Figure 4-2: The fabrication steps (anodization and sputtering) used to synthesize the TiO_2/ZnO core - shell heterojunctions [1].

Alloys of Titanium – Zinc were fabricated using a DC sputtering technique as both targets are metals. Titanium target was powered at 100 watt while having the zinc target at 30 watt to form a titanium alloy with some percentage of zinc. To form alloy of zinc with some percentage of titanium, the zinc target was powered at 100 watt while having the titanium target at 30 watt. Sputtering was done on pieces of titanium foil at pressure of 10 mTorr with argon flow at 10 sccm.

4.4 Morphological and Crystal Structure Characterization

The morphology and the composition of the samples were examined using a field emission scanning electron microscope FESEM-Zeiss SEM Ultra 60 and FESEM- Zeiss 1550 VP equipped with EDS (Energy dispersive X-ray spectroscopy) detector. Additional morphological analysis was done on Bruker Dimension AFM (Atomic Force Microscope). The crystalline phases were detected and identified on Panalytical X'Pert

Pro diffractometer with Cu Kα radiation. The compositional analysis of the samples was investigated using X-ray photoelectron spectroscopy (XPS) on a Thermo Scientific K-alpha XPS with an Al anode. The spectra were charge referenced to O 1s at 532 eV. XPS analysis for niobium - based samples were done on Surface Science M-Probe ESCA/XPS and the spectra were charge referenced to C 1s at 285 eV. Raman measurements were performed on a Raman microscope (ProRaman-L Analyzer) with an excitation laser beam wavelength of 532 nm.

4.5 Thermal Annealing

The as-anodized samples were subject to thermal annealing in a furnace with constant flow of chosen gas maintained during the annealing process for different time intervals with heating and cooling rates of 1^0C/ min. For the nitridation of niobium oxides into niobium oxynitrides, the as-anodized Nb_2O_5 samples were inserted in a quartz tube to be heated in a tube furnace at 450 ^{0}C with heating and cooling rates of 5 ^{0}C/ min for different time intervals. Ammonia gas was used to flow into the quartz tube during the annealing process at rates 50, 200 and 300 sccm.

4.6 Optical and Photoelectrochemical Measurements

The optical characterization of the TiO_2 – ZnO samples was performed using a Shimadzu UV−vis−NIR spectrophotometer with a solid-sample holder for reflectance measurements and an integrating sphere. Cary 5000 UV/vis/NIR spectrophotometer with integrating sphere was used for the optical characterization of the Nb_2O_5 and Nb – O – N samples. To prepare the sample for the photoelectrochemical measurements, copper contacts were drawn from the annealed samples with conducting silver epoxy and then were connected as the working electrode into three-electrode electrochemical cell.

Saturated Ag/AgCl was used as a reference electrode and platinum foil was used as a counter electrode. Photoelectrochemical properties were investigated in 0.5 M Na_2SO_4 solution for the TiO2 – ZnO photoanodes. For the Nb_2O_5 and Nb – O – N photoanodes, the photoelectrochemical properties were investigated in 0.1 M Na_2SO_4 solution (pH 4 was adjusted by concentrated H_2SO_4 drops). A scanning potentiostat (CH Instruments, model CHI 600B) was used to measure dark and illuminated currents at a scan rate of 10 mV/s. A 300W xenon lamp (Spectra physics) was used as the light source, with AM 1.5 filter (Oriel) used to restrict the incident light to UV wavelengths between 320 and 400 nm. The incident power was determined as 100 mW cm^{-2} using a power detector (Spectra Physics, CA, USA). The setup for the photoelectrochemical measurements is illustrated in **Figure 4-3**.

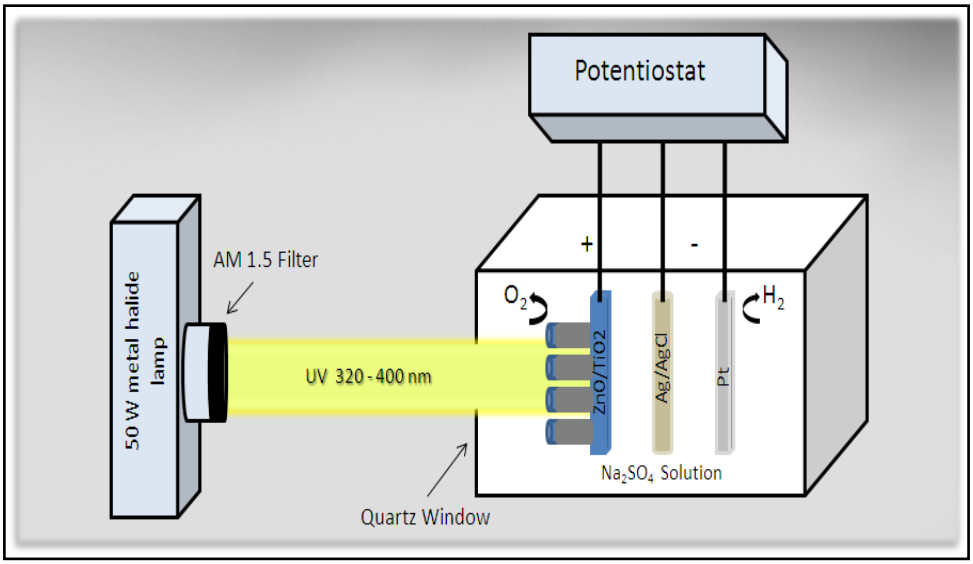

Figure 4-3: Illustrative drawing of the experimental set-up for hydrogen generation by water photoelectrolysis.

References

1. Shaheen, B.S.; Salem, H. G.; El-Sayed, M. A.; Allam, N. K. Thermal/Electrochemical growth and characterization of one dimensional ZnO/TiO_2 hybrid nanoelectrodes for solar fuel production. *J. Phys. Chem C* **2013**, 117, 18502-18509.

Chapter 5

One-Dimensional ZnO/TiO_2 Hybrid Nanoelectrodes for Solar Fuel Production

Based on the discussion in chapter 3, it is still not clear whether having a system of ZnO core with a TiO_2 shell will have better photocatalytic performance or a system with TiO_2 core and ZnO shell is the best. Since both materials have wide band gap, it is not expected to have significant enhancement in absorption when combining TiO_2 and ZnO in a core-shell structure. However, the enhancement is thought to be in promoting fast transport of charge carriers and increasing the stability in aqueous solutions. Hence, the question is: in which system will the charge transport due to difference in band positions be faster and have good stability leading to higher efficiency?

In an attempt to reach an answer, two alloys of Ti and Zn were formed by DC sputtering so that one of them is Zn-rich with some amount of Ti, while the other alloy is Ti-rich with some amount of Zn. The sputtered alloys were in the form of thin films that were difficult to be oxidized by anodization to get uniform structure. Higher film thickness was essential to form oxide structures. In order to search for an answer of the better combination far from the morphology enhancement, the thin films were turned into oxides by thermal annealing. **Figure 5-1** and **Figure 5-2** show the EDX analysis of Zn – 13.6 wt. % Ti shows that of Ti – 11.29 wt. % Zn. **Figure 5-3** shows the measured photocurrent versus time for the oxide films of the alloys at 0.5 V in 0.5 M Na_2SO_4.

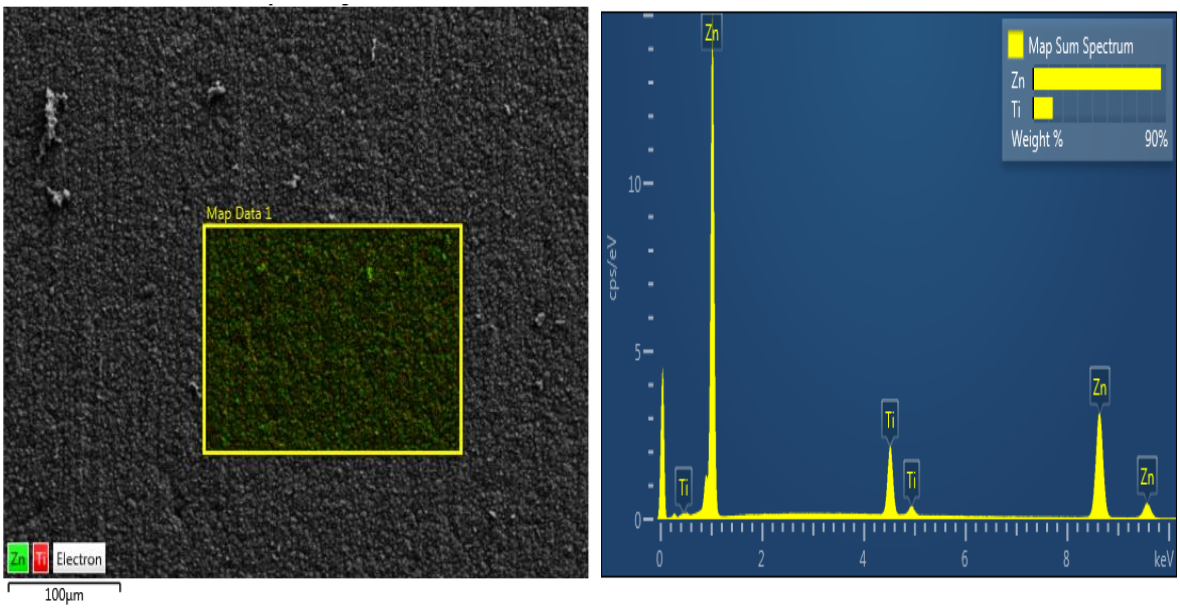

Figure 5-1: EDX analysis of Zn – 13.6 wt. % Ti alloy formed by DC sputtering.

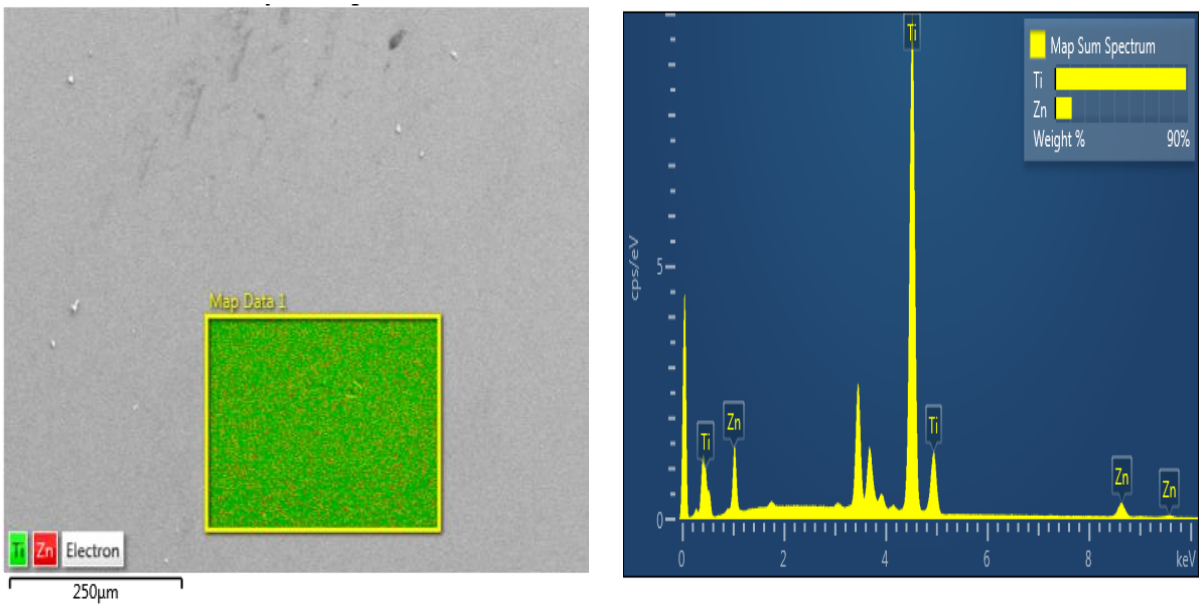

Figure 5-2: EDX analysis of Ti – 11.29 wt. % Zn alloy formed by DC sputtering.

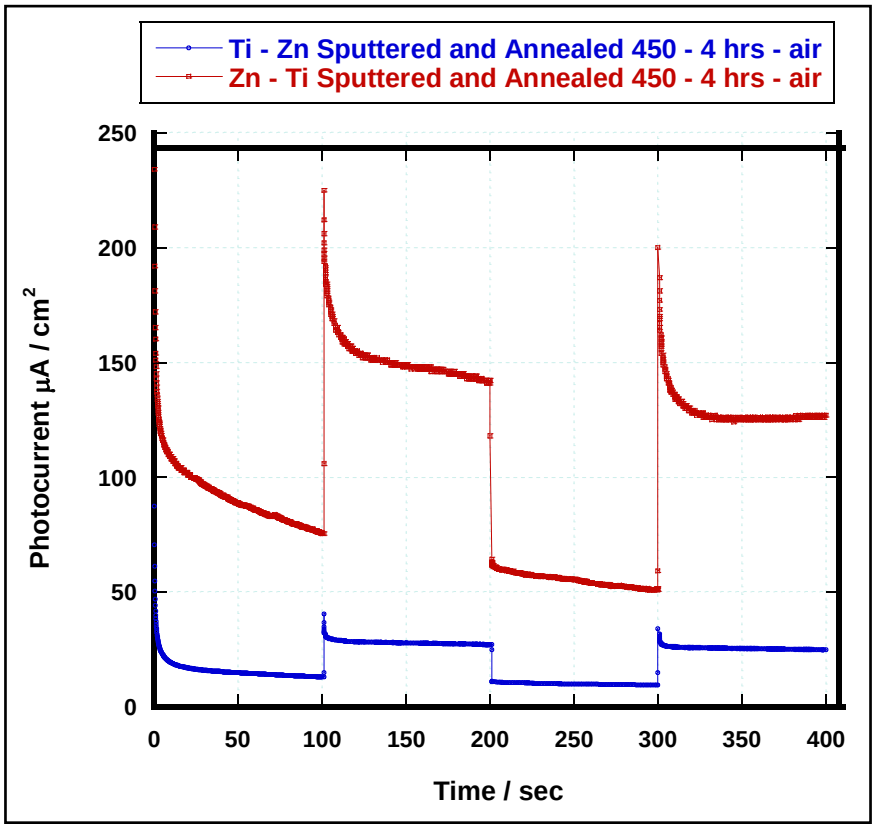

Figure 5-3: Photocurrent-time curve for oxide films of Zn – 13.6 wt. % Ti and Ti – 11.29 wt. % Zn measured in 0.5 Na_2SO_4solution at 0.5 V.

The oxide film of Zn – 13.6 wt. % Ti produced higher photocurrent than that produced by the oxide film of Ti – 11.29 wt. % Zn. The ZnO contribution to enhance the charge separation has high effect on the photoelectrochemical properties. This finding was a motive to study the structure of ZnO shell over a TiO_2 core. It is expected that one-dimensional (1D) ZnO/TiO_2 heterojunction electrodes will have better charge transfer properties than their powder and thin film counterparts. Herein, the results of fabrication of such 1D ZnO/TiO_2 heterojunction electrodes *via* the thermal evaporation of ZnO layers, with different thicknesses, on the surface of anodically fabricated titania nanotube arrays are reported. The rational behind the use of ZnO as an outer layer is the fact that the potentials of the CB and the VB of ZnO are slightly more negative than those of TiO_2.

Therefore, upon excitation, ZnO is excited first with the generated electrons being injected into the CB of TiO_2, in a way similar to photosensitizes. In this way, the use of ZnO as a shell can also serve as a favorable hole-channel for efficient separation of photogenerated charge carriers.

5.1 Morphological and Structural Characterization

As the anodization of titanium in aqueous electrolytes usually results in the formation of short nanotubes with irregular outer diameters that contain ridges and circumferential serrations, the anodization was performed in formamide-based electrolytes. Anodization in formamide is well-known to result in the formation of smooth nanotubes several microns in length. This morphology is achieved by reducing the changes in pH and suppresses the local concentration fluctuations during the anodization process [1].

Figure 5-4 shows the morphology of the as-grown TiO_2 nanotubes and ZnO/TiO_2 nanotube heterojunctions. Figure 1a shows the formation of highly ordered, vertically oriented TiO_2 nanotube arrays on Ti foil. The nanotubes are uniform and cover the entire surface with average diameter of 139 ± 10 nm and average length of 1.9 ± 0.2 μm that cover the entire surface. Figure 1 panels b-d show the morphology of the ZnO/TiO_2 heterojunctions formed via the sputtering of ZnO for 18, 35 and 53 min, respectively over the surface of the as-anodized titania nanotubes depicted in panel a. Note the pronouncing effect of the sputtering time on the morphology and thickness of the ZnO layer formed on top of the titania nanotubes. While sputtering for 18 min resulted in the formation of scattered tiny ZnO particulates on the surface of the tubes, complete coverage of the nozzles of the nanotubes along with agglomeration of the ZnO particles is evident upon

the sputtering for 53 min. Note that in all cases the nanotubular structure is still preserved as can be seen in panels b, c and the inset image in panel d. To have an estimate of the ZnO sputtered film thickness, the sputtering process, under the same conditions, was repeated on glass substrates. The thickness, measured by Tencor P15 Profilometer, was ~100, 200 and 300 nm for the films sputtered for 18, 35, and 53 min, respectively. Note that measuring the thickness of the ZnO film sputtered on TiO_2 nanotubes was very difficult due to the variation in the degree of roughness.

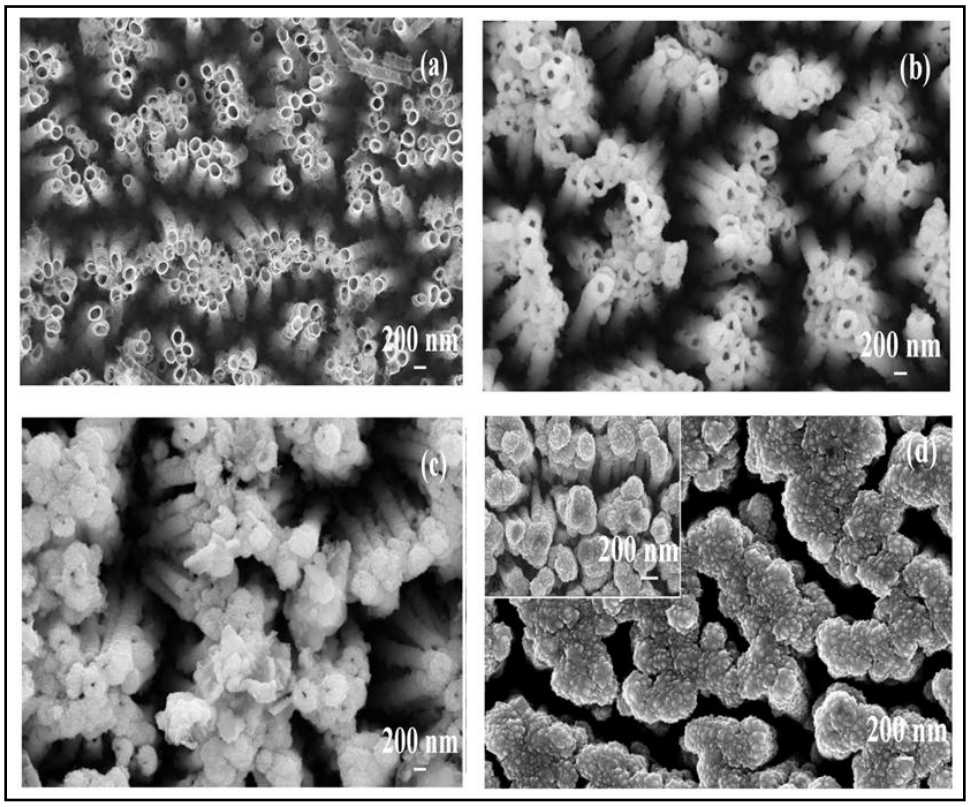

Figure 5-4: FESEM top-view images of (a) as-anodized TiO_2 nanotubes, and the ZnO/TiO_2 nanotubes heterojunctions formed via the sputtering of ZnO for (b) 18, (c) 35 and (d) 53 min, respectively on the as-anodized titania nanotube films.

In order to investigate the effect of crystallinity of TiO_2 the nanotubes on the morphology of the thermally evaporated ZnO, we repeated the sputtering experiments on nanotube films that are previously annealed in air for 4h at 450 ^oC with a heating and cooling rates of 1^oC/min. **Figure 5-5** shows the FESEM images of the obtained heterojunctions. It can be seen that the sputtered ZnO layer takes the same shape of the titania nanotubes forming a core-shell structure for the 18 and 35 min-sputtered samples, Figure 5-5 panels b, c. However, sputtering ZnO for 53 min (Figure 5-5 panel d) resulted in the formation of foam-like ZnO clusters over the titania nanotube surface. Mechanically cracked cross-sectional view showed the formation of core-shell structure, similar to that formed at 18 min, followed by ZnO clustering near the surface.

The glancing angle x-ray diffraction (GAXRD) patterns of the pure TiO_2 nanotubes and the ZnO/TiO_2 nanotube heterojunctions sputtered at different times are shown in **Figure 5-6**. Curve (a) obviously confirms the crystallization of the titania nanotubes in the regular anatase phase [1-2] with the appearance of the characteristic diffraction peaks at 25.3°, 37.7°, 47.8°, 53.8°, and 54.9°, corresponding to the (101), (004), (200), (105), and (211) facets, respectively. The diffraction patterns obtained for the ZnO/TiO_2 heterojunctions (curves b - d) showed the same characteristic peaks for anatase along with some new peaks. Note that the diffraction peak characteristic of the (004) facet is little bit shifted towards higher 2θ values in the heterojunction films compared to that for the pure titania film. It is also interesting to note the appearance of an additional anatase peak at 53.3° corresponding to the (103) facets [3] in all heterojunction films. The 18 min-heterojunction film showed identical pattern to that of pure titania along with the (103) anatase peak. However, the 35 and 53 min-

heterojunction films showed additional peaks at 31.9° and 34.4°, corresponding to (100) and (002) facets of ZnO, respectively [4]. Furthermore, the 53 min-heterojunction showed another diffraction peak at 36.4°, which can be assigned to the (101) facet of ZnO [4]. Therefore, the XRD investigation confirms the formation of ZnO/TiO_2 heterojunctions.

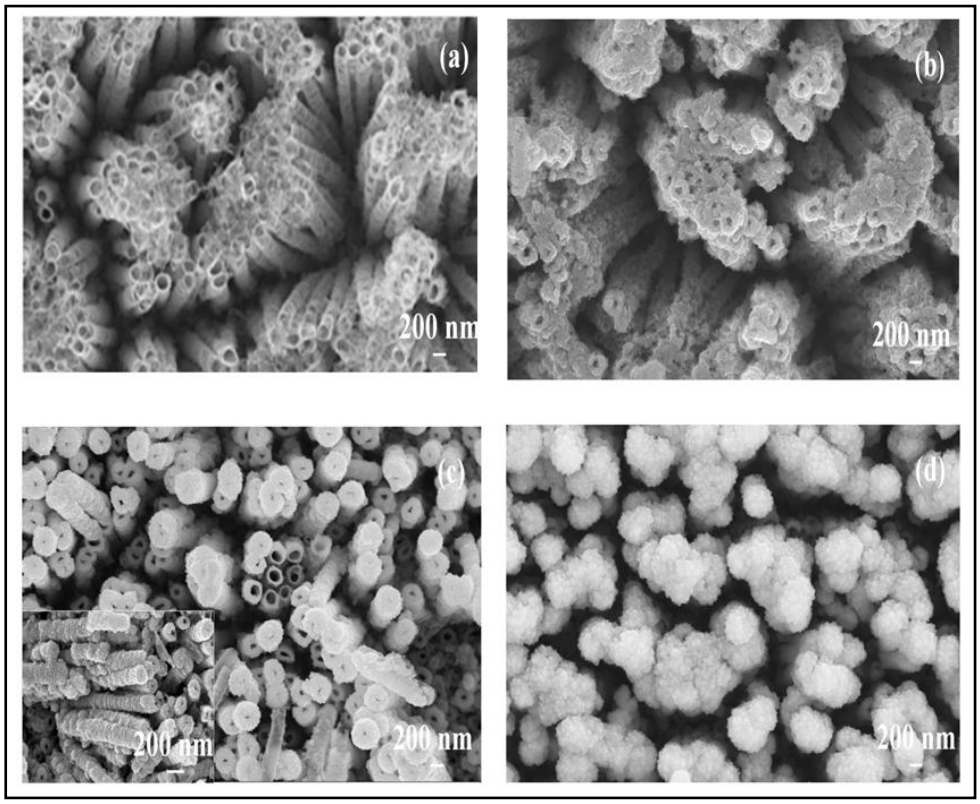

Figure 5-5: FESEM top-view images of (a) TiO_2 nanotubes after annealing for 4h at 450 ^oC, and the ZnO/TiO_2 nanotubes heterojunctions formed via the sputtering of ZnO for (b) 18, (c) 35 and (d) 53 min, respectively on the annealed titania nanotube films.

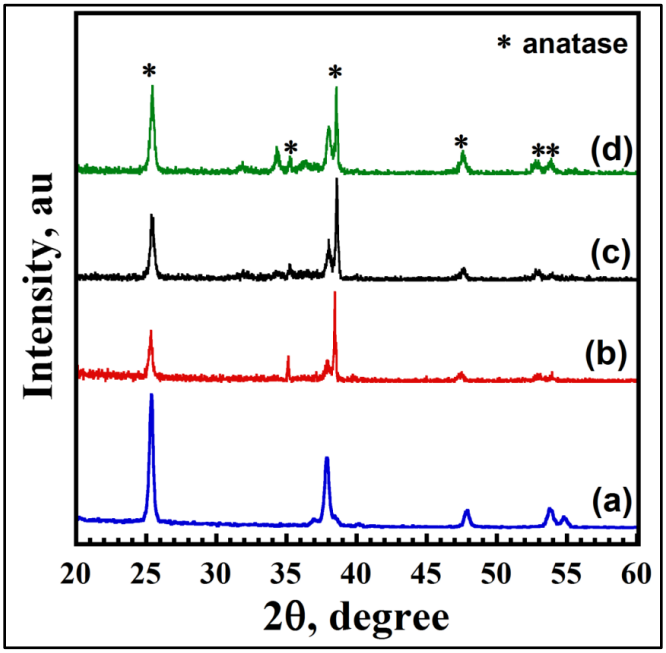

Figure 5-6: GAXRD diffraction patterns of (a) annealed TiO_2 nanotubes (450 ^oC, 4h) and ZnO/TiO_2 nanotube heterojunctions formed via the sputtering of ZnO for (b) 18, (c) 35 and (d) 53 min, respectively on annealed TiO_2 nanotube films.

To investigate the surface composition of the ZnO/TiO_2 heterojunctions, x-ray photoelectron spectroscopy (XPS) analysis was performed. **Figure 5-7A** shows the Ti 2p spectra obtained from pure titania nanotubes (as a reference) as well as the ZnO/TiO_2 heterojunctions fabricated at different sputtering times (panels a-c). Two peaks can be distinguished in all cases that can be assigned to Ti $2p_{3/2}$ and Ti $2p_{1/2}$ photoemission spectra. These two peaks were located at 459.4 and 465.3 eV for the pure titania nanotubes sample with a spin-orbit splitting of 5.7 eV, confirming that both signals correspond to Ti^{4+} [5]. The 18 min-heterojunction showed almost the same peaks (panel a) as those of pure titania nanotubes with only a small shift in the peak positions (459.2 and 464.7 eV for Ti $2p_{3/2}$ and Ti $2p_{1/2}$ photoemission spectra, respectively). However, as

the sputtering time of ZnO layer increases (and consequently the amount of ZnO), the peaks become broader and significantly shifted from those of pure titania. Note the diminishment of the Ti $2p_{1/2}$ peak for the 53 min-heterojunction (panel c). The high-resolution spectrum of Zn 2p is depicted in **Figure 5-7B**, where doublet peaks are observed at around 1045.2 and 1022.1 eV that are characteristic of Zn $2p_{1/2}$ and Zn $2p_{3/2}$, respectively. A spin orbit splitting of 23.1 eV suggests the existence of Zn species in the chemical state of Zn^{2+} [5]. It is important to note that well-defined peaks are obtained for all heterojunctions with a minimal shift in the binding energy. Also, the intensity of the peaks increases with increasing the ZnO sputtering time. Similarly, the high-resolution spectra of O 1s are shown in **Figure 5-7C**, where doublet peaks are observed at approximately 530.6 and 532.4 eV. While the first peak at 530.6 eV can be assigned to lattice oxygen in the ZnO and TiO_2, i.e., Ti−O and Zn−O [5], the second peak at 532.4 eV can be assigned to the oxygen in the hydroxyl groups at the surface of ZnO and TiO_2, i.e., Ti-OH and Zn-OH [5-6]. It is worthy to note that the O1s spectra recorded for the 53 min-heterojunction (Figure 5-4C, panel c) showed a diminishment in the second peak with a slight shift towards lower binding energy compared to the peaks obtained for the 18 and 35-min heterojunctions. In general, the observed small shift in the binding energies of Ti 2p, Zn 2p and O 1s, in the heterojunction films compared to pure oxides, can be related to the slight difference in the electronegativity values of Zn (1.6) as compared to that of Ti (1.5). Therefore, the XPS analysis confirmed the formation of ZnO/TiO_2 nanotube heterostructures, which is in a good agreement with the XRD and SEM results.

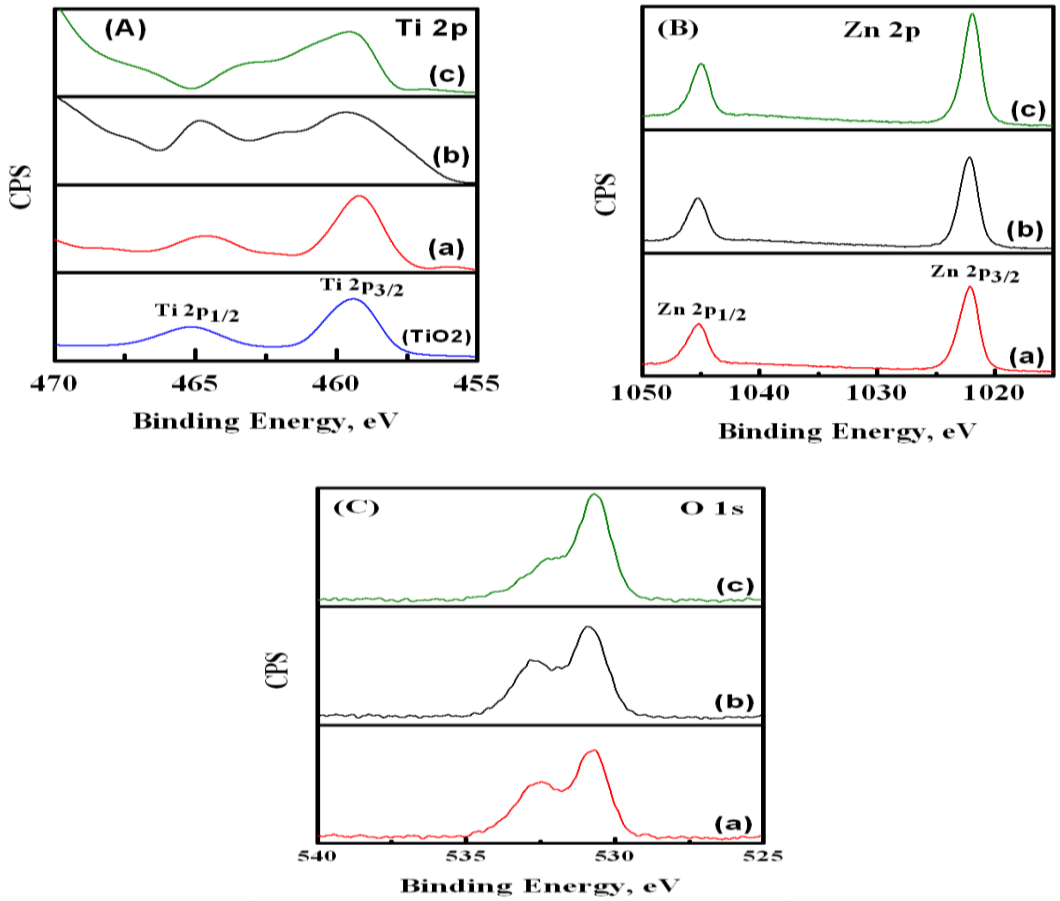

Figure 5-7: XPS spectra of the (A) Ti 2p, (B) Zn 2p and (C) O 1s emission peaks for ZnO/TiO_2 heterojunctions formed via sputtering ZnO for (a) 18, (b) 35 and (c) 53 min, respectively on annealed TiO2 nanotube films.

Raman-scattering is another effective technique to investigate the crystallinity and the vibrational properties of materials as the Raman signals are very sensitive to the crystal structure and defects. **Figure 5-8** shows the obtained results upon testing the 450 ^{o}C-annealed titania nanotubes and the corresponding ZnO/TiO_2 heterojunction films. For the sake of comparison, the Raman spectra of ZnO on both Ti and Zn substrates are included. The remarkable E_g, E_g, B_{1g}, and A_{1g}anatase tetragonal vibration modes of TiO_2 can be clearly seen at 144, 391, 514, and 636 cm^1, respectively [7]. Upon the sputtering of ZnO to form the ZnO/TiO_2 heterojunctions, the anatase peaks start to diminish except for the two peaks at 144 and 636 cm^{-1}. This annihilation in the peaks intensity increases

with increasing the amount of sputtered ZnO, panels a-c in Figure 5-5. Note the appearance of a weak peak at 197 cm^{-1}, which corresponds to the anatase E_g mode [7]. Three new pronounced peaks can be distinguished at 745, 1053 and 1118 cm^{-1}. Those three peaks were also detected for the ZnO deposited on Ti and Zn substrates, suggesting that those peaks are related to vibrational modes of ZnO. The three peaks are close to those reported by Hu *et al.* [8]. Note the absence of the E_1(LO) mode at 578 cm^{-1}, usually associated with defects, indicating the high quality of the sputtered ZnO layers [9].

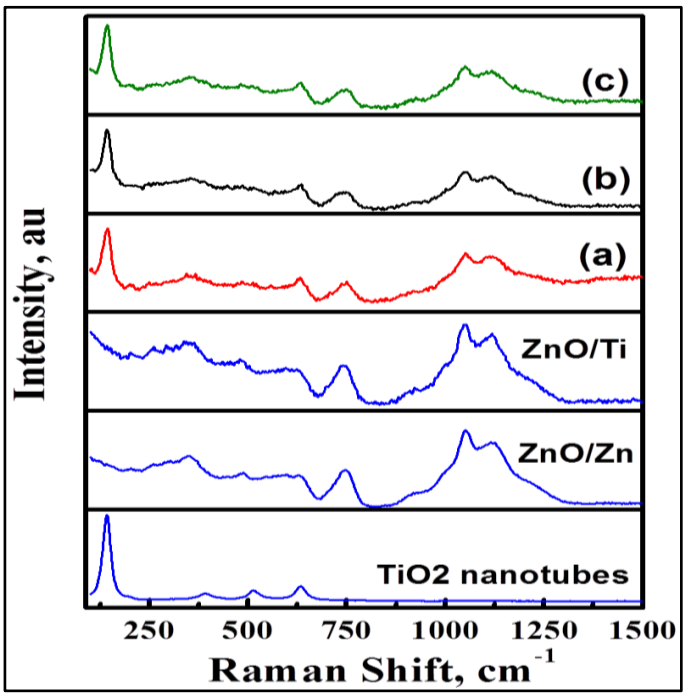

Figure 5-8: Raman spectra of pure TiO_2, ZnO/Zn, ZnO/Ti, and ZnO/TiO_2 heterojunctions formed via sputtering ZnO for (a) 18, (b) 35 and (c) 53 min, respectively on annealed TiO_2 nanotube films.

5.2 Optical and Photoelectrochemical Characterization

Figure 5-9 shows the typical UV-vis diffuse reflectance spectra (DRS) for pure TiO_2 nanotubes and the ZnO/TiO_2 heterojunction films. Two sets of samples were tested: (i) amorphous titania nanotubes and their corresponding ZnO/TiO_2 heterojunctions (part A), and (ii) crystalline titania nanotubes and their corresponding ZnO/TiO_2 heterojunctions (part B). As shown in part A, the pure amorphous titania nanotubes showed a continuous wide absorption band with the absorption edge located at about 380 nm, corresponding to a bandgap of 3.26 eV. Upon sputtering the ZnO layers, the absorption band edge is red-shifted towards higher wavelength, curves a-c. Note that the amount of red shift increases with increasing the amount of ZnO (sputtering time) reaching 400 nm (3.1 eV) for the heterojunction sputtered at 53 min. The heterojunctions fabricated by sputtering ZnO on previously annealed titania nanotube films (Part B) showed almost the same absorption trend as those in Part A. However, the absorption band edges are slightly shifted to higher wavelengths reaching 405 nm (3.06 eV) for the 53 min-heterojunction sample (part B, curve c). This slight shift in the absorption band edge can, on one hand, be related to the enhanced crystallinity, in a good agreement with the literature [10]. On the other hand, the slight change in the bandgap can be explained based on the band-edge positions in ZnO relative to TiO_2. The fact that the potentials of the CB and VB of ZnO are slightly more negative than those of TiO_2 may facilitate heterojunction sputtered at 53 min [11].

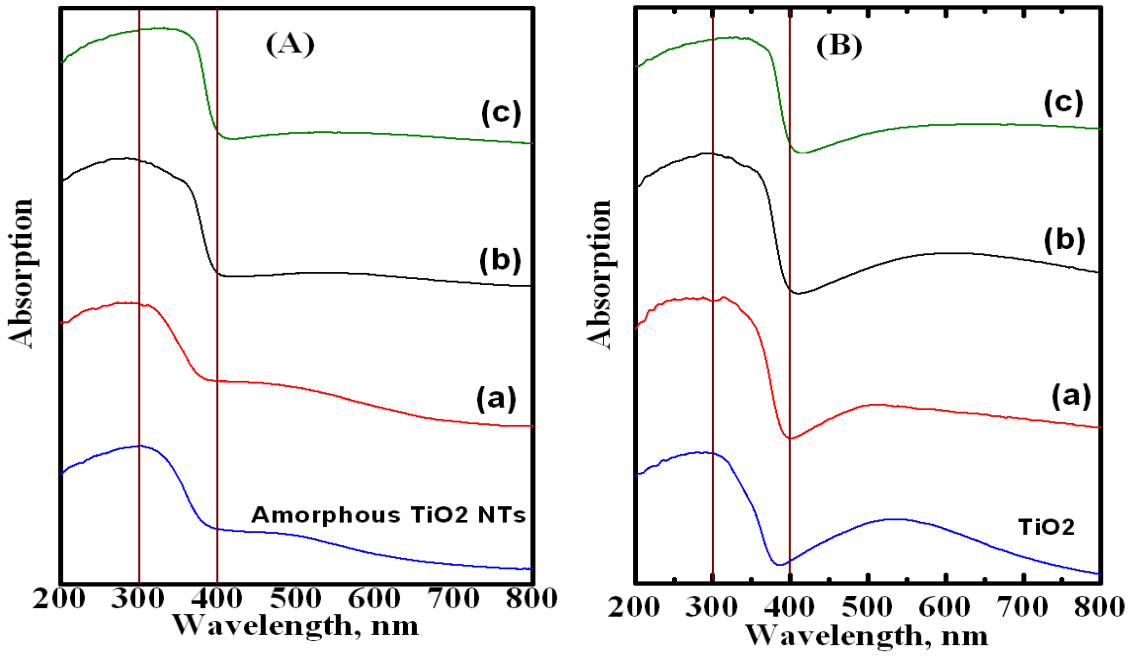

Figure 5-9: The absorption spectra of (A) the as anodized TiO_2 nanotubes and the corresponding ZnO/TiO_2 heterojunction formed via sputtering ZnO for (a) 18, (b) 35 and (c) 53 min, respectively on annealed TiO_2 nanotube films and (B) the annealed TiO_2 nanotubes and the corresponding ZnO/TiO_2 heterojunction formed via sputtering ZnO for (a) 18, (b) 35 and (c) 53 min, respectively on annealed TiO_2 nanotube films.

The photoelectrochemical activity test for water photoelectrolysis using the grown ZnO/TiO_2 heterojunctions was carried out in a 0.5 M Na_2SO_4 electrolyte solution using a typical three-electrode electrochemical cell, **Figure 5-10**. Dark scans showed almost negligible current densities in the range of 0.1 µA/ cm^2. Upon illumination (UV light 320 – 400 nm, 100 mW/cm^2) (**Figure 5-10A**), a significant increase in the photocurrent with increasing the applied potential was observed for pure TiO_2 nanotube electrode as well as the ZnO/TiO_2 heterojunction electrodes. This enhancement in photocurrent may be related to the good electron transport and network forming ability of the electrodes. The maximum obtained photocurrent density of pure TiO_2 was 10.3 mA cm^{-2}. The

photocurrent enhanced drastically upon grafting the ZnO layers on the titania nanotubes, reaching 13.7 mA cm^{-2} for the heterojunction electrode sputtered for 53 min. Comparing the photocurrents to the dark currents may indicate that the photocurrents under illumination conditions are mainly generated only by absorbed photons without a dark-current contribution. We note that the maximum photocurrent obtained for the 18 min-heterojunction electrode (9.7 mA cm^{-2}) is lower than that for pure titania nanotubes. However, the onset potential (-0.67 $V_{Ag/AgCl}$) is more negative than that of pure titania (-0.62 $V_{Ag/AgCl}$). The open-circuit voltage represents the contribution of light toward the minimum voltage needed for the water splitting potential [12]. In fact, the onset potentials for all junction electrodes are more negative than that of pure titania nanotube electrode. Therefore, it seems that the heterojunction photoanodes require less voltage for water oxidation than the pure TiO_2 photoanode, indicating more favorable photoelectrochemical activity [12].

To assess the efficiency of the fabricated electrodes, the light-energy-to-chemical- energy conversion (photoconversion) efficiency (η) was calculated as follows:

η% = [(total power output – electrical power output)/light power input] x 100

$$= j_p[(E^0_{rev} - |E_{appl}|) / I_0] \times 100 \quad (1)$$

Where j_p is the photocurrent density (mA/cm^2), $j_p E^0_{rev}$ the total power output, $j_p|E_{appl}|$the electrical power input and I_0 is the power density of incident light (mW/cm^2). E^0_{rev} is the standard reversible potential, and the applied potential $E_{appl} = E_{meas} - E_{aoc}$, where E_{meas} is the electrode potential of the working electrode at which photocurrent was measured

under illumination and E_{aoc} is the electrode potential of the same working electrode at open circuit conditions under the same illumination and in the same electrolyte.

Figure 5-10B shows the obtained photoconversion efficiency of pure titania nanotubes as well as the fabricated ZnO/TiO_2 heterojunctions. The photoconversion efficiencies for all tested heterojunctions are greater than that obtained for pure titania nanotubes electrode, confirming the higher photoactivity of the heterojunctions, which is in agreement with the more negative onset potentials. The 53 min-heterojunction electrode showed almost 80% increase in the photoconversion efficiency (7.3%) compared to that of pure titania nanotubes electrode (4.1%). Also, the photoconversion efficiency increases with increasing the amount of sputtered ZnO, in agreement with the photocurrent (Figure 5-10A) and DRS (Figure 5-9) results.

The enhanced photoactivity of the heterojunction electrodes can be understood based on the band positions in the two-oxide system, Schematic 5-1. Upon band gap excitation, the photogenerated electrons in the ZnO CB can be injected into the TiO_2 CB, which in turn will change the bottom of the CB. Simultaneously, the photogenerated holes can transfer from the VB of TiO_2 to that of ZnO. Thus, the interfacial electron transfer from ZnO to TiO_2 can effectively separate the electrons and holes, inhibiting the recombination of electron-hole pairs and accordingly increase the lifetime of the charge carriers. This reduction in recombination can be considered the main reason behind the enhanced photoactivity of the heterojunction electrodes.

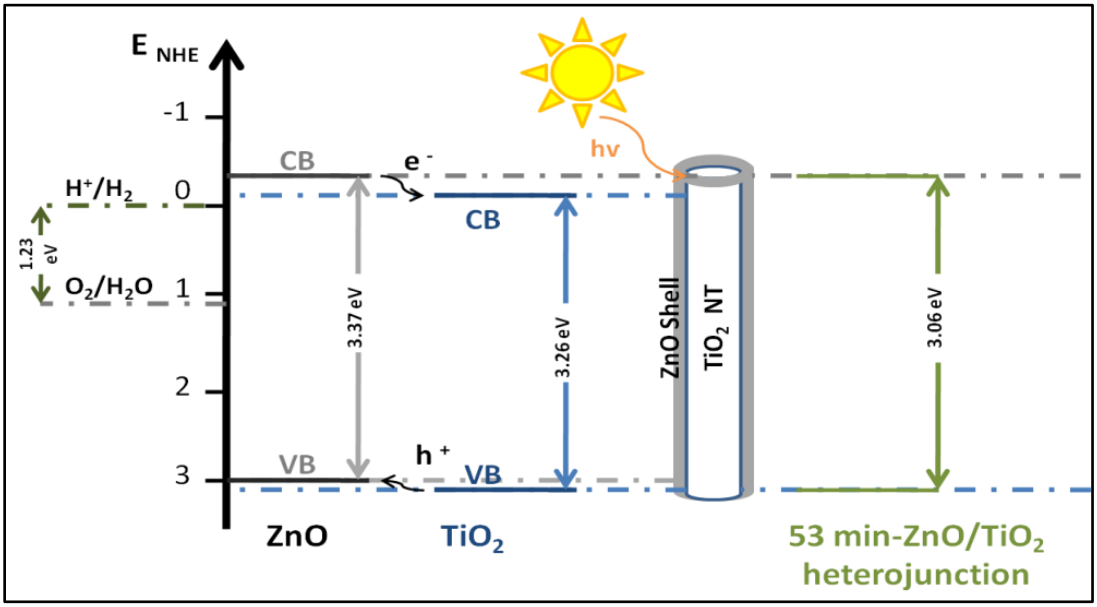

Schematic 5-1: Illustration of the band gap energy and the charge separation of the ZnO/TiO_2 heterojunctions under illumination.

Figure 5-10C shows the incident photon conversion efficiency (IPCE) of the pure TiO_2 and the 53-min ZnO/TiO_2photoelectrodes as a function of the irradiation wavelength in 0.5 M Na_2SO_4solutions under a constant applied bias of 0.6V. The IPCE was calculated using Eq. 2, where λ is the wavelength of incident light, i_{ph} is the photocurrent density under illumination at λ and *Io* is the incident light intensity at λ.

$$IPCE\% = \frac{(1240\ eV.nm)\times(i_{ph}\,mA.cm^{-2})}{(\lambda nm)\times(I_o\,mW.cm^{-2})}\times 100 \qquad (2)$$

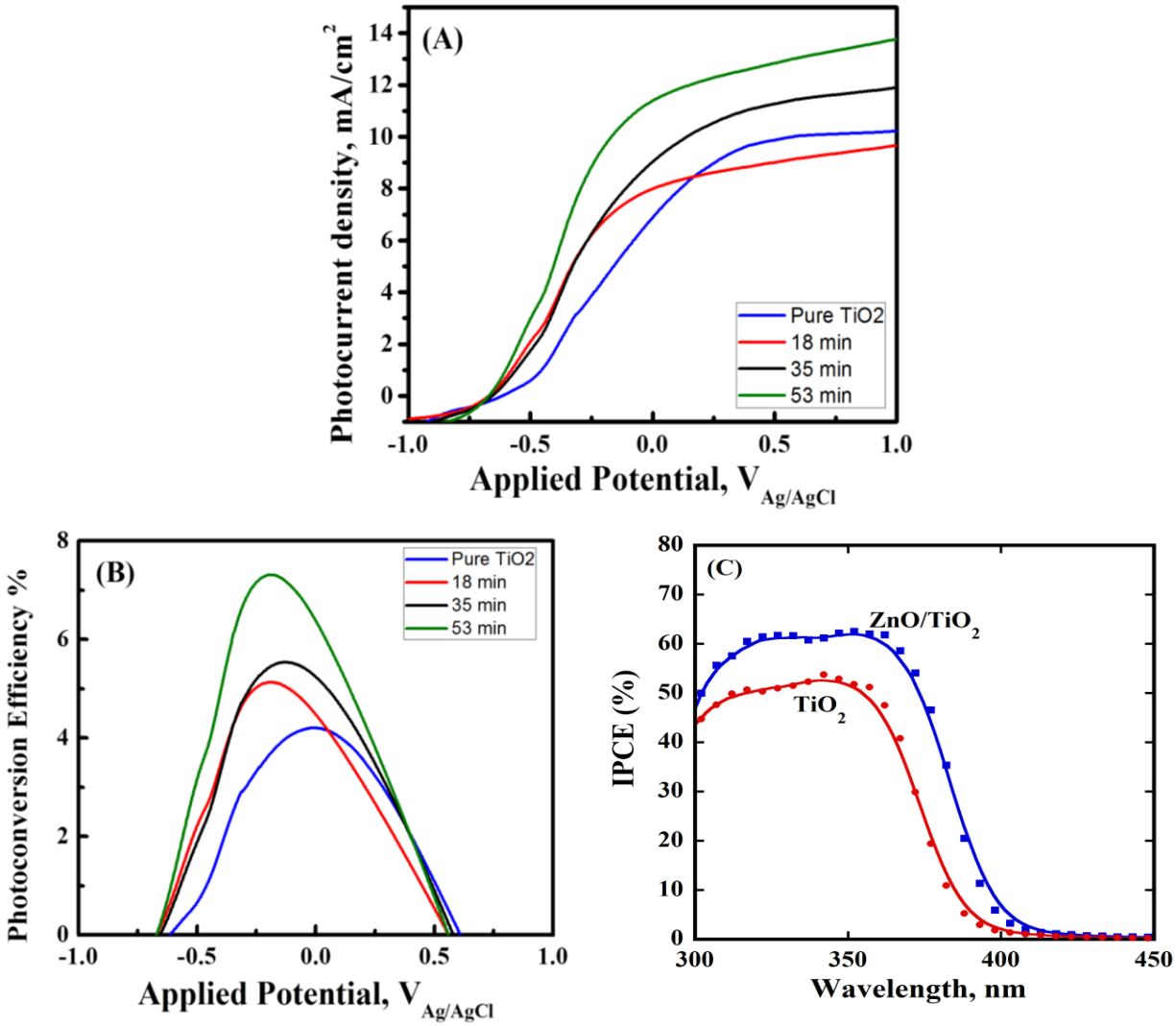

Figure 5-10: (A) Photocurrent density vs. potential in 0.5 M Na_2SO_4 solution under UV (320 – 400 nm, 100 mW/cm^2) illumination for the pure titania nanotubes and the ZnO/TiO_2 heterojunction electrodes, (B) the corresponding photoconversion efficiency and (c) The IPCE of pure TiO_2 nanotubes and the 53-min ZnO/TiO_2 electrodes under a constant bias of 0.6 V.

Note that an IPCE of 50% is obtained for pure TiO_2 nanotubes, which increases to about 60% upon the use of the ZnO/TiO_2 heterojunction electrode. This increase in IPCE can be related to the reduction in the charge carriers recombination rate upon the use of the heterojunction electrodes, in agreement with the photocurrent measurements and

Scheme 2. In this regard, the applied bias also assists the separation of the photogenerated electron-hole pairs, thereby enhancing the IPCE. Note also that the obtained IPCE results are in agreement with the absorption data shown in figure 5-9, where the combination of ZnO and TiO_2 resulted in a red shift in the absorption edge as compared to pure titania photoanode.

Using density functional theory (DFT) calculations for the ZnO/TiO_2 interface, Conesa [13] showed that the energy difference promotes charge separation. Consequently, the interface, with its lower band width, can absorb lower energy photons leading to some photocatalytic activity in the visible light region, in an agreement with the experimental absorption results. The results indicate that the vertically oriented ZnO/TiO_2 heterojunctions can offer a great potential as a material architecture for water oxidation due to their suitable band edges positions and high IPCE.

In summary, the fabrication of efficient ZnO/TiO_2 nanotubes heterojunctions composed of anodically fabricated TiO_2 nanotubes inner core and thermally evaporated ZnO outer shell was demonstrated. The morphology, crystallinity and optical properties of the hybrid electrodes were found to depend on the sputtering time of ZnO and consequently its thickness. The light adsorption was red-shifted with increasing the ZnO shell thickness reaching 405 nm for the 53 min-sputtered electrode. Used as a photoanode to photoelectrochemically split water, the TiO_2/ZnO heterojunction sputtered for 53 min showed almost 80% increase in the photoconversion efficiency (7.3%) compared to that of pure TiO_2 NTs (4.1%) under UV illumination (320-400 nm, 100 mW/cm^2, 0.5 M Na_2SO_4). This was confirmed via the IPCE measurements, which showed an enhancement in the charge carriers' collection efficiency in the heterojunction electrodes

compared to pure titania nanotube films. The enhanced photocatalytic activity of the heterojunctions can be related to the large exposed surface area to the surrounding electrolyte and the formation of hybrid core-shell structure that greatly promotes efficient separation of photogenerated electron−hole charge carriers. The ZnO/TiO_2 interface plays a key role to promote charge separation and shifting the absorption slightly to the visible light. The concept is also proven by investigating the oxide films of Zn – 13.6 wt. % Ti and Ti – 11.29 wt. % Zn. The higher percentage of Zn in the oxide film showed higher photocurrent. Therefore, the investigation of other stoichiometries and morphology of Zn-Ti oxide system can offer more enhancements.

References

1. Allam, N. K.; El-Sayed, M. A. Photoelectrochemical Water Oxidation Characteristics of Anodically Fabricated TiO_2 Nanotube Arrays: Structural and Optical Properties. *J. Phys. Chem. C* **2010**, *114*, 12024–12029.
2. Allam, N. K.; Grimes, C. A. Room Temperature One-Step Polyol Synthesis of Anatase TiO_2 Nanotube Arrays: Photoelectrochemical Properties. *Langmuir* **2009**, 25, 7234–7240.
3. Allam N. K.; Grimes, C. A. Effect of Rapid Infrared Annealing on the Photoelectrochemical Properties of Anodically Fabricated TiO_2 Nanotube Arrays. *J. Phys. Chem. C* **2009**, *113*, 7996–7999.
4. Wonga, Y. –H.; Li, Q. Study of the crystallinity of ZnO in the Zn/ZnO nanocable heterostructures. *J. Mater. Chem.***2004**, 14, 1413–1418.
5. Briggs, D.; Gran, T. J. *Surface Analysis by Auger and X-ray Photoelectron Spectroscopy*; IM Publications: Chichester, UK, **2003**.
6. Jing, L.; Xin, B.; Yuan, F.; Xue, L.; Wang, B.; Fu, H. Effects of Surface Oxygen Vacancies on Photophysical and Photochemical Processes of Zn-Doped TiO_2 Nanoparticles and Their Relationships. *J. Phys. Chem. B* **2006**, 110, 17860–17865.
7. Yu, Y.; Yu, J. C.; Yu, J. G.; Kwok, Y. C.; Che, Y. K.; Zhao, J. C.; Ding, L.; Ge, W. K.; Wong, P. K. Enhancement of photocatalytic activity of mesoporous TiO_2 by using carbon nanotubes. *Appl. Catal. A* **2005**, 289, 186–196.

8. Hu, H.; Song, W.; Ruan, W.; Wang, Y.; Wang, X.; Xu, W.; Zhao, B. Fabrication of one-dimensional ZnO/4-Mpy/Ag assemblies and their spectroscopic studies. *Journal of Colloid and Interface Science* **2010**, 344, 251–255.
9. Wang, Y. X.; Li, X. Y.; Lu, G.; Quan, X.; Chen, G. H. Highly Oriented 1-D ZnO Nanorod Arrays on Zinc Foil: Direct Growth from Substrate, Optical Properties and Photocatalytic Activities. *J. Phys. Chem. C* **2008**, 112, 7332–7336.
10. Allam, N. K.; Shankar, K.; Grimes, C. A. A General Method for the Anodic Formation of Crystalline Metal Oxide Nanotube Arrays without the Use of Thermal Annealing. *Advanced Materials***2008**, 20, 3942–3946.
11. Serpone, N.; Maruthamuthu, P.; Pichat, P.; Pelizzetti, E.; Hidaka, H. Exploiting the interparticle electron transfer process in the photocatalysed oxidation of phenol, 2-chlorophenol and pentachlorophenol: chemical evidence for electron and hole transfer between coupled semiconductors. *J. Photochem. Photobiol. A* **1995**, 85, 247–255.
12. Grimes, C. A.; Varghese, O. K.; Ranjan, S. *Light, Water, Hydrogen: The Solar Generation of Hydrogen by Water Photoelectrolysis*, Springer: New York, **2008**.
13. Conesa, J. C. Modeling with Hybrid Density Functional Theory the Electronic Band Alignment at the Zinc Oxide–Anatase Interface. *J. Phys. Chem. C* **2012**, 116,18884−18890.

Chapter 6

Niobium Oxide – Based Photoanodes for Solar Fuel Production

As discussed in chapter 3, niobium oxide materials are widely used in many optical and electronic applications, however their investigation as photoanodes for solar-water splitting is limited. This can be related to the complexity of the niobium – oxygen system and the difficult formation of well-organized structures by facile methods like anodization. In this chapter, the results for the anodization of different structures of niobium oxides are presented. A study for *in-situ* crystallization of niobium oxide microcones during anodization is also discussed. Finally, the development of niobium oxynitride by nitrogen doping is explained along with its effect on the optical properties of the material.

6.1 Fabrication of self – organized niobium oxide

Four morphologies of niobium oxides were successfully obtained by anodization: nanopores, nanorods, nanochannels, and microcones with nanowire – like structure. The different structures were formed by varying the anodization parameters (electrolyte solution, voltage, and duration). **Table 6-1** shows the conditions that enabled the fabrication of nanoporous, nanochannel and nanorod structures. **Figures 6-1, 6-2 and 6-3** show the morphology of the Nb_2O_5 nanoporous, nanochannels and nanorods, respectively as investigated by FESEM. **Figure 6-4** shows the AFM images of the nanoporous and nanorod structures.

Table 6-1: Anodization conditions for niobium oxide nanoporous and nanochannels structures

Structure	Composition of Electrolyte	Voltage - Time	Average Dimensions
Nanoporous	0.4 M NH_4F + 2ml H_2O + 48 ml Glycerol	20 V – 2 hrs	Pore diameter ≈16 ± 3.5 nm
Nanochannels	0.5 ml HF + 1.25 ml H_2O + 23.25 ml H_2SO_4	20 V – 10 min	Channel length ≈ 114 ± 36 nm
Nanorods	0.75 ml HF + 3 ml H_2O + 21.25 ml H_2SO_4	30 V – 3 min	Rod length ≈ 114 ± 36 nm

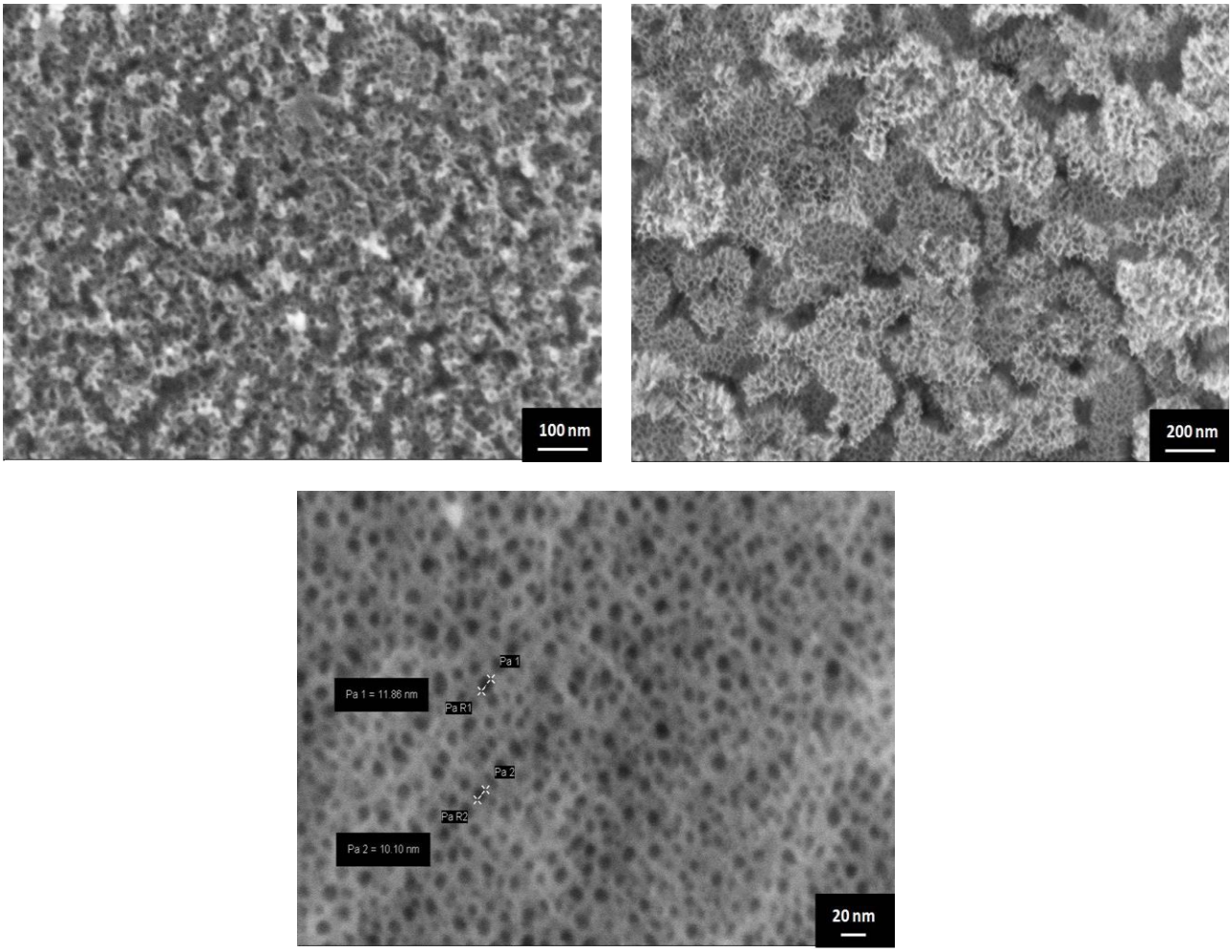

Figure 6-1: Different magnifications FESEM images of the nanoporous Nb_2O_5 fabricated by anodization in glycerol electrolyte containing 0.4 M NH_4F at 20 V for 2 hours.

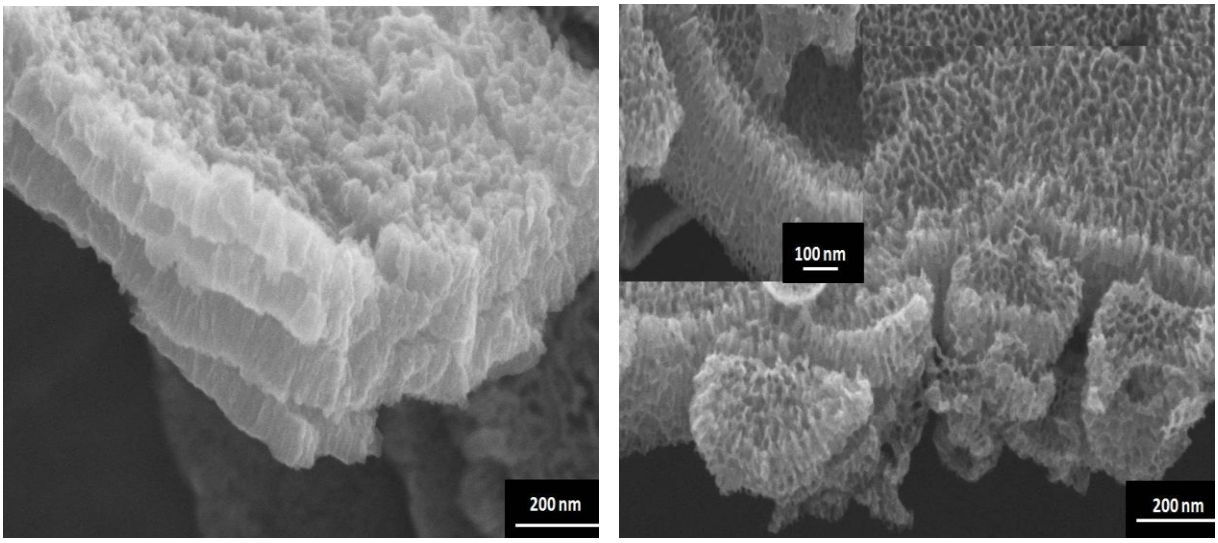

Figure 6-2: FESEM images of the Nb_2O_5 nanchannels fabricated by anodization in H_2SO_4 electrolyte containing 0.5 ml HF and 1.25 ml H_2O at 20 V for 10 min.

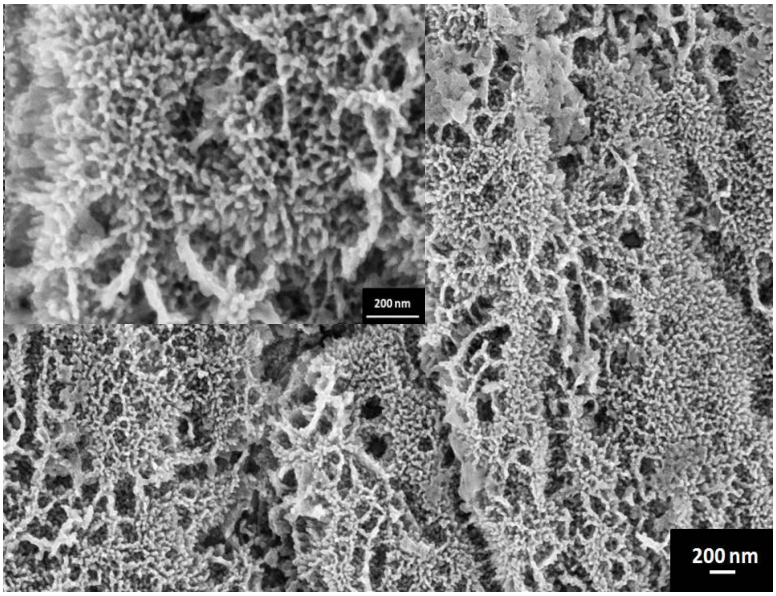

Figure 6-3: FESEM images of the Nb_2O_5 nanorods fabricated by anodization in H_2SO_4 electrolyte containing 0.75 ml HF and 3 ml H_2O at 30 V for 3 min.

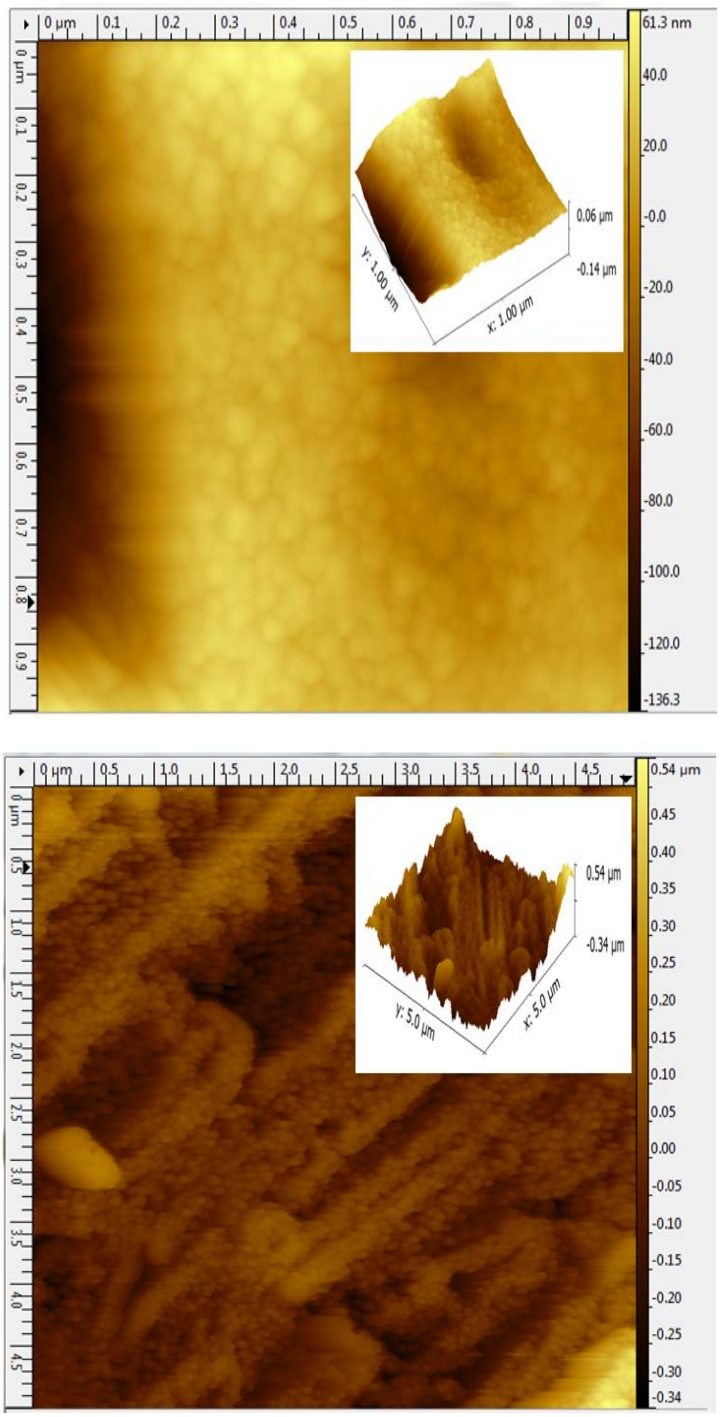

Figure 6-4: AFM images of nanoporous (upper) and nanorods of Nb_2O_5 (below).

In agreement with literature, it was observed that the nanoporous and nanochannel structures are formed in small thickness that can be easily removed [1]. Therefore, anodization conditions were modified in an attempt to fabricate more homogeneous and stable structures. It was started with the same anodization procedure reported by Jeong et *al.* for the fabrication of Nb_2O_5 microcones [2]. **Table 6-2** summarizes the fabrication conditions.

Table 6-2: Electrolyte compositions for niobium oxide cones.

Parameter	Electrolyte Composition	Voltage - Time	Morphology
Aqueous Electrolyte	1M NaF + 1wt. % HF in DI. Water	40 V – 50 min	Average Height 16 ± 3 µm.
	1 M NaF in DI. Water	40 V – 50 min	Average Height 20 ± 4 µm
	1 M NH_4F in DI. Water	40 V – 50 min	Average Height 12 ± 2 µm
Organic Electrolyte	1 M NaF + 1wt. % HF + DI. Water + 5 vol. % Glycerol	40 V – 50 min	
	1 M NaF + 1wt. % HF + DI. Water + 5 vol. % Ethylene Glycol	40 V – 50 min	Microcones with broken tips
	1 M NaF + 1wt. % HF + DI. Water + 5 vol. % Formamide	40 V – 50 min	Separated Microcones
pH	1M NaF + 1wt. % HF in DI. Water + NH_4OH to adjust the pH at 5	40 V – 50 min	Height11 ± 1 µm
	1M NaF + 1wt. % HF in DI. Water + H_3PO_4 to adjust the pH at 3	40 V – 50 min	Height 15 ± 2 µm
Voltage	1M NaF + 1wt. % HF in DI. Water	20 V – 50 min	Height 11 ± 2 µm
	1M NaF + 1wt. % HF in DI. Water	60 V – 50 min	Height 7 ± 1 µm.

Figures 6-5 shows the morphology of the microcones fabricated in different aqueous electrolytes. Since the first work done on the fabrication of Nb_2O_5 microcones with nano-sized tips, HF is used as the electrolyte or at least as one of the constituents. Due to the hazards of HF and the strict precautions required during its use, 1 M NaF and 1 M NH_4F aqueous electrolytes free from HF were used to grow microcones. Also, the effect of the addition of organic solvents is shown in **Figure 6-6**. The addition of 5 volume % of formamide to the electrolyte (1 M NaF and 1 ml HF) leads to the formation of separated microcones, opposite to the effect of adding 5 volume % of glycerol. The addition of 5 volume % of ethylene glycol, on the other hand, resulted in the breakdown of the tip of the microcones.

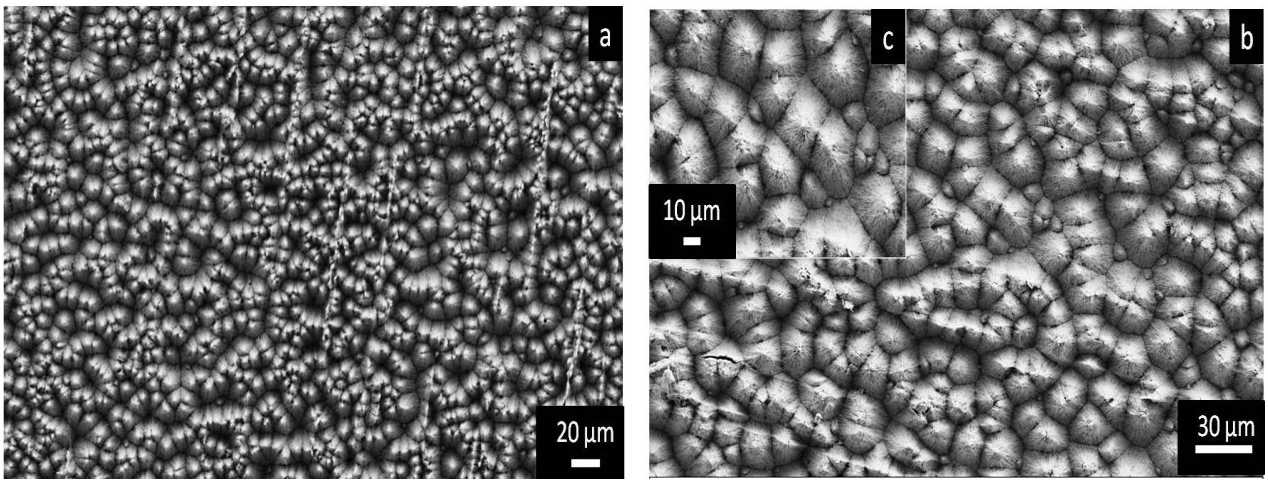

Figure 6-5: FESEM top-view images of as-anodized micro cones of Nb_2O_5 at 40 V for 50 min in HF free electrolyte containing (a) 1M NH_4F and (b) 1M NaF and (c) is a higher magnification of (b).

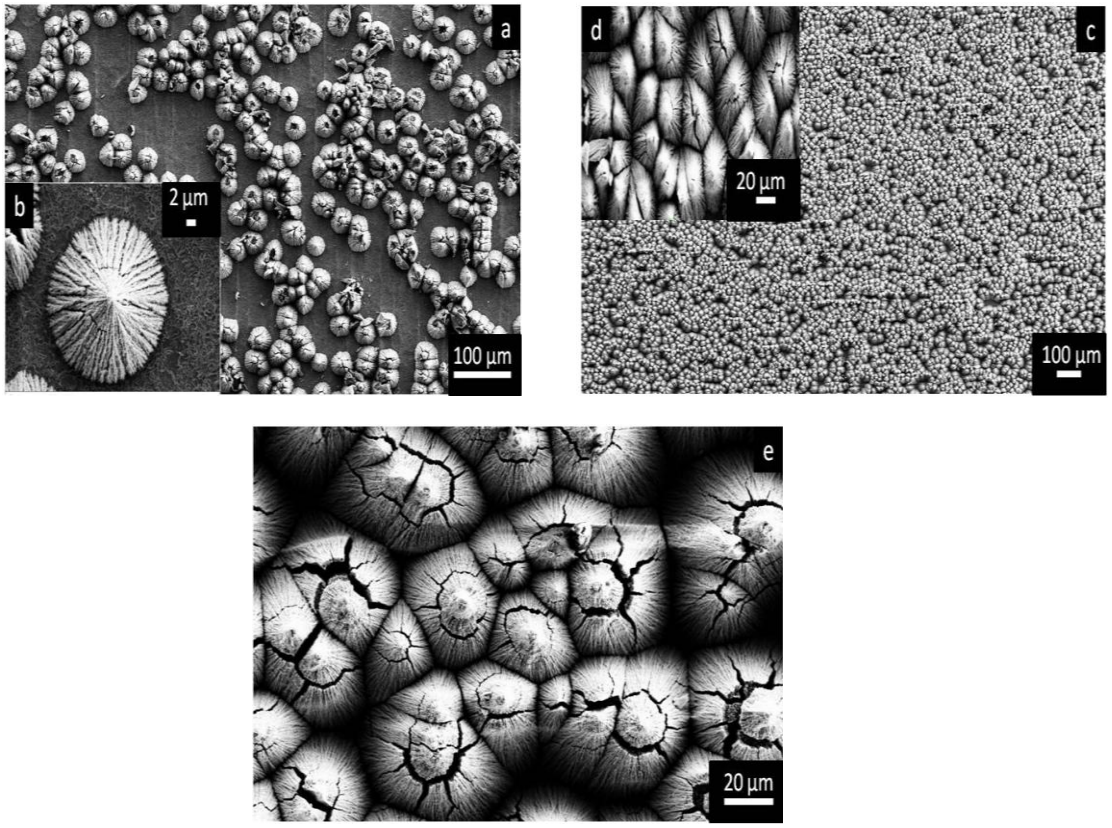

Figure 6-6: FESEM top-view images of as-anodized micro cones of Nb_2O_5 at 40 V for 50 min in 1 M NaF + 1 wt. % HF with 5 vol. % (a) formamide, (b) higher magnification (c) glycerol and (d) ethylene glycol.

The pH of the electrolyte is known to be effective in determining the structure resulting from the anodization process. The pH of the 1 M NaF and 1 ml HF electrolyte is 4. Thus, the pH of the electrolyte was made more acidic (pH 3) by adding drops of H_3PO_4. On the other hand, the electrolyte was made more alkaline (pH 5) by adding drops of NH_4OH. **Figure 6-7** shows the morphology of the microcones obtained at pH 3 and 5.

The applied voltage was another parameter to be studied in the fabrication of Nb_2O_5 microcones. **Figure 6-8 (a)** shows microcones fabricated in 1 M NaF and 1 ml HF

electrolyte for 50 min at 20 V. **Figure 6-8 (b)** shows smaller microcones formed in similar electrolyte at 60 V. It was noticed that the high voltage cause the oxide layer to be less adhered to the metal foil.

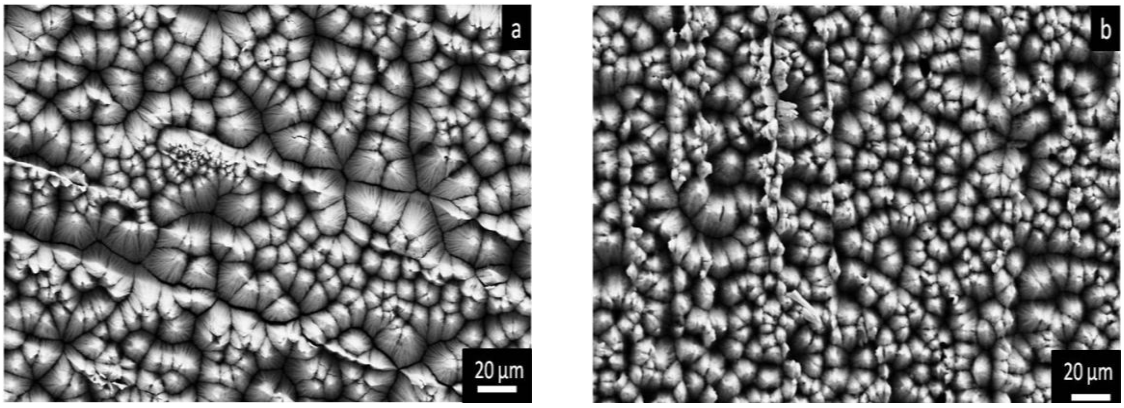

Figure 6-7: FESEM top-view images of as-anodized micro cones of Nb_2O_5 at 40 V in 1 M NaF + 1 wt. % HF electrolyte at (a) pH 3 by the addition of H_3PO_4 and (b) pH 5 by the addition of NH_4OH.

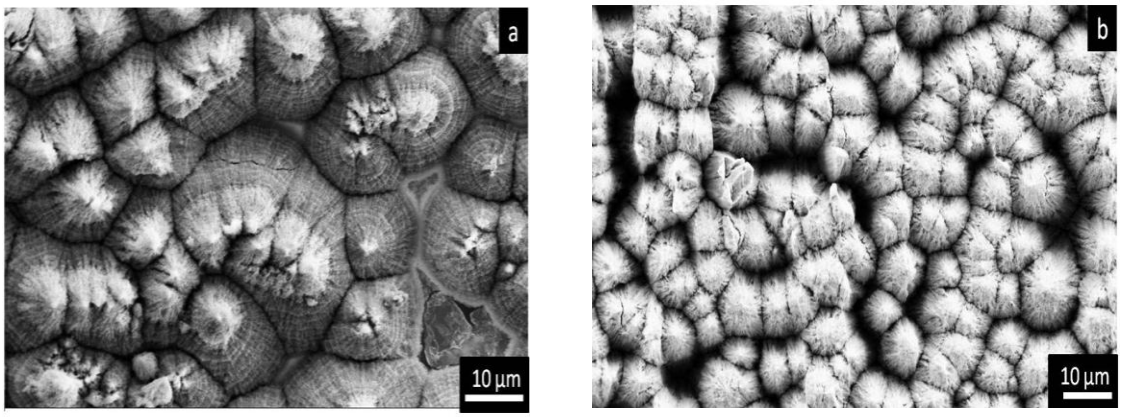

Figure 6-8: FESEM top-view images of as-anodized micro cones of Nb_2O_5 in 1 M NaF + 1 wt. % HF electrolyte (pH 4) at voltages (a) 20 V and (b) 60 V.

As it was stated previously, the nanoporous and nanochannels oxide layers are thinner and less stable than the microcones. **Figure 6-9** shows the UV-Vis diffuse reflectance spectra (DRS) of the Nb_2O_5 nanoporous, nanochannels and microcones

samples. **Figure 6-9 (a)** and **(b)** show that the maximum absorption for the nanoporous and nanochannels samples occurs at wavelength ≈ 363 nm. **Figure 6-9 (c)** shows that the microcones have higher absorption at wavelength ≈ 450 nm. There was also variation in the absorption spectra between the microcones samples fabricated in different aqueous electrolytes as shown in **Figure 6-10**. Microcones fabricated in NH_4F aqueous electrolyte shows lower absorption (360 nm). Microcones fabricated in NaF aqueous electrolyte and in NaF with HF electrolyte absorbed till 480 and 450 nm, respectively.

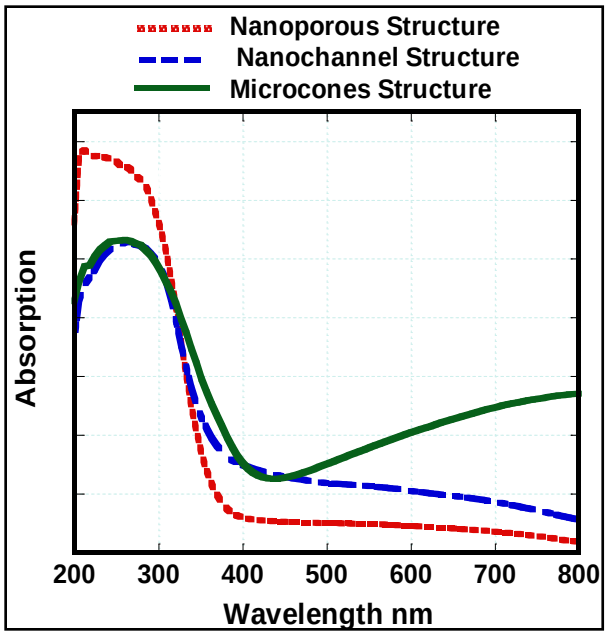

Figure 6-9: The absorption spectra of Nb_2O_5 anodized in the form of nanoporous, nanochannels and microcones fabricated in 1 M NaF + 1 wt. % HF at 40 V for 50 min.

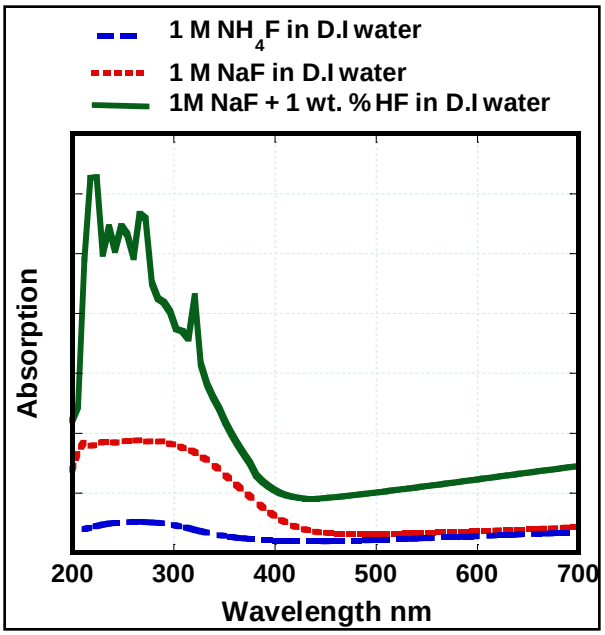

Figure 6-10: The absorption spectra of Nb_2O_5 micro cones anodized at 40 V for 50 min in 1 M NaF, 1 M NH_4F and 1 M NaF + 1 wt. % HF aqueous electrolytes.

This variation in the absorption with the morphology can be understood in agreement with the several reports that explain the effect of the architecture on light management in attempt to achieve full absorption and trapping [3, 4]. **Figure 6-11** shows four different architectures [3].

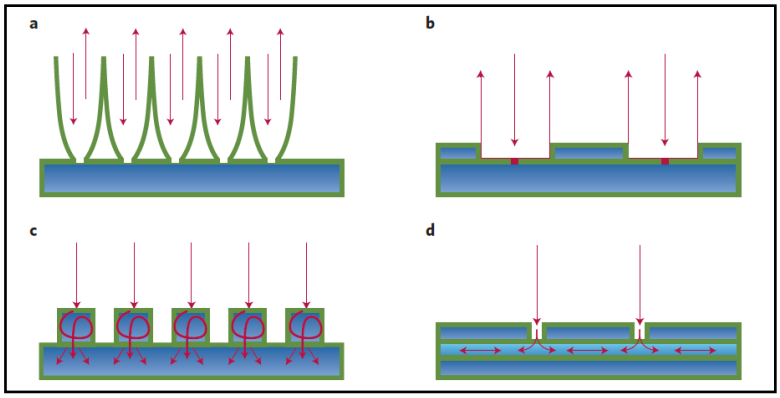

Figure 6-11: Light-management architectures for reaching ultrahigh efficiency. **a** Three-dimensional parabolic light reflector, **b** Planar metamaterial light-director structures, **c** Mie-scattering surface nanostructure for light trapping and **d** Metal–dielectric– metal waveguide or semiconductor–dielectric–semiconductor slot waveguide [3].

Moreover, Kosten *et al.* conducted a comparison between two GaAs solar cell geometries, conventional planar geometry and a light trapping geometry (cone structure) as shown in **Figure 6-12**. The limiting emission angle in a light trapping geometry allows for much thinner cells and for significantly higher overall efficiencies. However, the planar structure provides larger angular distribution of light that increases the entropy of photons leading to efficiency loss.

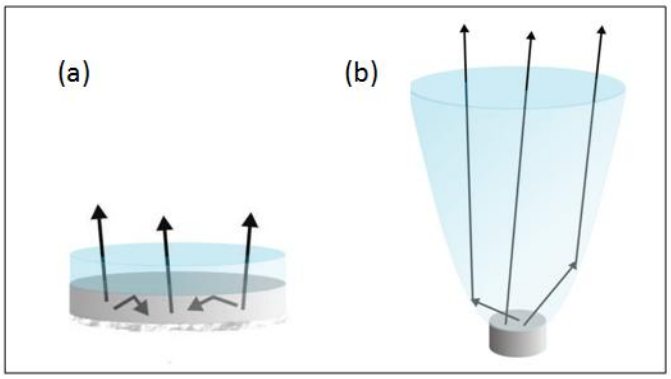

Figure 6-12: Light management in (a) planar geometry and (b) light trapping geometry [5].

In an attempt to understand the mechanism of fabrication of Nb_2O_5 microcones in 1 M NaF and 1 wt. % HF electrolyte at 40 V, the tests were repeated at different durations starting from 1 min till 20 min as shown on **Table 6-3.**

Table 6-3: The growth of niobium oxide cones with the time in 1 M NaF and 1 wt. % HF electrolyte at 40 V.

Time (minutes)	Morphology
1	nanopores
3	nanopores
5	nanopores
7	nanorods
10	microcones
20	microcones

Figure 6-13 shows the FESEM images of the obtained structures. First, pores are formed and continue to increase as shown in **Figure 6-13 (c)**. Then, nanostructures as nanorods are formed as shown in **Figure 6-13 (d)**. The nanochannels are connected to form multilayer of microcones as shown in **Figure 6-13 (e)**. Well-developed microcones can be seen after 20 min of anodization as shown in **Figure 6-13 (f)**. Higher magnification of microcones formed for 20 min shows that they are composed of well-developed nanowires as shown in **Figure 6-14**. The tip was found to have an average size of 800 nm. Using the same electrolyte (1 M NaF + 1 wt. % HF) but from different chemical company, the anodization at 40 V for 10 min resulted in the formation of a different structure, branched nanowire – like structure as shown in **Figure 6-15**.

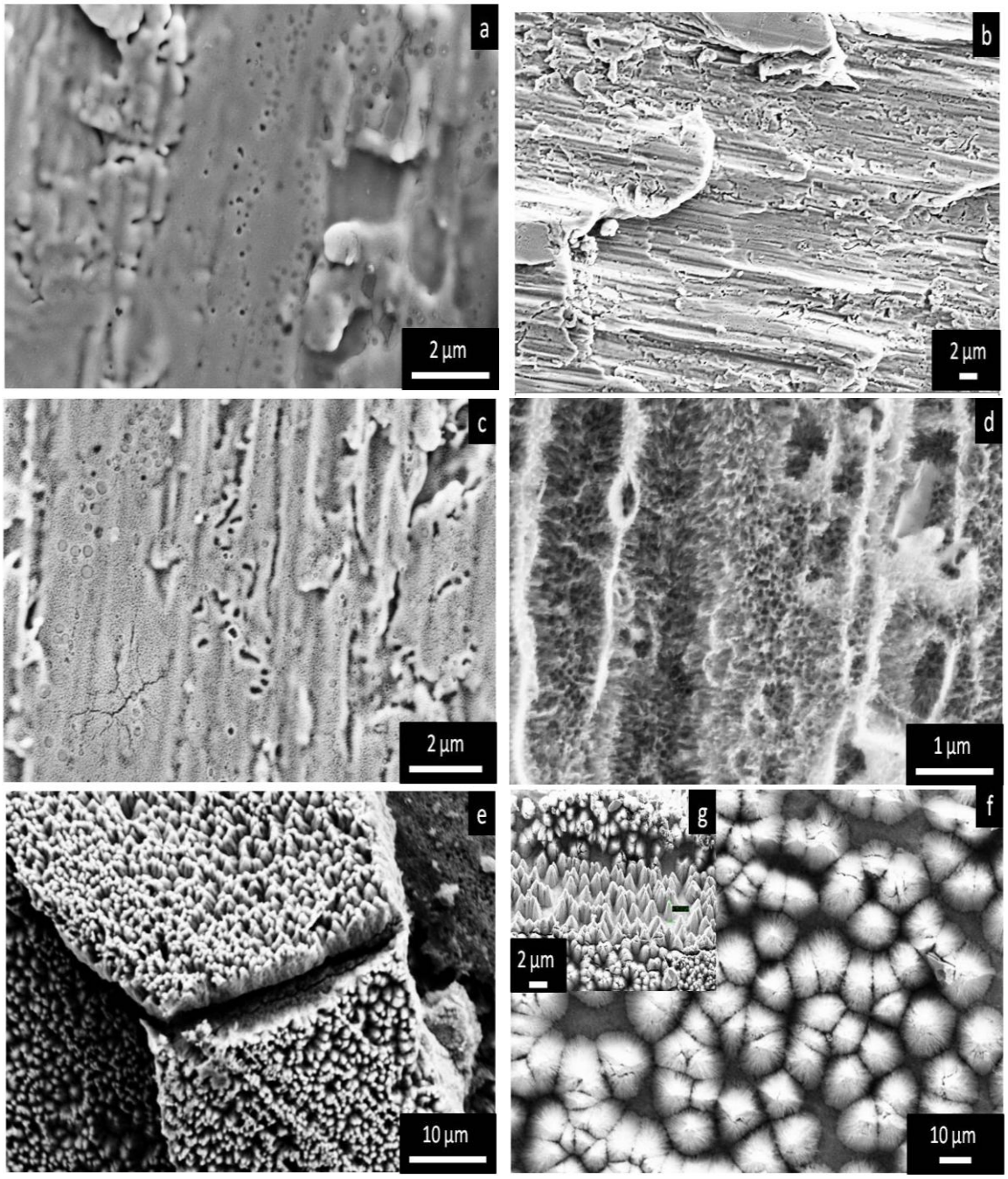

Figure 6-13: FESEM top-view images of as-anodized micro cones of Nb_2O_5 at 40 V in 1 ml HF and 1 ml NaF electrolyte for different durations (a) 1 min (b) 3 min (c) 5 min (d) 7 min (e) 10 min (f) 20 min and (g) higher magnification.

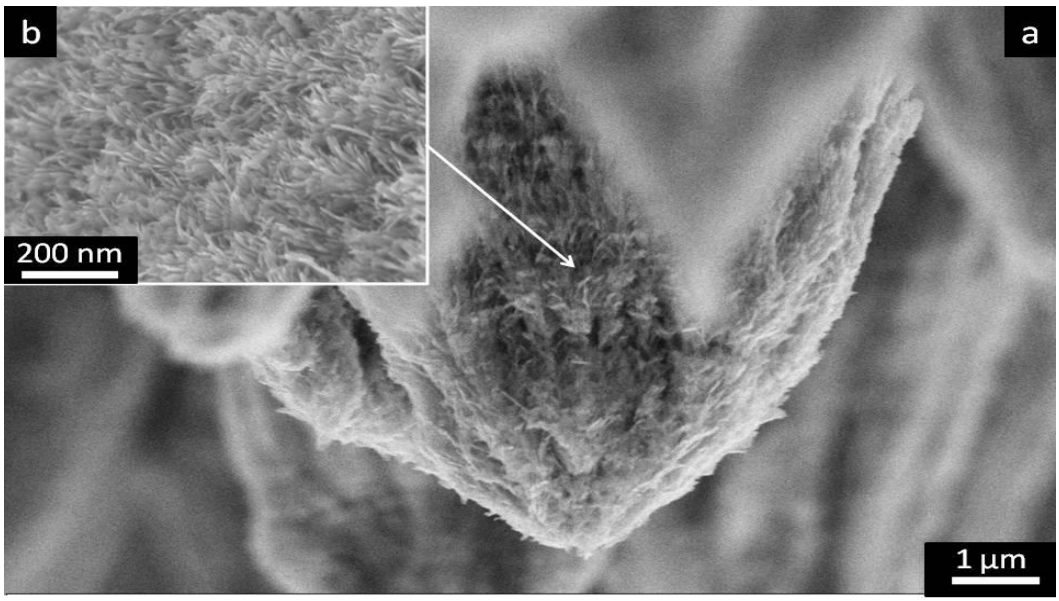

Figure 6-14: FESEM images of as-anodized micro cones of Nb_2O_5 at 40 V in 1 ml HF and 1 ml NaF electrolyte for (a) 20 min and (b) is a higher magnification of the microcones showing nanowires structure.

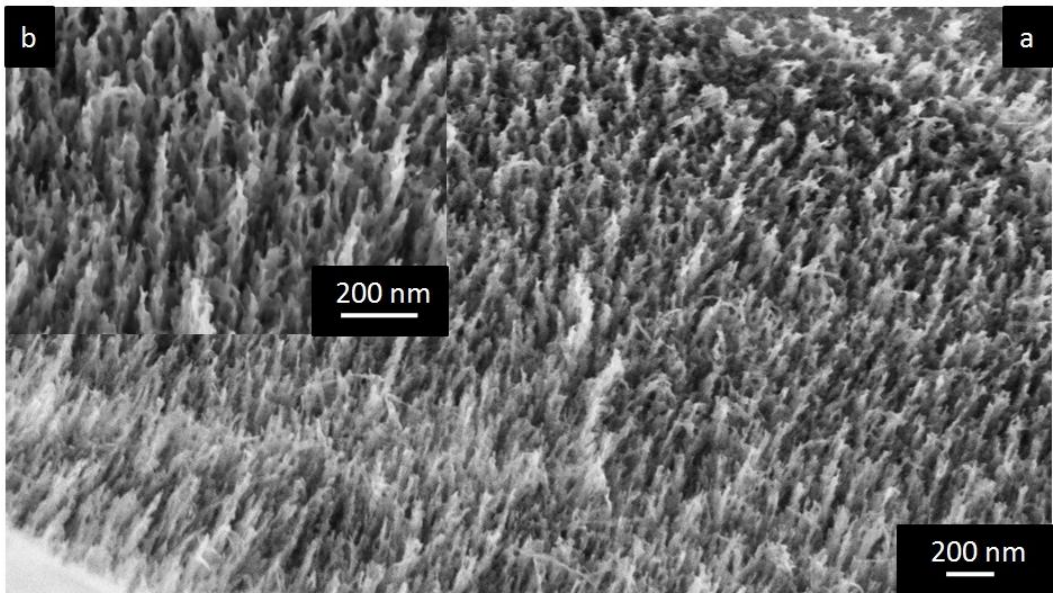

Figure 6-15: FESEM images of as-anodized Nb_2O_5 40 V in 1 ml HF and 1 ml NaF electrolyte for 10 min using local chemicals in the form of branched nanowires.

The samples anodized for different durations were annealed and then analyzed for their structure using XRD. **Figure 6-16** shows that all the samples are crystalline with the characteristic peaks of orthorhombic Nb_2O_5. Note that the intensity of the characteristic (100) peak increases as the duration of anodization increases.

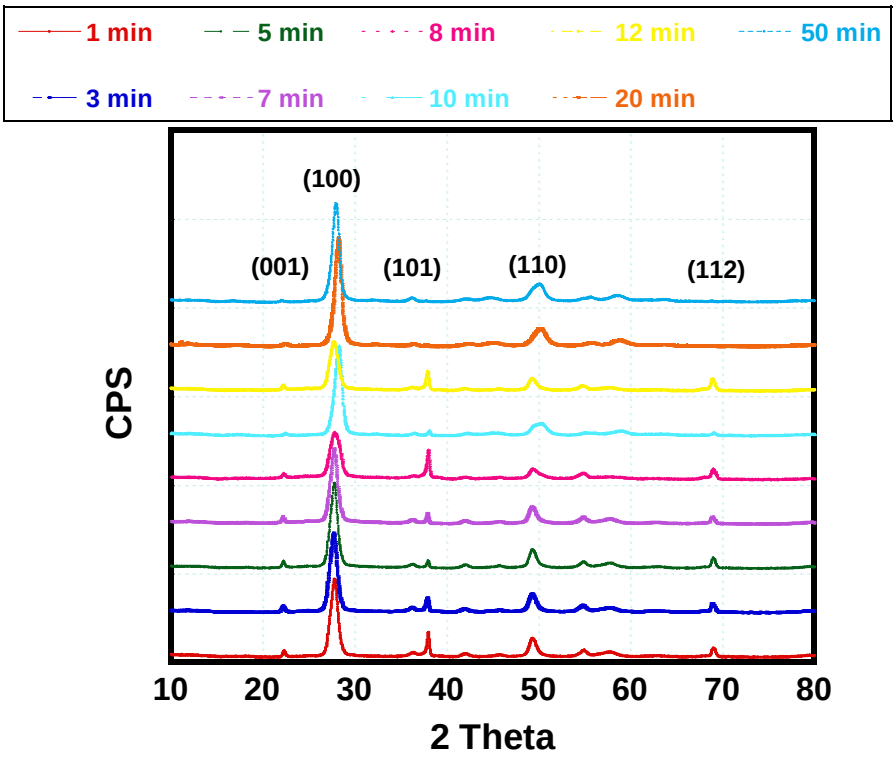

Figure 6-16: GAXRD diffraction patterns of Nb_2O_5 microcones anodized in 1 ml HF and 1 M NaF aqueous electrolyte at 40 V for 1, 3, 5, 7, 8, 10, 12, 20, and 50 minutes.

In summary, this section showed the possibility of forming various morphologies of Nb_2O_5 by controlling the anodization parameters. The different morphologies play a role in defining the properties of the material as was shown for the optical properties. In addition, the photoelectrochemical properties are dependent on the morphology as shown in **Figure 6-17**. The photocurrent-time measurements for niobium oxide in the form of

thin film, microcones and nanowires were done in aqueous solution of 1 M Na_2SO_4 under constant applied bias of 0.5 V and radiation of AM 1.5. The lowest photocurrent was produced from the thin film sample (0.5 µA/ cm^2) compared to that produced from microcones (10 µA/ cm^2) and nanowires (15 µA/ cm^2). The nanowires have nano size dimensions which facilitate the charge transfer compared to the micro size of the microcones structure.

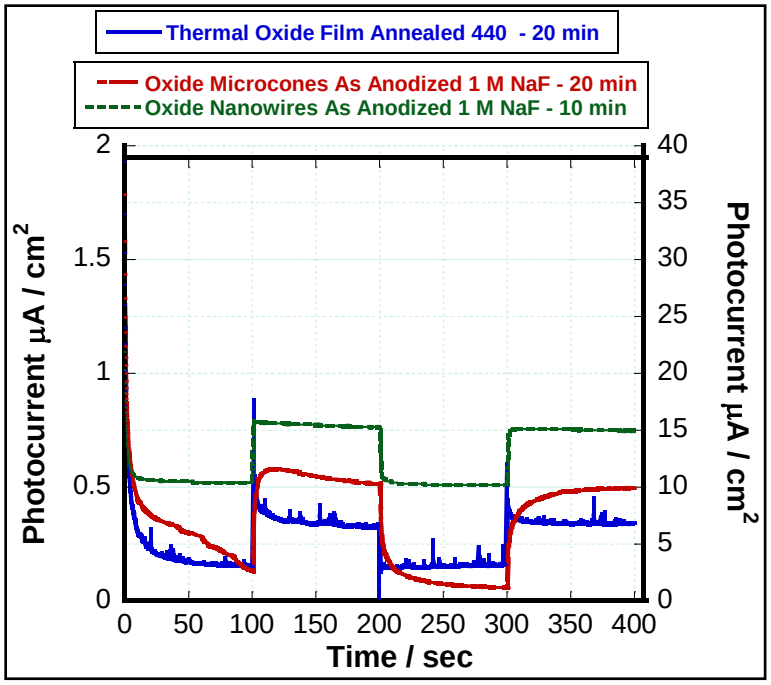

Figure 6-17: Photocurrent-time curve of Nb_2O_5 samples with different morphologies (thin film formed by thermal annealing, microcones and nanowires formed by anodization). All samples are measured in aqueous electrolyte (1 M Na_2SO_4 – pH 3) at external bias 0.5 V.

The crystallinity of the formed Nb_2O_5 microcones formed at different durations starting from 1 min till 50 min directed the attention for studying the crystalline structure of the as-anodized structures formed in NaF and HF electrolytes as discussed in the following section.

6.2 Room Temperature Crystallization of Niobium Oxide Microcones

The microcone structure is considered to be homogeneous and well-developed. In addition, its high roughness and nano-sized tip promote its use in many applications such as sensors and dye-sensitized solar cells. As discussed in chapter 3 and section 6.1, anodization has been used to produce ordered nanostructures and microstructures of niobium oxides. However, the resulted structures are usually amorphous with an elevated temperature heat-treatment required to induce crystallinity, limiting their applications in many fields. For example, in photocatalysis, annealing at temperatures sufficient to induce crystallinity usually leads to the formation of a dense barrier layer, separating the structured oxide array film from the underlying metal substrate. This barrier layer introduces a significant series resistance that hinders transport of the photogenerated charge carriers, in turn reducing the overall efficiency of the system. The need for high-temperature crystallization also limits the use of the material with temperature-sensitive materials, such as polymers, for applications such as flexible solar cells. Therefore, in-*situ* low-temperature synthesis routes, where a high-temperature annealing step for crystallization is not required, are needed to obtain the full benefit of those unique materials. Also, crystallization during the anodization process saves energy and time required for the annealing step. In addition, the low temperature crystallization preserves the morphology of the formed structure. In this regard, in-situ crystallization during anodization has been studied for TiO_2 nanotubes fabricated in highly viscous organic electrolytes [6]. Other studies showed the effect of electrolyte temperature on the formation of crystalline Nb_2O_5 microcones [7-9]. Herein, we demonstrate the possibility

of *in-situ* crystallization of niobium oxide microcones during their fabrication by controlling the electrolyte composition.

Figure 6-18 (a-f) shows FESEM images of as-anodized niobium oxide microcones fabricated in aqueous electrolytes containing 1 ml HF with different concentrations of NaF. **Figure 6-18 (g)** shows the annealed microcones in air at 440 ^{o}C for 20 min. Anodization in HF electrolytes resulted in the formation of scattered microstructures **(Figure 6-18 a)**. Upon the addition of NaF, well developed and closely-packed microcones have been obtained; **Figure 6-18 c, f**.

Figure 6-19 shows the XRD patterns obtained for the niobium oxide microcones fabricated in different electrolytes. In the absence of NaF **(Figure 6-19 a)**, Nb metal peaks with high intensity were only observed indicating the amorphous nature of the formed oxide layer. Upon the addition of 0.1 M NaF **(Figure 6-19 b)**, a small peak appeared at 27^{o}, which can be related to the (100) plane for orthorhombic Nb_2O_5 [10]. The intensity of the (100) peak continues to increase with increasing the NaF concentration, **Figure 6-19 c-f**, with the emergence of another peak at 49.9^{o} that is corresponding to the (001) orthorhombic Nb_2O_5 [10]. For comparison, the XRD pattern of an annealed niobium oxide microcones sample (20 min at 440 ^{o}C in air) is also shown, **Figure 6-19 g**. Note that the same diffraction pattern was observed for both annealed and as-anodized samples, confirming the successful fabrication of crystalline microcones directly from the anodization bath. However, the intensity of the (100) peaks was slightly different for different conditions as shown in **Figure 6-20**.

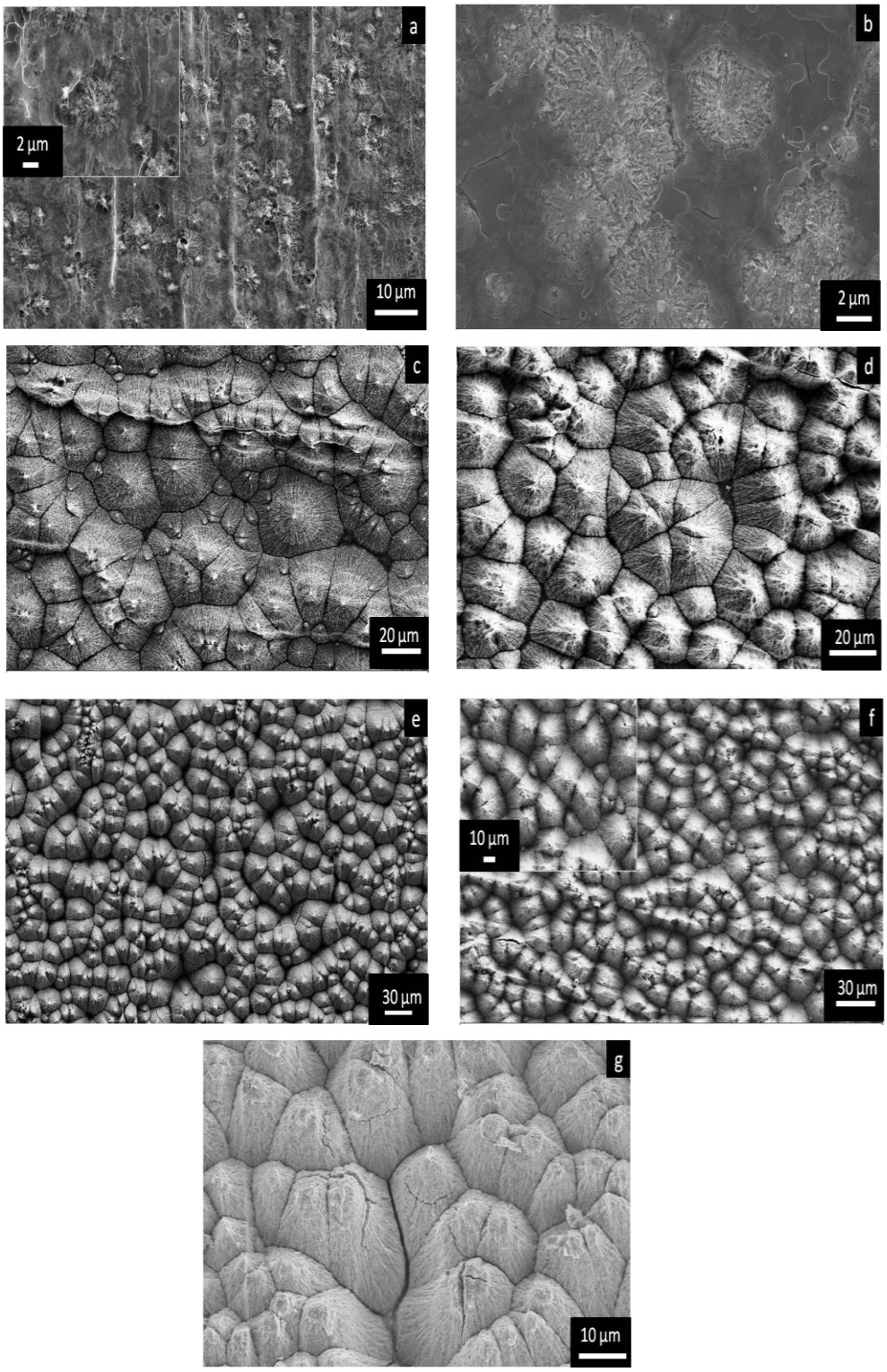

Figure 6-18: FESEM of the niobium oxide microcones obtained via anodization of Nb at 40 V for 50 min in aqueous electrolytes containing (a) 1 ml HF, (b) 0.2 M NaF + 1 ml HF, (c) 1 M NaF + 1ml HF, and (d) 1 M NaF + 1ml HF and then annealed in air at 440 ^{o}C for 20 minutes.

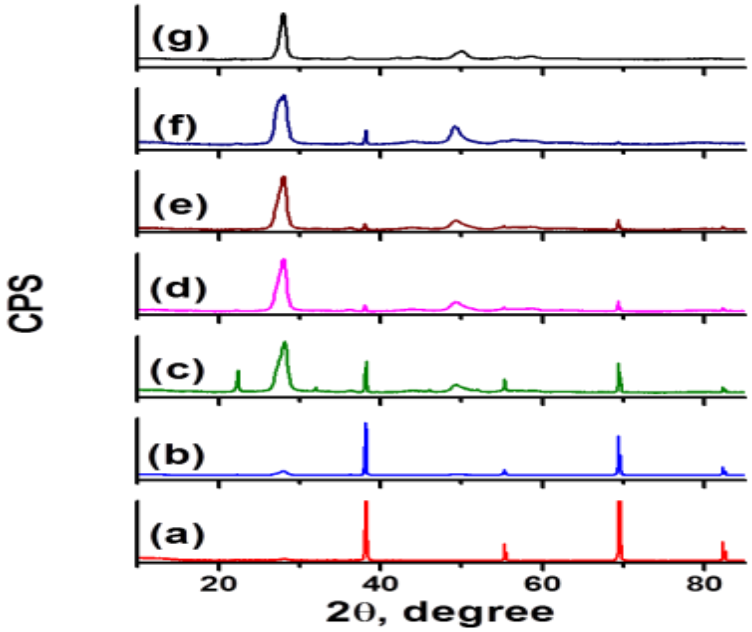

Figure 6-19: XRD patterns of the samples anodized at 40 V for 50 min in aqueous electrolytes containing (a) 1 ml HF, (b) 0.1 M NaF + 1 ml HF, (c) 0.2 M NaF + 1 ml HF, (d) 0.5 M NaF + 1 ml HF, (e) 1 M NaF + 1ml HF, (f) 1 M NaF and (g) 1 M NaF + 1ml HF and then annealed in air at 440 ^{o}C for 20 minutes.

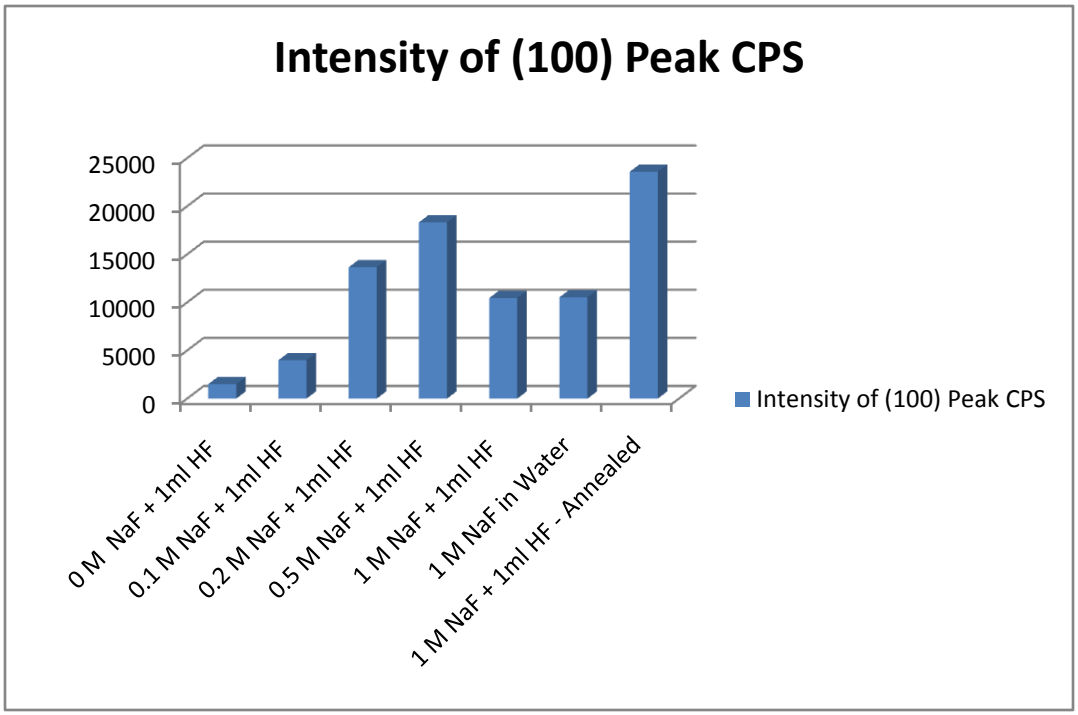

Figure 6-20: Variation of the (100) peak intensity with NaF concentration.

To confirm the results obtained by the XRD, Raman spectroscopy was performed for the same set of samples as shown in **Figure 6-21**. The peak at 690 cm^{-1}obtained for the as-anodized samples **(Figure 6-21 a-f)** is in agreement with that reported for annealed orthorhombic Nb_2O_5 [10], confirming the crystallinity of the as-anodized samples. In addition, the peak at 235 cm^{-1} is another characteristic for Nb_2O_5 [1]. Both peaks at 235 and ~303 cm^{-1} can be related to the bending mode of Nb–O–Nb [11]. For the annealed sample shown in **Figure 6-21 g**, the peak is shifted to 708 cm^{-1} and becomes less broad, which can be attributed to the formation of NbO_2 [11-12].

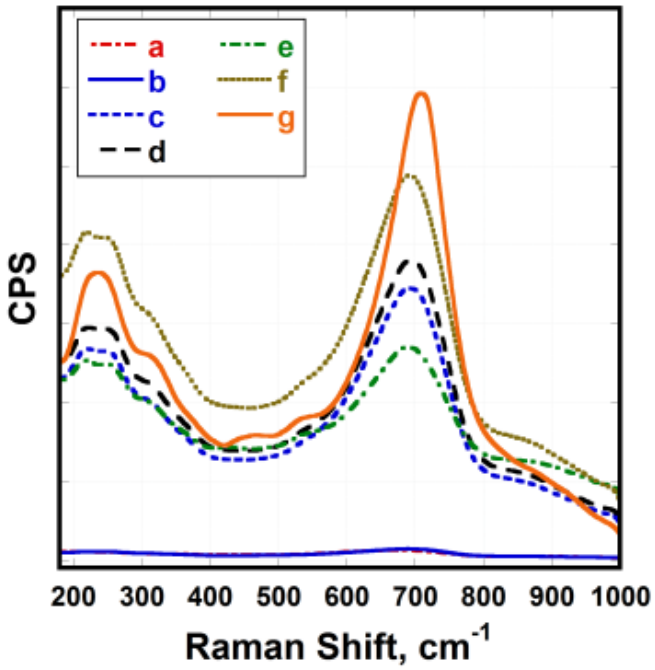

Figure 6-21: Raman Spectra of the samples anodized at 40 V for 50 min in aqueous electrolytes containing (a) 1 ml HF, (b) 0.1 M NaF + 1 ml HF, (c) 0.2 M NaF + 1 ml HF, (d) 0.5 M NaF + 1 ml HF, (e) 1 M NaF + 1ml HF, (f) 1 M NaF and (g) 1 M NaF + 1ml HF and then annealed in air at 440 ºC for 20 minutes.

To further investigate the possibility of the formation of mixed NbO_2 and Nb_2O_5 upon annealing, XPS analysis was performed for the annealed sample. **Figure 6-22 (a)** shows the Nb3d doublet (Nb 3d3/2 at 209.4 eV and Nb 3d5/2 at 206.73 eV) with a spin-orbit splitting of 2.67 eV. According to literature, the Nb 3d5/2 peak for Nb_2O_5 is usually seen at 207.3 eV, while that of NbO_2 usually exists at 206 eV [12]. The O 1s spectra show doublet peaks at 529.64 and 531.14 eV, **Figure 6-22 (b)**. The first peak at 529.64 eV can be assigned to O 1s in Nb_2O_5, while the second peak at 531.14 eV can be assigned to O 1s in NbO_2 [13]. The increase in the oxidation number of Nb from Nb^{+4} to Nb^{+5} reduces the binding energy of O 1s [13]. Thus, the XPS analysis confirms the formation of mixed oxide upon annealing the as-anodized microcones.

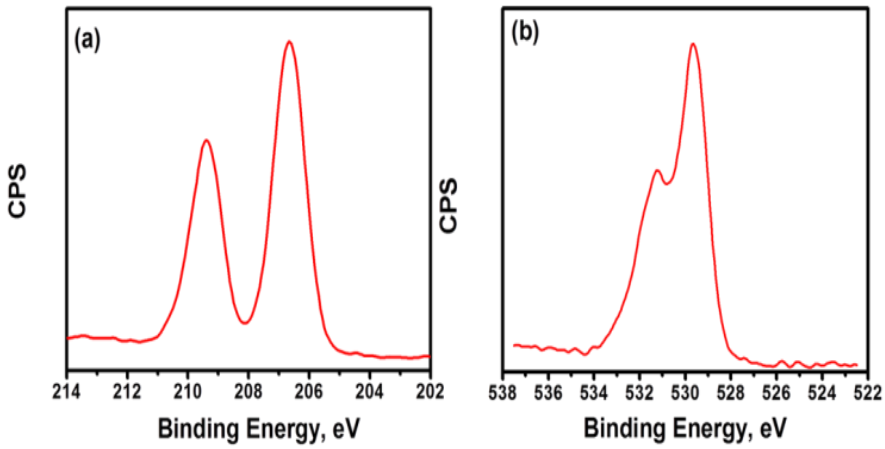

Figure 6-22: XPS spectra of anodized sample at 40 V for 20 min in 1 M NaF + 1ml HF and then annealed in air at 440 ^{o}C for 20 minutes.

As Nb_2O_5 and NbO_2 have different bandgaps, the absorption characteristics were investigated as an evidence for the formation of mixed oxides upon annealing. **Figure 6-23** shows the absorption spectra of as-anodized and annealed samples. The observed red shift in the absorption spectra of the annealed sample as compared to the as-anodized sample can be explained in terms of the mixture of NbO_2 and Nb_2O_5. Orthorhombic Nb_2O_5 is a wide band gap semiconductor (≈ 3.3 - 3.4 eV) while NbO_2 has narrow band gap (0.7 eV) [12]. Thus, the sample containing a mixture from both oxides should have a lower band gap and consequently absorb at higher wavelength than the pure Nb_2O_5.

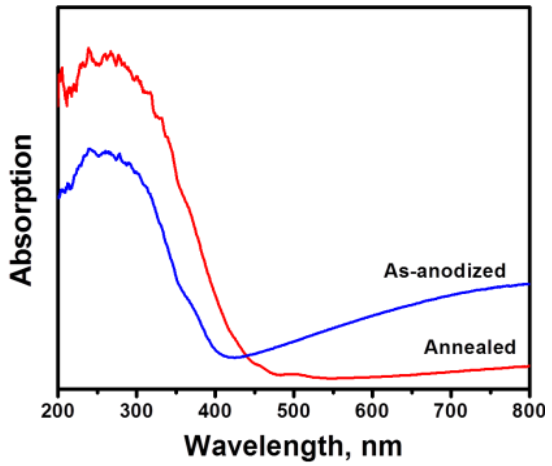

Figure 6-23: Absorption spectra of (a) as-anodized and (b) annealed niobium oxide microcones fabricated at 40 V for 20 min in 1 M NaF + 1ml HF.

The optical spectra of the as-anodized samples in different NaF concentrations are compared in **Figure 6-24**. It was observed that the addition of NaF to the HF-containing electrolytes results in an increase in the electrolyte temperature during anodization, reaching ~ 60 ^{o}C upon the addition of 0.5 M NaF as shown in **Figure 6-25**. From this temperature increase as well as the XRD and Raman data, field-assisted crystallization

during anodization can be proposed as a possible mechanism for the observed crystallinity of the as-anodized microcones [14-17]. The crystalline structure is formed as a result of the electric field, due to the applied voltage, as well as the temperature increase during anodization.

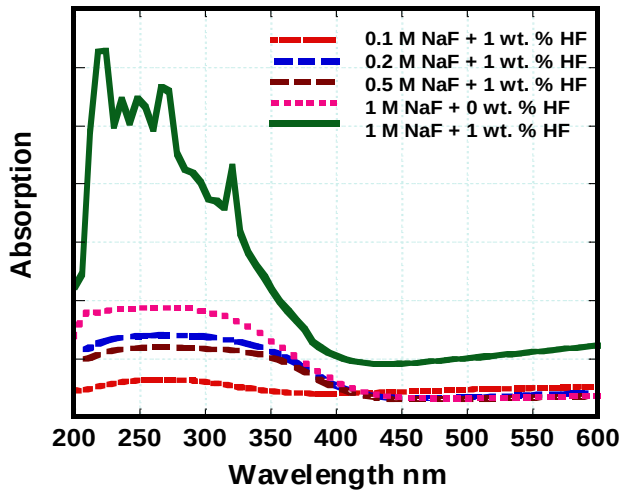

Figure 6-24: Absorption spectra of as anodized samples fabricated at different concentrations of NaF and 1 wt. % HF at 40 V for 50 min.

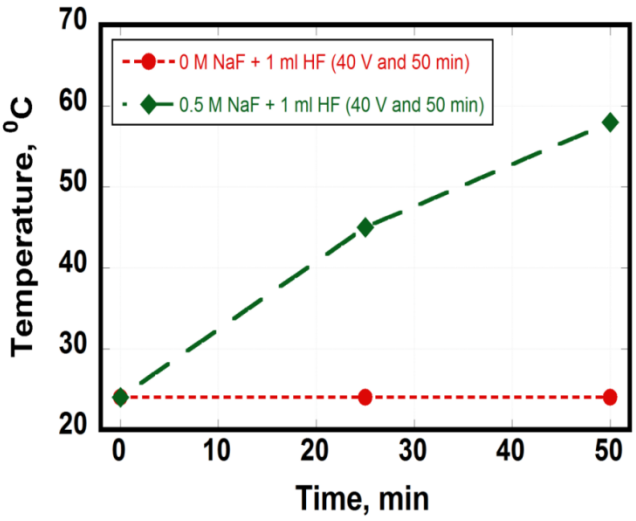

Figure 6-25: Variation of the electrolyte temperature with the NaF concentration.

In terms of applications, having a mixture of stable niobium oxides (Nb_2O_5 and NbO_2) with different bandgaps can be an advantage for optical and electrical applications [18]. While in mechanical and biomedical applications, single phase can be essential to prevent segregation and inhomogeneity in the structure. Back to the thesis' application, the photocurrent of the crystalline as-anodized samples were measured and compared with that of the annealed sample as shown in **Figure 6-26**.The photocurrent of the as-anodized samples increases with the concentration of NaF. However, the annealed sample has much less photocurrent. This can be understood based on the fact that the annealed sample has a mixture of Nb_2O_5 and NbO_2.

In conclusion, the *in-situ* crystallization of Nb_2O_5 (single phase) microcones during anodization of niobium metal is reported in aqueous electrolytes containing different amounts of NaF. The as anodized samples are of high crystallinity such that the peaks and their intensities are comparable to annealed samples at temperature 440 and 240 ^{0}C. The thermal annealing is found to produce a mixture of crystalline phases of niobium oxides (Nb_2O_5 and NbO_2). Both crystalline microcone structures, with single and mixture phases of niobium oxides, are thought to be useful in different applications depending on the structure-properties relationship.

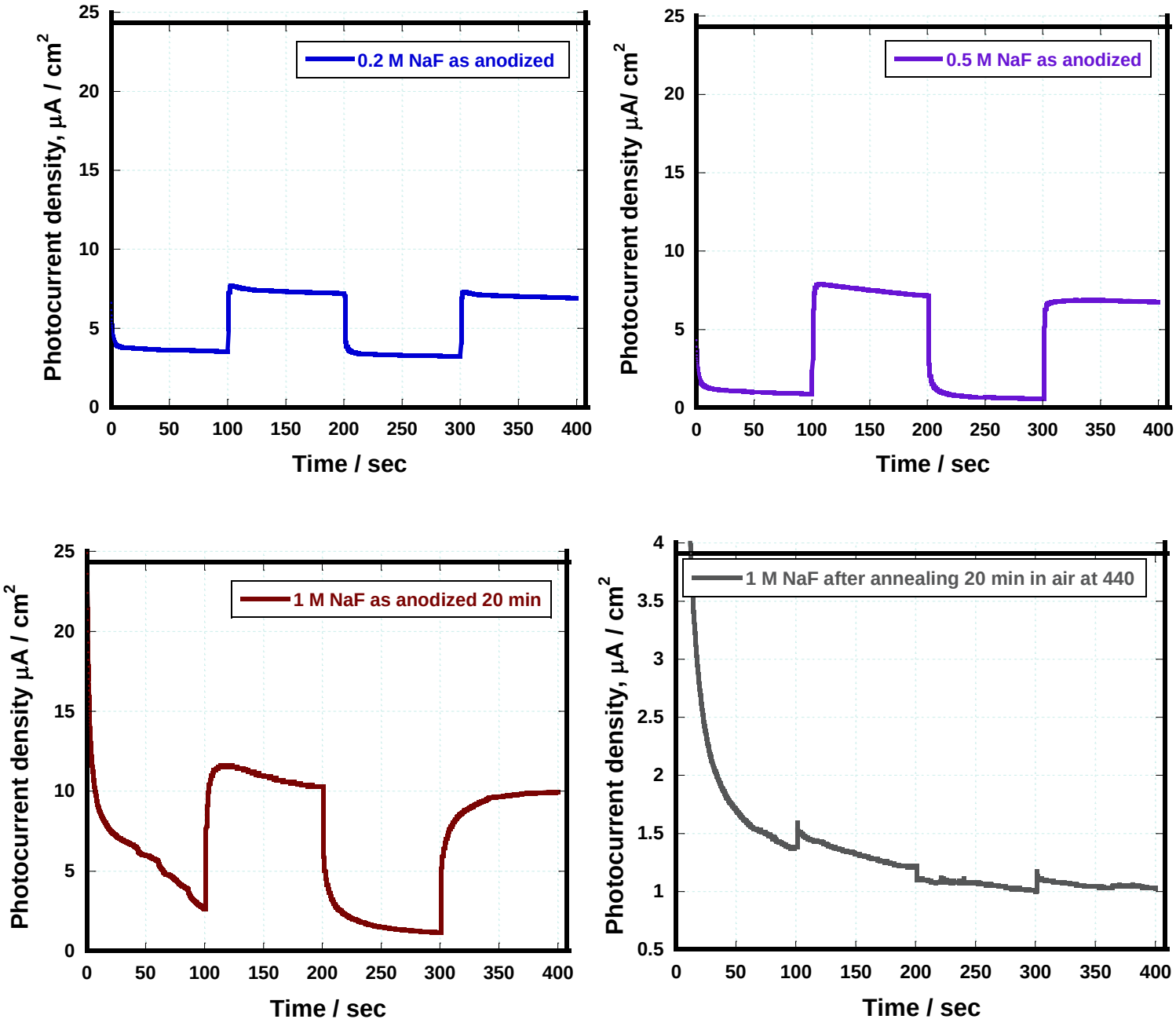

Figure 6-26: Photocurrent-time curve of as Nb_2O_5 microcones anodized samples compared to annealed sample in air at 440 ^{0}C for 20 min. All samples are measured in aqueous electrolyte (1 M Na_2SO_4 – pH 3) at external bias 0.5 V.

6.3 Niobium Oxynitrides with Enhanced Optical Properties

After studying the fabrication and the crystallization of Nb_2O_5 microcones, it was of great interest to study the development of the properties of this well-ordered structure in terms of band gap engineering. The development of niobium oxynitride microcones to make benefit from the decrease of the band gap caused by the N 2p energy is the target of this section. Up till now, the studied niobium oxynitrides in literature are either thin films or powders [19-21]. The new structure is tested as photoanodes for solar water splitting reaction. As stated before in chapter 4, after the formation of Nb_2O_5 microcones by anodization (1M NaF and 1 wt. % HF electrolyte - 40 V – 20 min), they were annealed in ammonia gas to allow their doping with nitrogen. The parameters investigated for the ammonia annealing are shown in **Table 6-4**.

Table 6-4: Conditions of annealing Nb_2O_5 microcones in ammonia.

Sample Code	Ammonia Flow Rate (sccm)	Annealing Duration (min)	Annealing Temperature (^{0}C)
S1	50	20	440
S2	150	180	450
S3	200	20	440
S4	300	20	450
S5	300	60	450
S6	200	300	450
S7	200	420	450

6.3.1 Morphology and Structure Characterization

Figure 6-27 shows the FESEM images of the Nb-O-N microcones prepared at conditions S7 (Table 6-4). It can be observed that the microcones preserved their morphology after the NH_3 annealing compared to as- anodized oxide sample. However, Nb_2O_5 some deformation appears and it is thought to be because of the long duration of annealing.

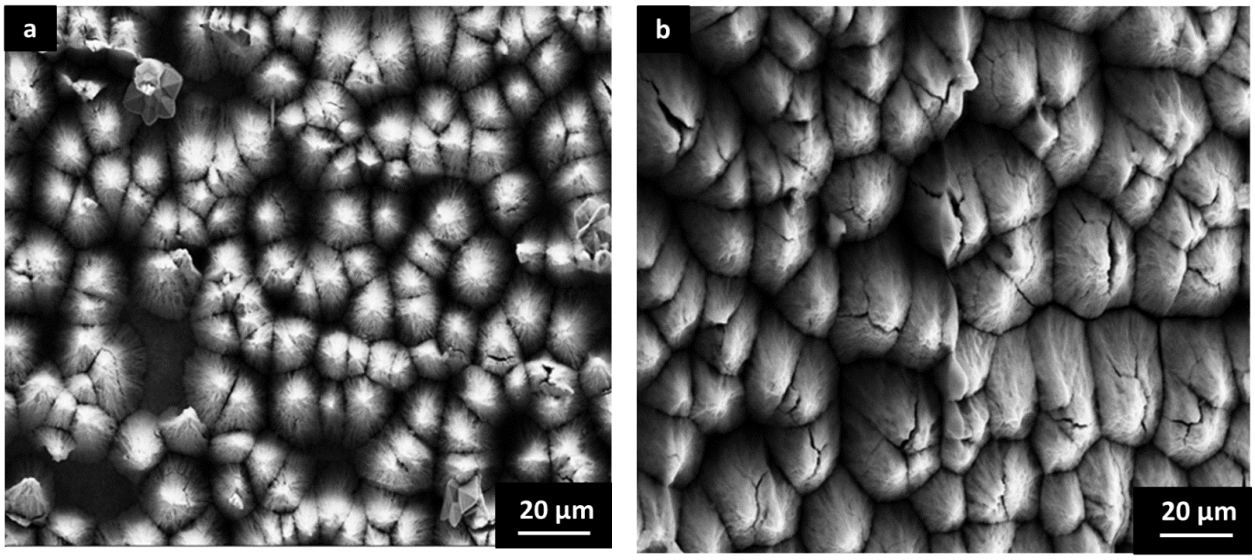

Figure 6-27: FESEM top-view images of (a) as-anodized Nb_2O_5 micro cones, and the Nb – O – N micro cones formed via annealing in ammonia atmosphere for 420 minutes.

Oxide samples S8, S9 and S10 annealed in air, as shown in **Table 6-5**, were tested for comparison. **Table 6-6** shows the concentrations of the major elements Nb, O, N and also the concentrations of carbon and fluorine in samples annealed in NH_3 compared to oxide samples S8, S9 and S10. The annealing temperature was almost constant (440 –

450 ^{0}C) so that the ammonia flow rate and the annealing duration were the main parameters to convert oxides into oxynitrides 450 ^{0}C).

Table 6-5: Conditions of fabricating Nb_2O_5 samples.

Sample Code	Fabrication Procedure
S8	Anodized Microcones - Air Annealing (450 ^{0}C – 20 minutes)
S9	Anodized Microcones - Air Annealing (450 ^{0}C – 300 minutes)
S10	Thermally oxidized by air annealing (450 ^{0}C– 300 minutes)

The investigation of oxynitrides by XPS is essential to prove the formation of oxynitrides through nitrogen doping rather than the surface adsorption of nitrogen. Adsorbed nitrogen has binding energy of ≈ 399 eV. However, oxynitride materials show nitrogen peaks of less binding energy due to N—O bonds. **Figures 6-28** shows the XPS spectra of sample S1. No peak for nitrogen was observed in the N 1s spectrum indicating that annealing in flow rate 50 sccm for 20 minutes is not sufficient to allow nitrogen doping. However, N peak appeared at binding energy of 397 eV in the sample S2 by increasing the flow rate to 150 sccm and the duration to 3 hours as shown in **Figure 6-29.** This peak can be related to the N - O bond, while the nitrogen peak observed at 400 eV can be related to adsorbed nitrogen. At a flow rate of 200 sccm and annealing duration of 20 minutes, sample S3 did not show a significant peak for nitrogen as shown in **Figure 6-30**. Increasing the flow rate to 300 sccm at the same annealing duration did not lead to the formation of a significant N peak as shown in **Figure 6-31.** On the other hand, N peak with a binding energy of 396 eV was found by increasing the annealing duration to 1 hour at a flow rate of 300 sccm as shown in **Figure 6-32**. High annealing duration was

found to be efficient at a flow rate of 200 sccm to produce high nitrogen doping. This was concluded from the significant N peaks found at 396 and 395 eV for durations 5 and 7 hours as shown in **Figure 6-33 and 6-34**, respectively. Spectra of Nb 3d and O 1s are analyzed for oxide samples S8, S9 and S10 as shown in **Figure 6-35, 6-36 and 6-37**, respectively. Analysis for the atomic concentrations of the main elements; niobium, oxygen, nitrogen, carbon and fluorine, is displayed in **Table 6-6**. It can be observed that the peaks of C 1s found in the samples were located in a range of binding energies (283 – 286 eV) that can be attributed to adventitious carbon from handling [22].

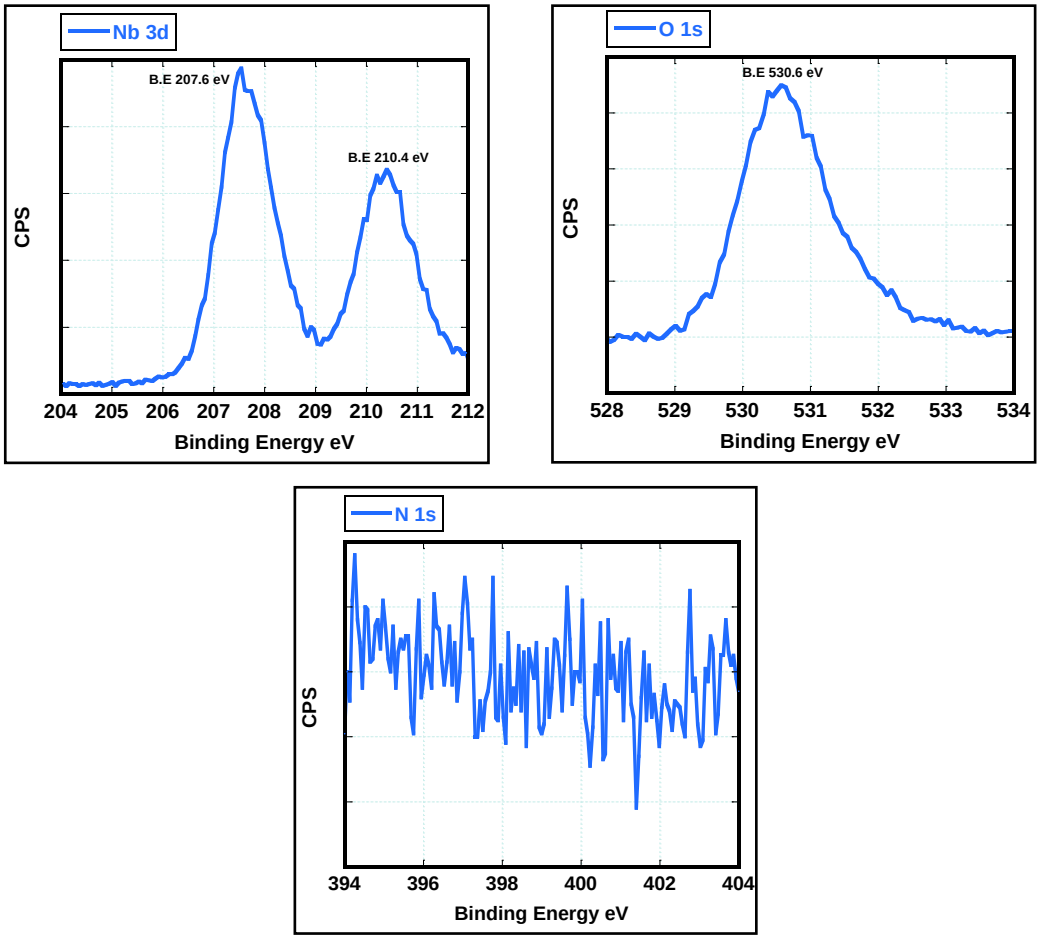

Figure 6-28: XPS Spectra of Nb 3d, O 1s and N 1s in microcones S1 annealed in NH_3 with flow rate 50 sccm at 440 ^{0}C for 20 min.

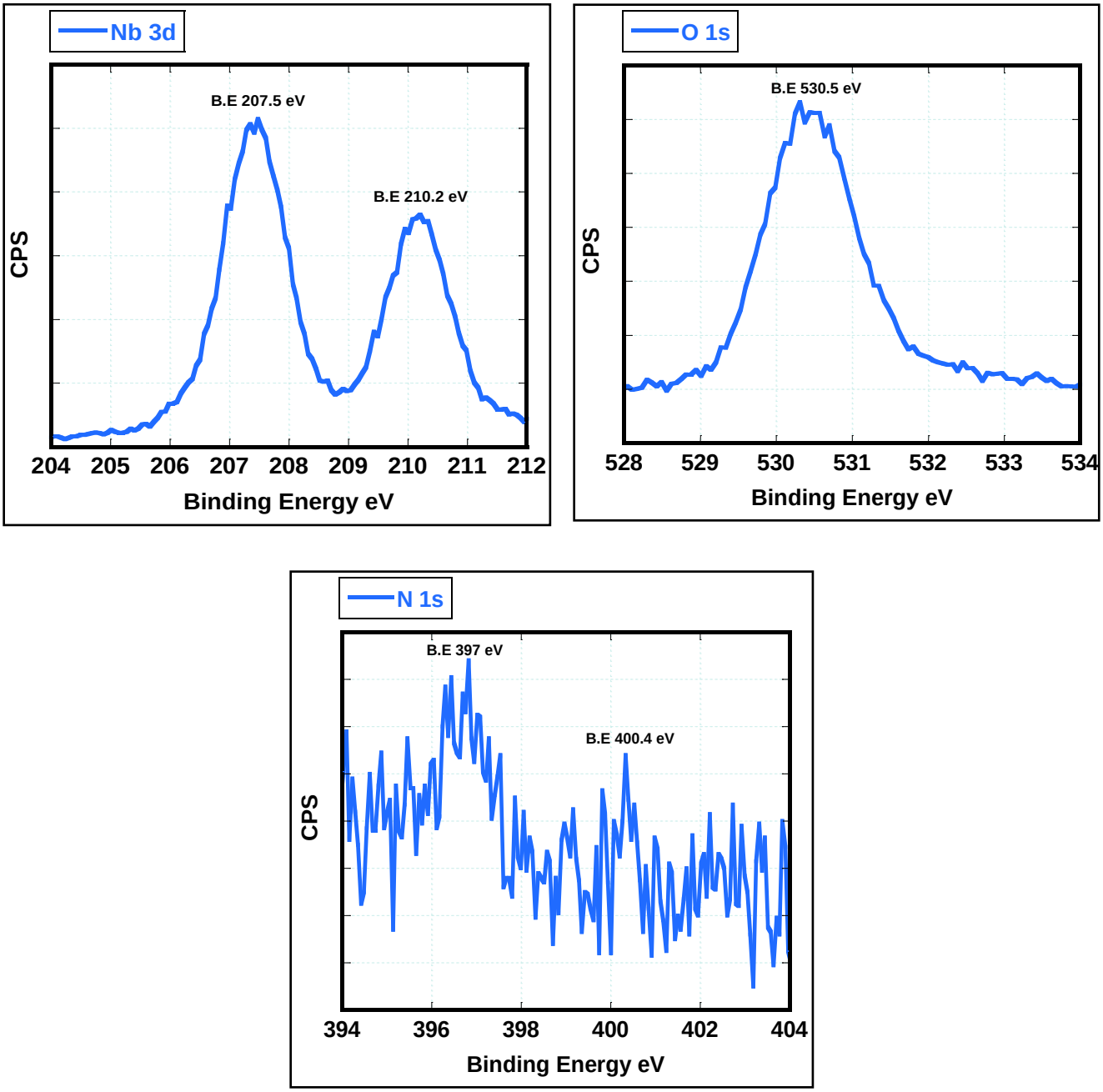

Figure 6-29: XPS Spectra of Nb 3d, O 1s and N 1s in microcones S2 annealed in NH_3 with flow rate 150 sccm at 450 ^{0}C for 180 min.

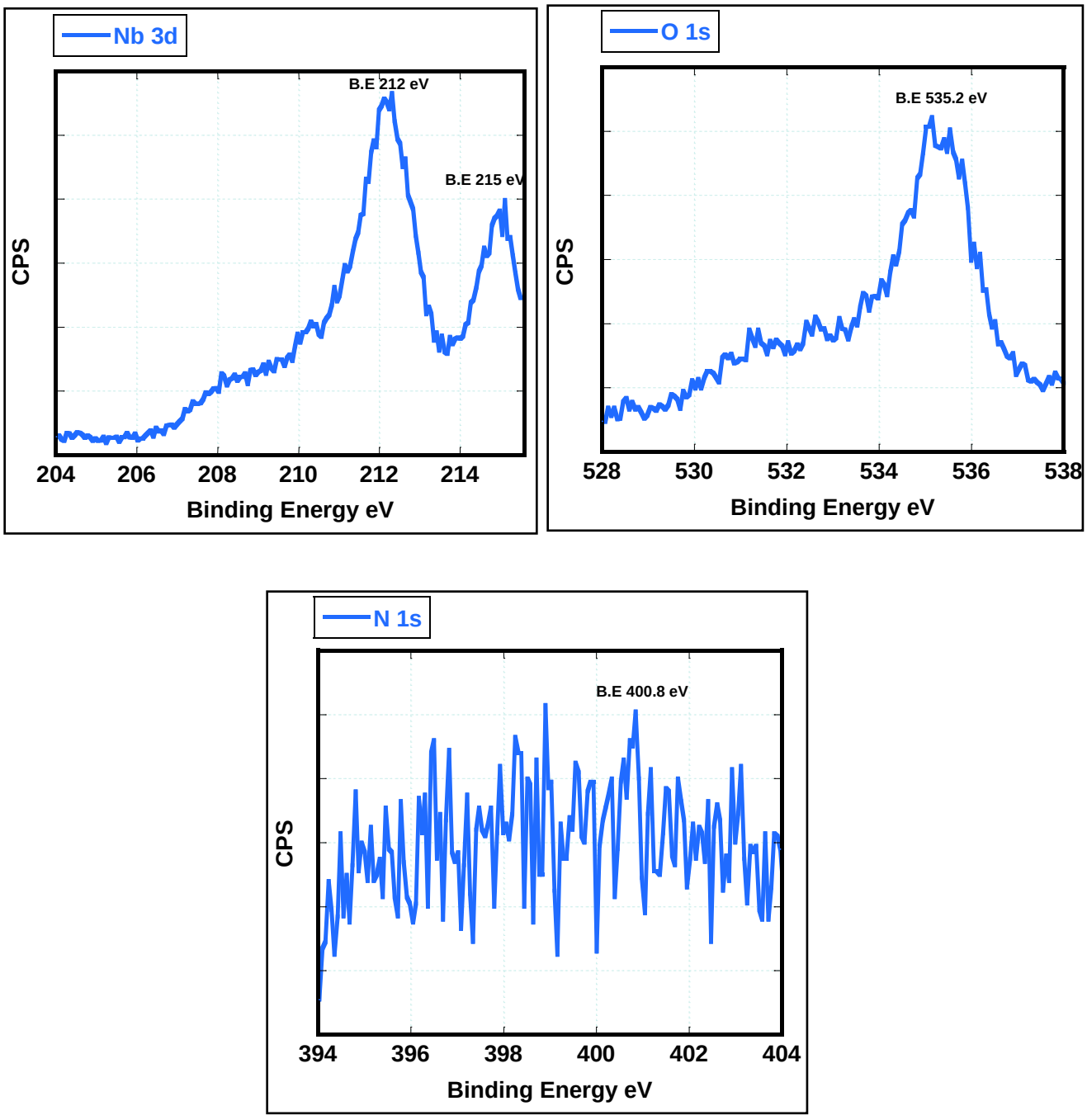

Figure 6-30: XPS Spectra of Nb 3d, O 1s and N 1s in microcones S3 annealed in NH_3 with flow rate 200 sccm at 440 ^{0}C for 20 min.

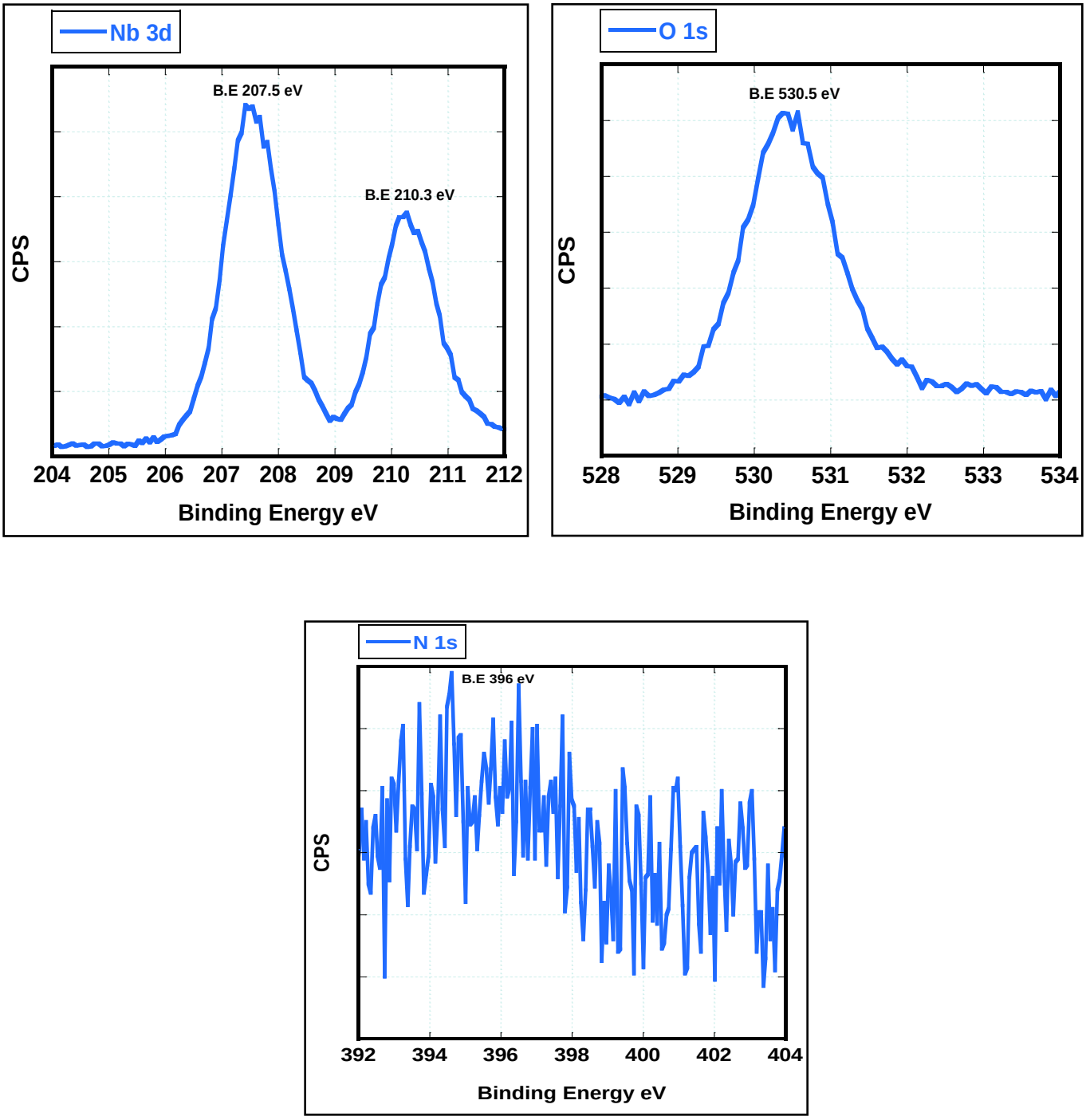

Figure 6-31: XPS Spectra of Nb 3d, O 1s and N 1s in microcones S4 annealed in NH_3 with flow rate 300 sccm at 450 ^{0}C for 20 min.

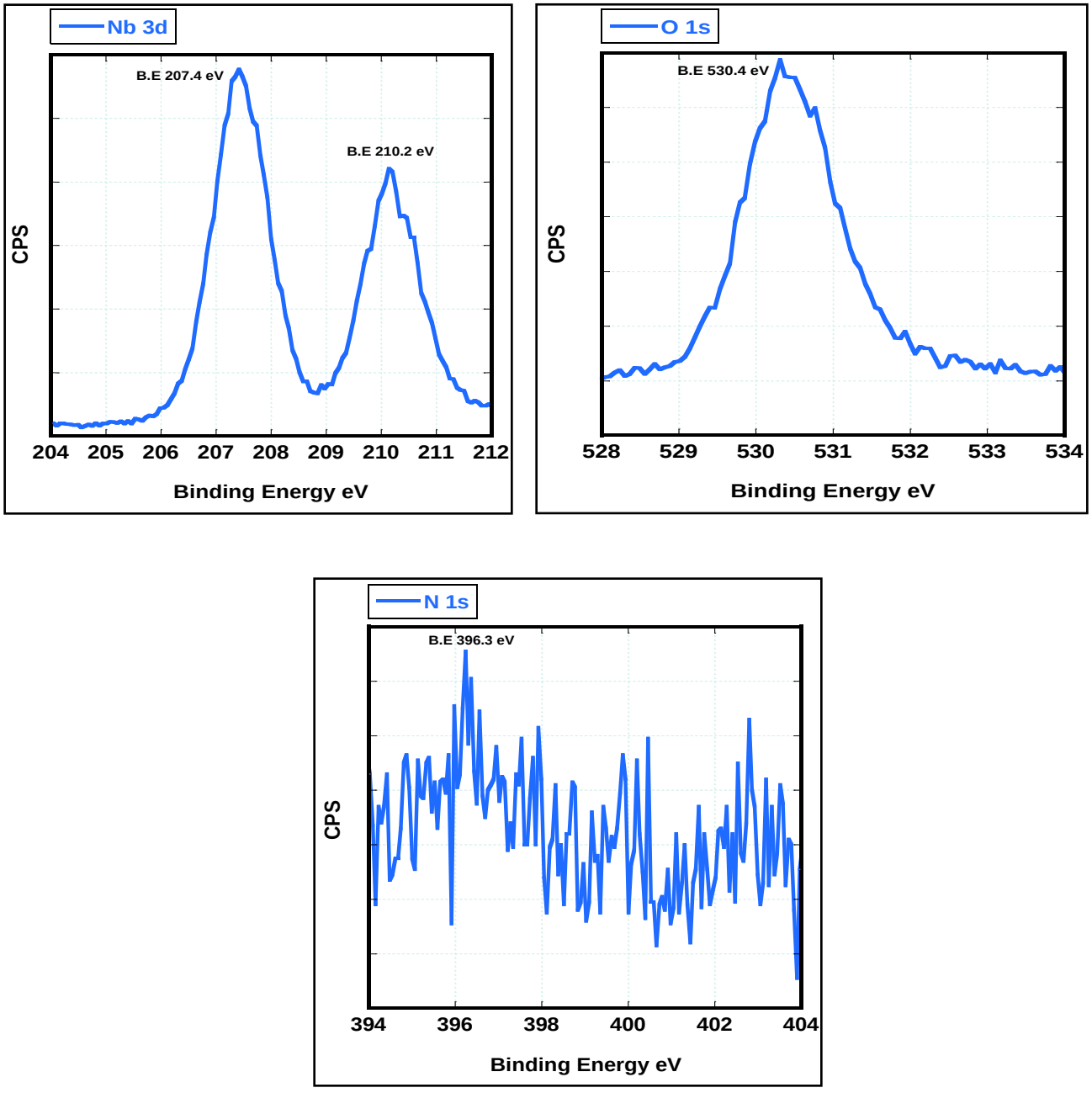

Figure 6-32: XPS Spectra of Nb 3d, O 1s and N 1s in microcones S5 annealed in NH_3 with flow rate 300 sccm at 450 ^{0}C for 60 min.

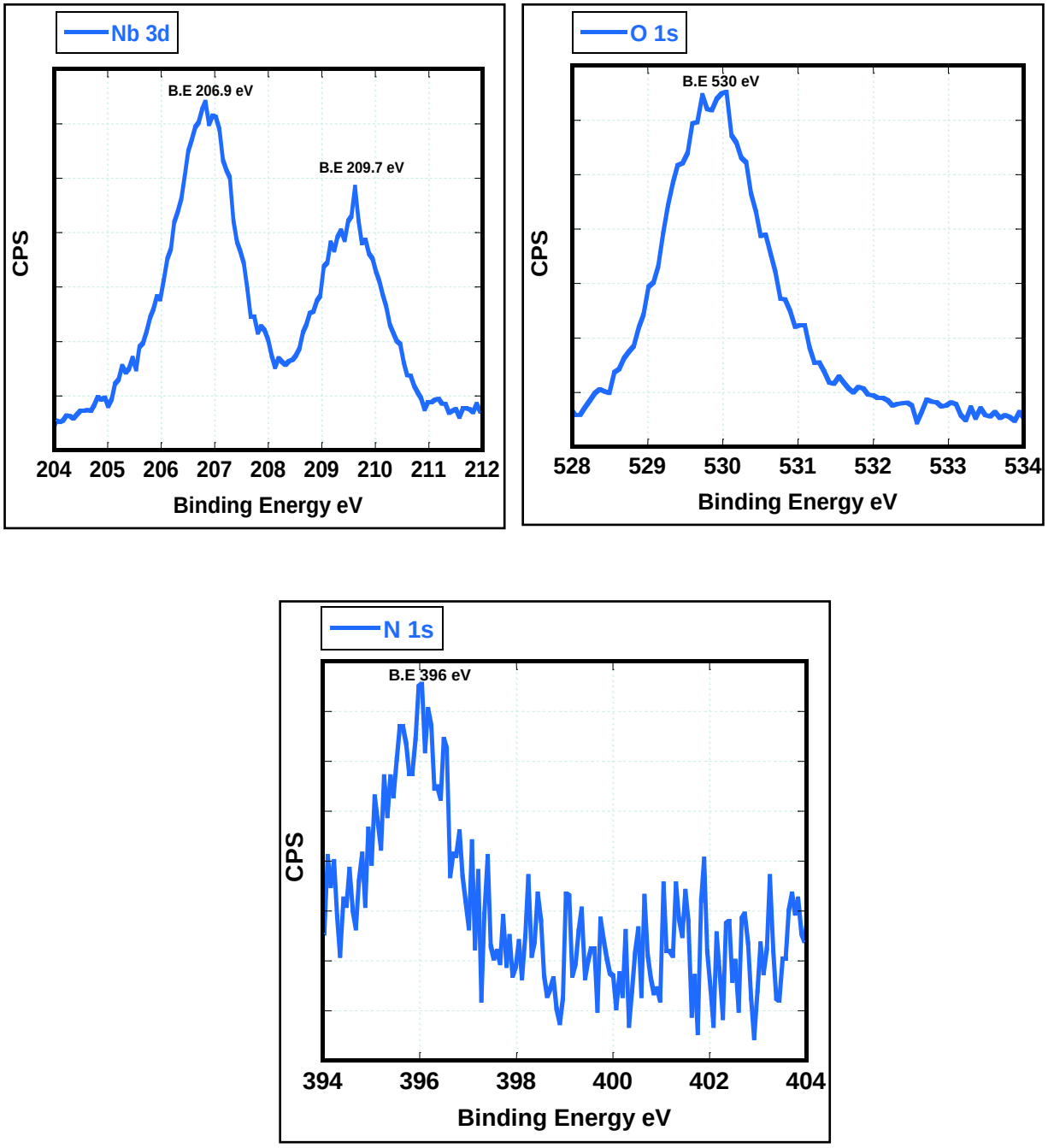

Figure 6-33: XPS Spectra of Nb 3d, O 1s and N 1s in microcones S6 annealed in NH_3 with flow rate 200 sccm at 450 ^{0}C for 300 min.

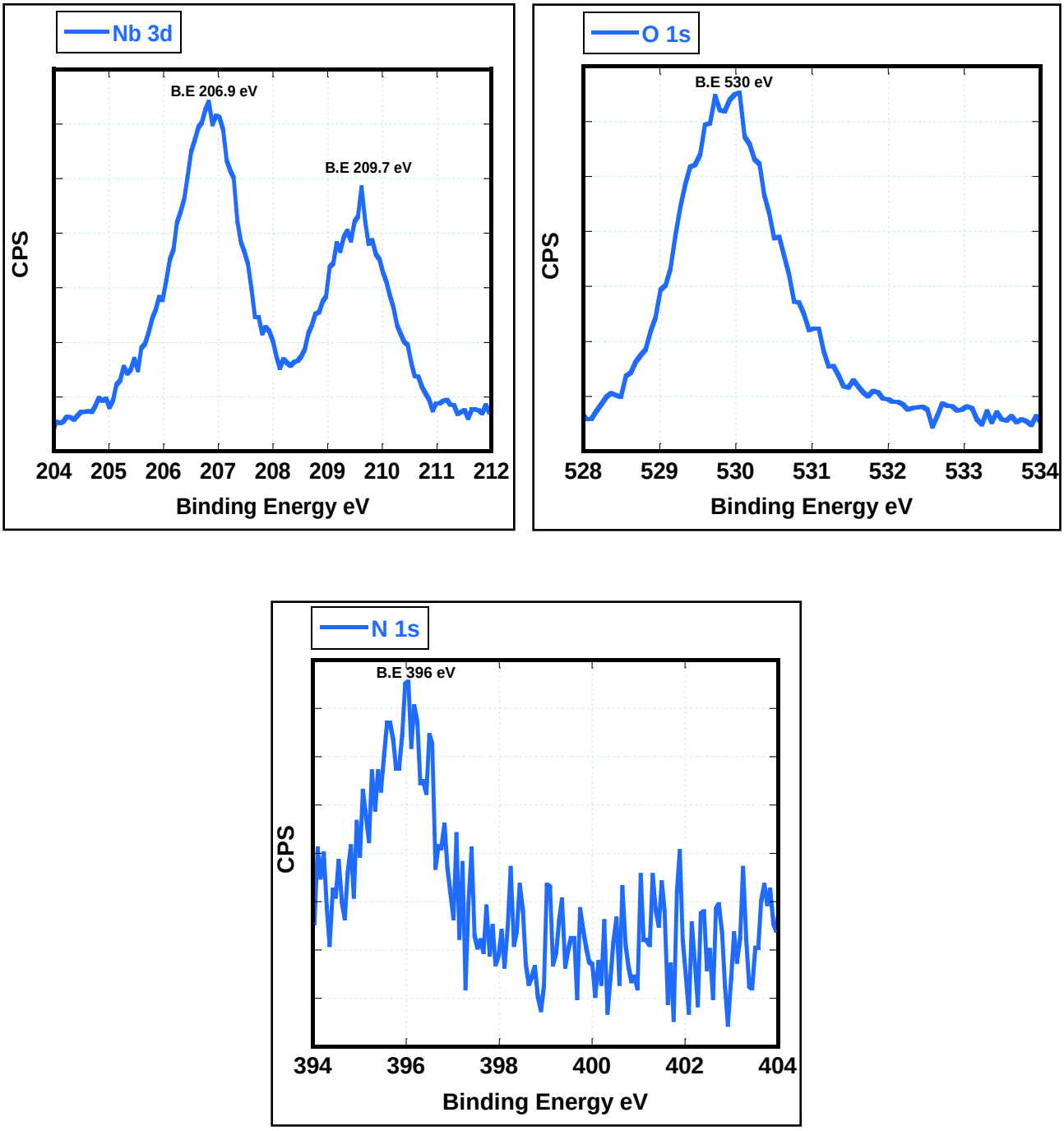

Figure 6-34: XPS Spectra of Nb 3d, O 1s and N 1s in microcones S7 annealed in NH_3 with flow rate 200 sccm at 450 ^{0}C for 480 min.

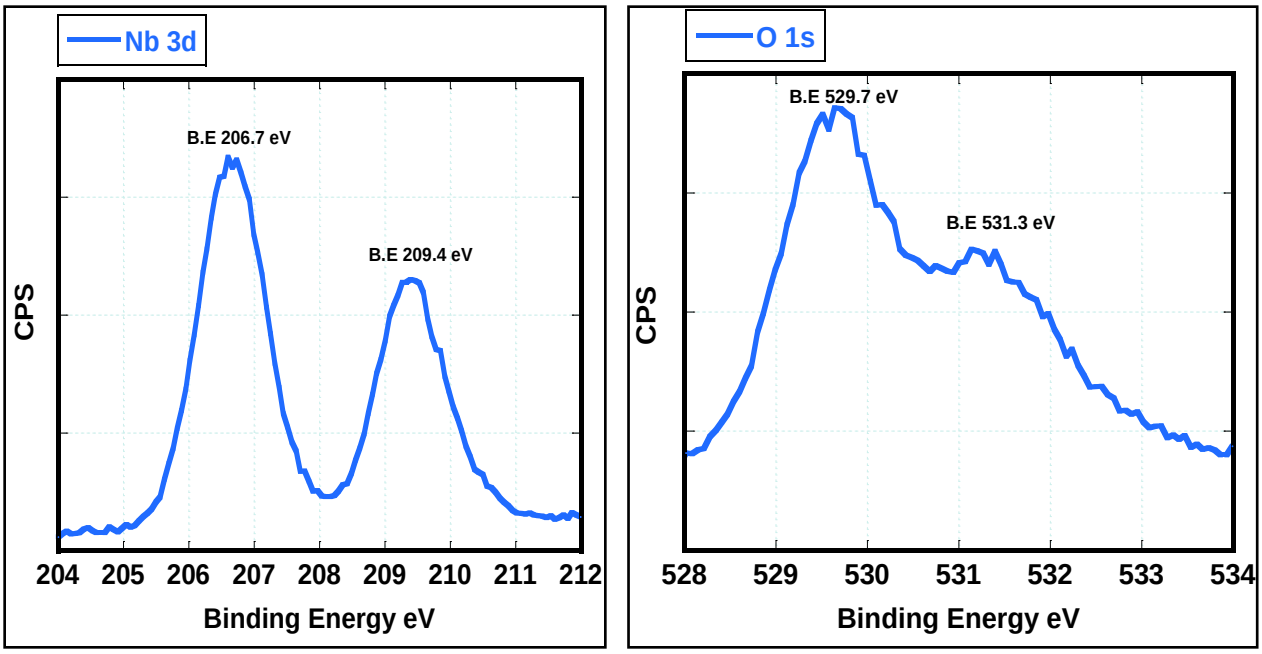

Figure 6-35: XPS Spectra of Nb 3d and O 1s in microcones S8 annealed in air at 440 ^{0}C for 20 min.

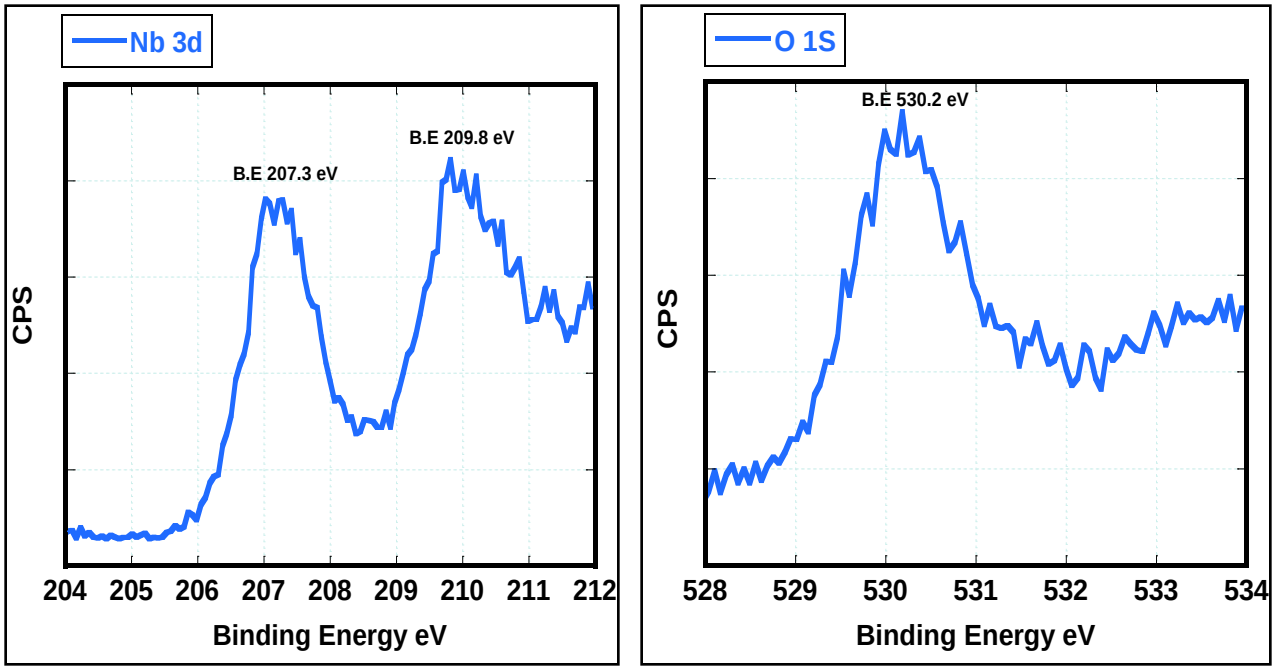

Figure 6-36: XPS Spectra of Nb 3d and O 1s in microcones S9 annealed in air at 440 ^{0}C for 300 min.

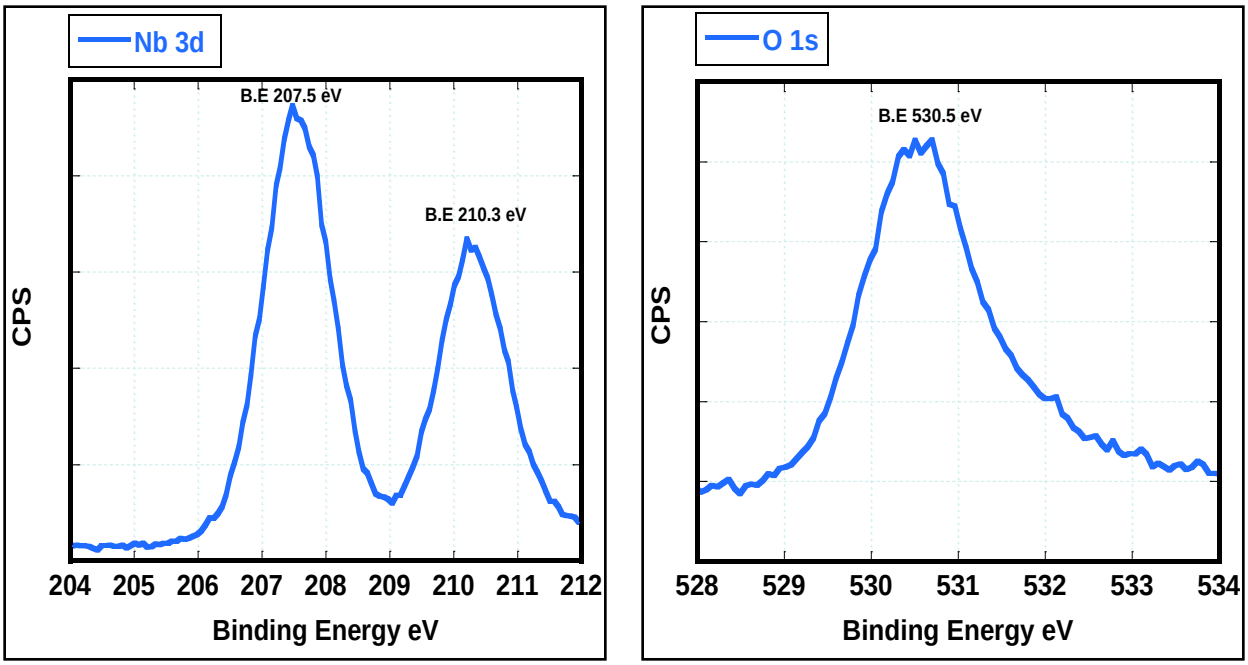

Figure 6-37: XPS Spectra of Nb 3d and O 1s in thermal oxide film S10 annealed in air at 450 ^{0}C for 300 min.

Table 6-6: The atomic concentrations and the positions of peaks of the main elements (Nb, N, O, C and F) obtained from XPS survey analysis.

Element / **Sample**	**Nb 3d**		**N 1s**		**O 1s**		**C 1s**		**F 1s**	
	At. %	Position	At. %	Position	At. %	Position	At. %	Position	At. %	Position
S1	23.2	210	0.31	396	67	531	6	286	3.3	685
S2	24.2	208	2.51	397	65.2	531	6.9	285	1.2	685
S5	29	210	0.9	394	64.7	531	5.5	285	0	-
S6	28.6	206	3	394	60	529	7.3	283	1.2	682
S7	28	206	5.7	395	64.2	529	1.3	283	0.8	683
S8	31.64	207	0.83	401	65.5	530	2	285	0	-
S9	16.9	207	0	-	73	530	10.2	284	0	-
S10	17.53	207	0	-	75	530	7.5	285	0	-

The XRD patterns of the oxynitride samples (S1 to S7) are shown in **Figure 6-38**, and compared to one oxide sample (S8). No significant difference in the peaks can be observed between the oxynitrides and the oxide sample. On the other hand, peaks appearing at 27^{o} and 50^{o} are attributed to (100) and (110) planes of orthorhombic Nb_2O_5.

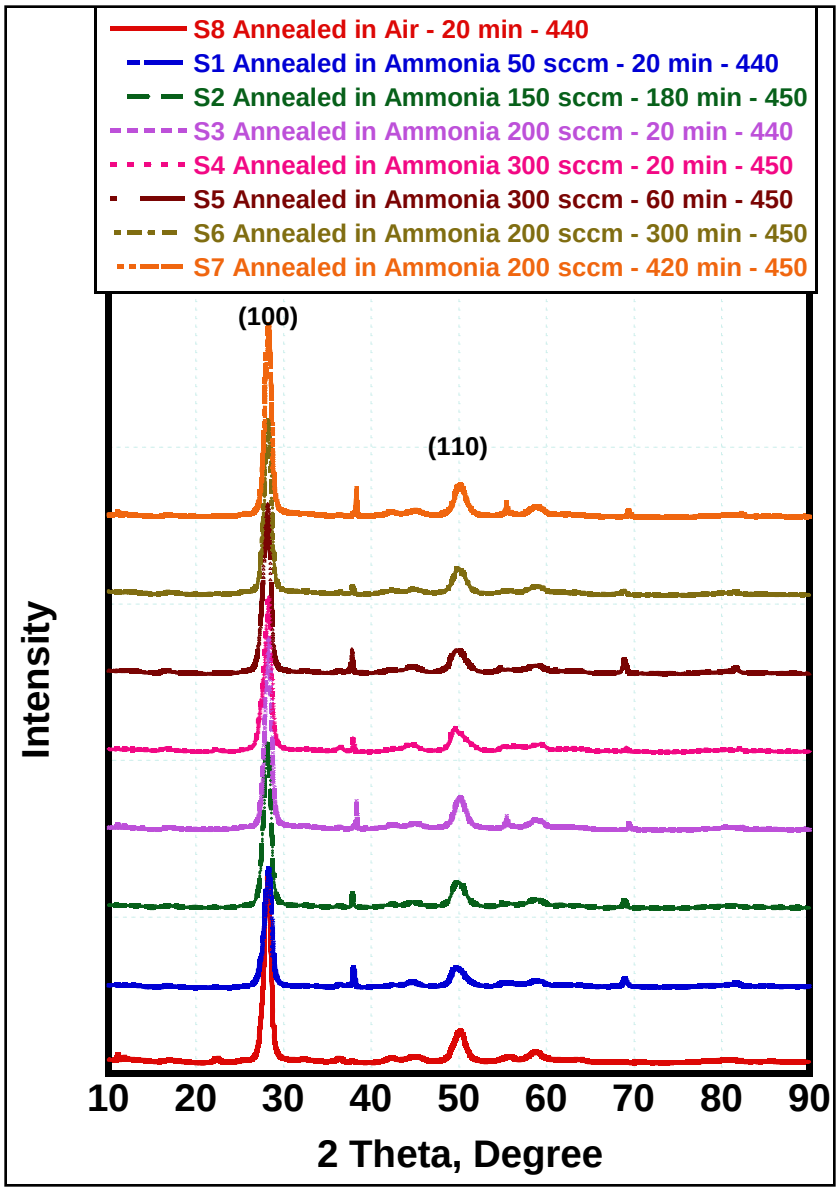

Figure 6-38: GAXRD diffraction patterns of microcones annealed in ammonia (S1, S2, S3, S4, S5, S6, and S7) compared to Nb_2O_5 microcones annealed in air for 20 min at 450 ^{0}C (S8).

For more structural analysis, Raman spectroscopy for oxynitride samples (S6 and S7) is compared to that of oxide sample (S9). **Figure 6-39** shows that the oxide sample (S9) has more prominent peaks than the oxynitride samples (S6 and S7). The band at 235 cm^{-1} is characteristic for Nb_2O_5. The peaks at 700 and 310 cm^{-1} can be indicative of the orthorhombic crystal structure of Nb_2O_5, which is in agreement with the XRD results.

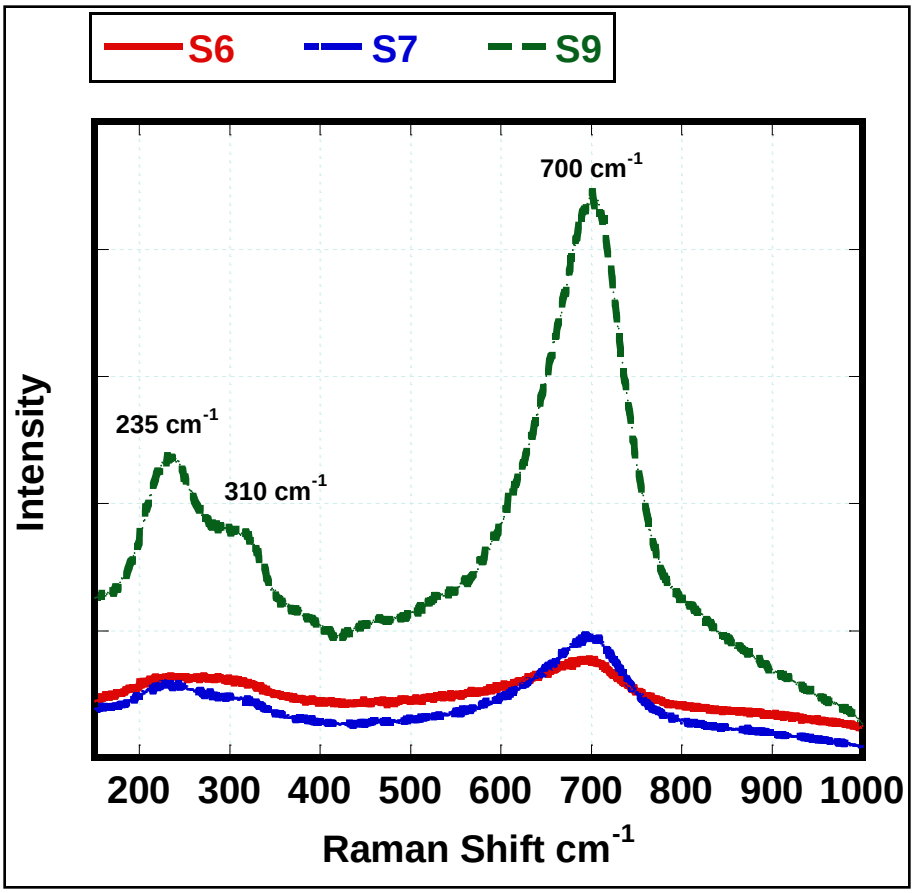

Figure 6-39: Raman spectra of microcones annealed in ammonia (S6 and S7) compared to Nb_2O_5 microcones annealed in air for 5 hours at 450 ^0C (S9).

6.3.2 Optical Characterization

As explained before, the optical properties are one factor to determine the performance of photoelectrodes. Since it was confirmed by the XPS that nitrogen doping was done at some conditions, it is expected to find differences in the optical properties. Therefore, the UV-Vis absorption of samples annealed in ammonia was measured and compared with niobium oxide sample (S8) at different incident angles from 10 to 60 degrees. The optical absorption was shown to be angle-dependent in silicon wires and gallium arsenide nanowires [23-24]. Illustration for the reflection measurements at different angles is shown in **Figure 6-40**. It was observed in all samples (S1-S8) that the highest red shift is obtained at incident angle of 60^0 as shown in **Figure 6-41 and 6-42**.

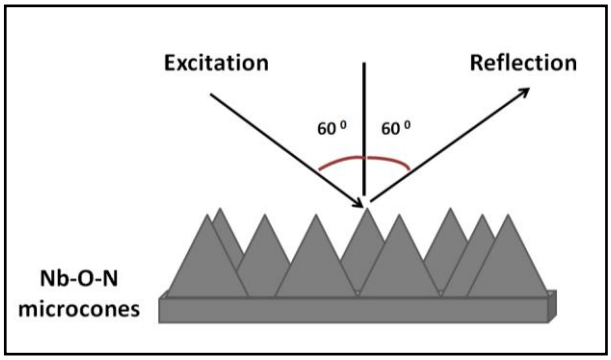

Figure 6-40: Illustration of the reflection measurements of microcones at different angles.

In addition, the red shift increases with the increase in the amount of nitrogen doping. The absorption spectra of all the samples are drawn together in **Figure 6-43** for better comparison. This absorption increase can be related to the decrease in the bandgap upon the increase in the amount of nitrogen doped in the material. **Table 6-7** summarizes the maximum absorption and the corresponding optical bandgap determined from the equation: $E = \frac{1240}{\lambda}$, where E is the bandgap energy and λ is the wavelength in nm.

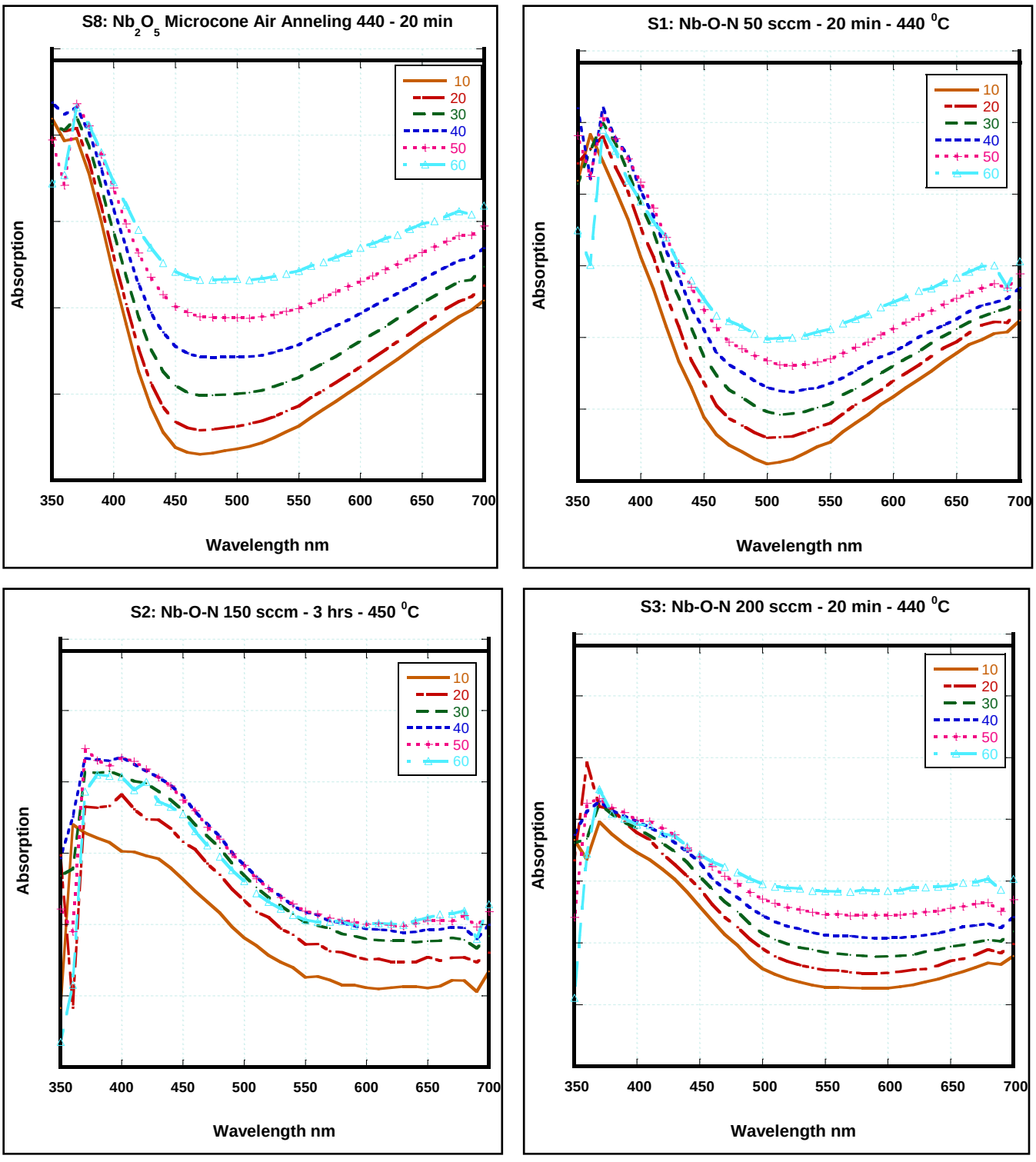

Figure 6-41: The absorption spectra at different incident angles of niobium oxide microcones (S8), and samples annealed in ammonia (S1, S2, and S3).

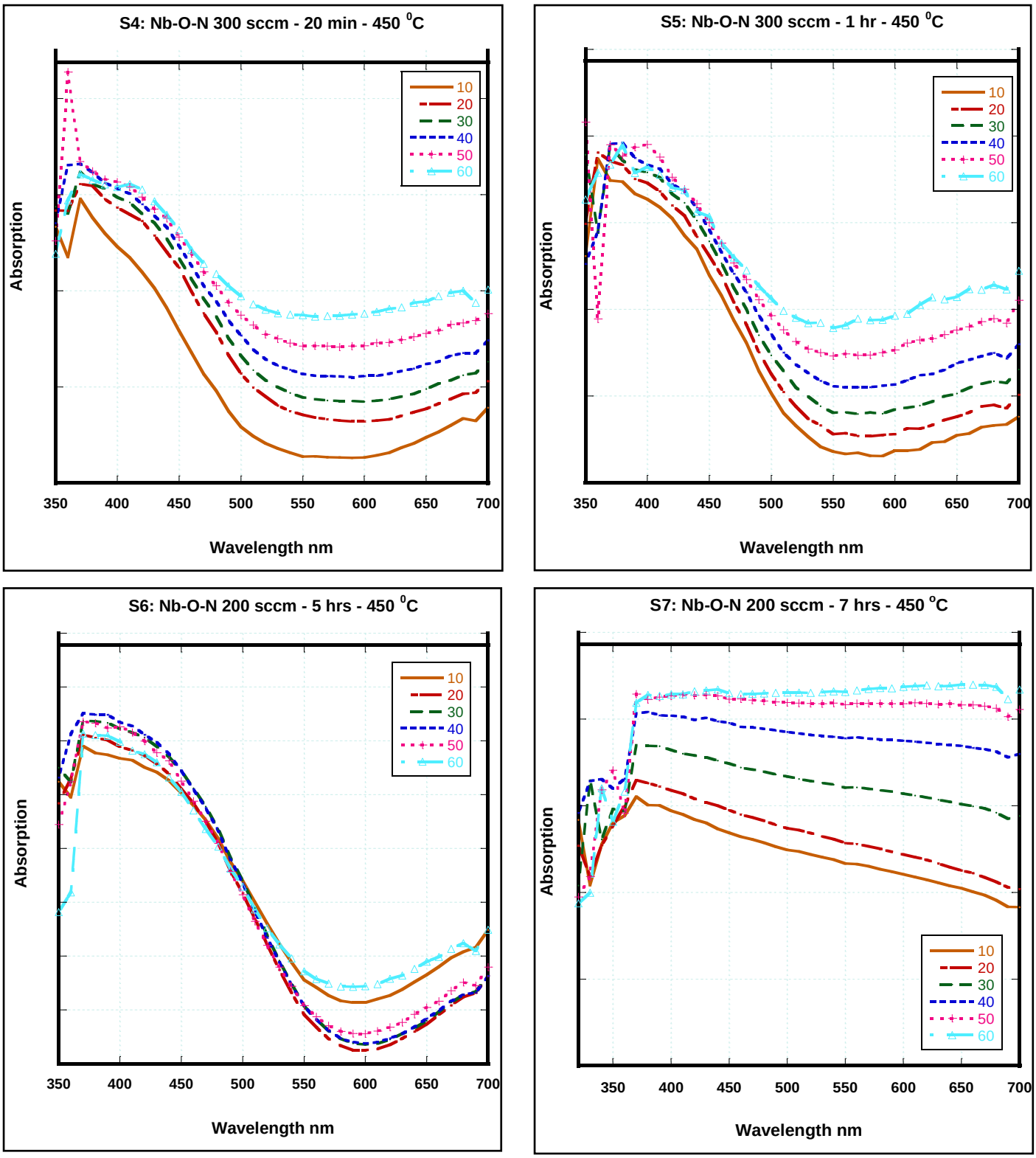

Figure 6-42: The absorption spectra at different incident angles of samples annealed in ammonia (S4, S5, S6 and S7).

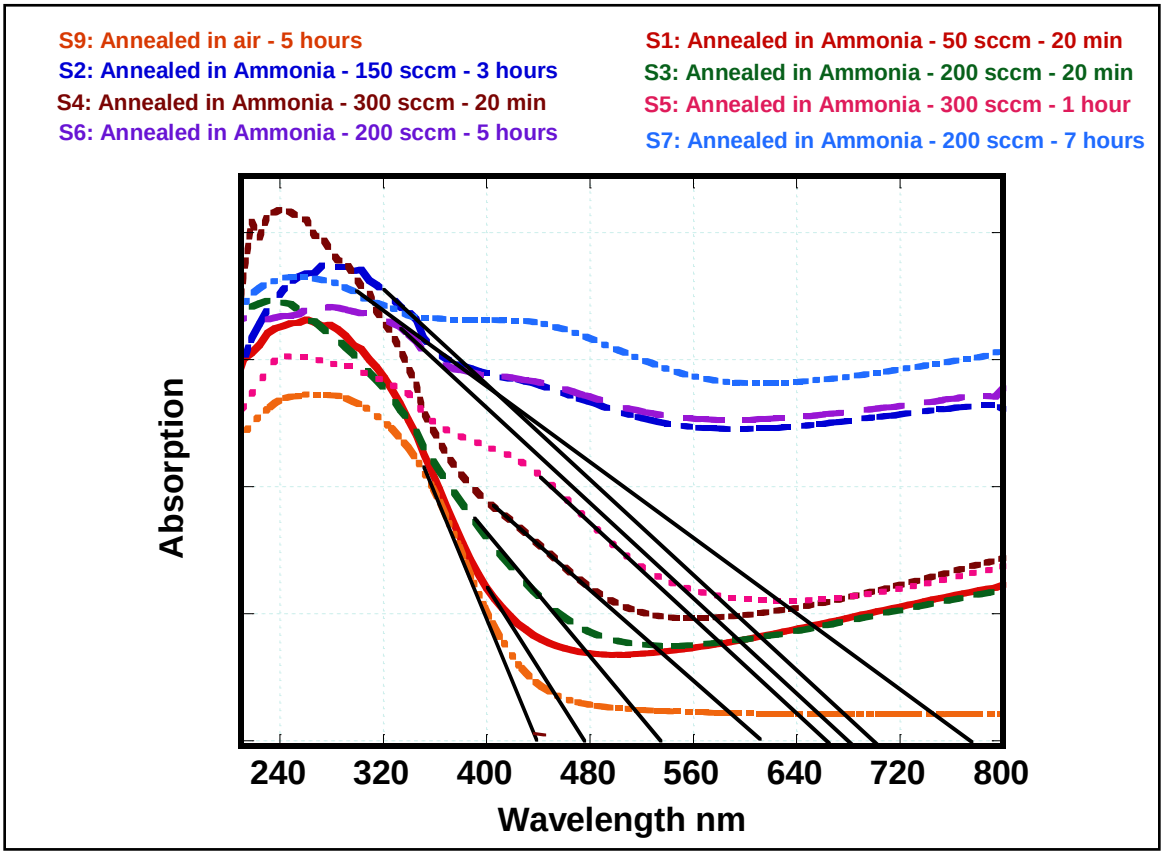

Figure 6-43: The absorption spectra of niobium microcones annealed in ammonia at different conditions (S1, S2, S3, S4, S5, S6, and S7) compared to that annealed in air for 5 hours (S9).

Table 6-7: The maximum absorption and optical bandgap of niobium oxynitride microcones compared with niobium oxide.

Sample	Maximum Wavelength, nm	Optical Bandgap, eV
S9	440	2.8
S1	478	2.6
S2	700	1.77
S3	534	2.32
S4	615	2.01
S5	665	1.86
S6	683	1.82
S7	777	1.56

For more optical characterization, the photoluminescence (PL) properties were measured at room temperature using excitation source of wavelength 325 nm to measure the material's emission upon excitation. **Figure 6-44** shows the PL spectra of niobium oxynitride microcones annealed in ammonia at 300 sccm for one hour (S5) and that annealed at 200 sccm for seven hours (S7) compared to niobium oxide sample (S8). It is observed that the same peaks appear in the three samples at approximately 350, 380 and 470 nm. However, the intensity of the peaks is higher in the oxynitride samples in comparison with the oxide sample, especially for the peak at 470 nm. In addition, the oxynitride sample (S7) that has higher amount of nitrogen, shows higher peak intensity than S3 which is attributed to the higher density of photogenerated electrons and holes [25]. Liu *et al.* showed the PL spectra at the same excitation wavelength for single-crystalline nanoporous Nb_2O_5 nanotubes where the most prominent peak appeared at nearly 370 nm [26].

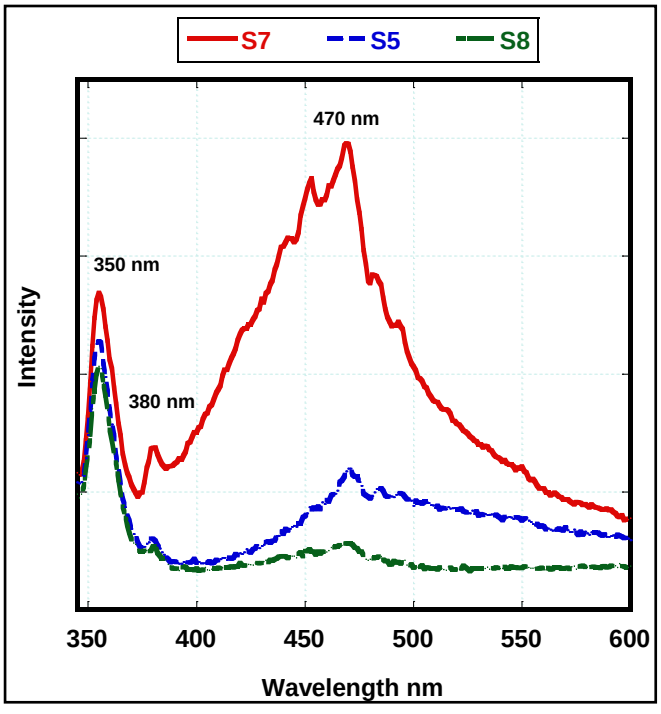

Figure 6-44: PL spectra of niobium oxynitride microcones (S5: annealed in ammonia at flow rate of 300 sccm for 1 hour and S7: annealed in ammonia at flow rate of 200 sccm for 7 hours) compared to niobium oxide microcone (S8: annealed in air for 20 minutes).

Both the absorption and the PL spectra revealed the enhanced optical properties of the oxynitride samples. In addition, the good optical properties depend on the amount of nitrogen doping, which is controlled by the annealing conditions.

6.3.3 Photoelectrochemical Characterization

The photoelectrochemical properties of niobium oxide and oxynitride microcones were measured in aqueous solutions of 1 M Na_2SO_4 under constant external bias of 0.5 V under AM 1.5 illumination. **Figure 6-45** shows the photocurrent-time measurements for the oxynitride sample S5 (annealed in ammonia at flow rate of 300 sccm for 1 hour) compared to as-anodized niobium oxide microcone (1 M NaF + 1 ml HF at 40 V for 50 minutes). It can be observed that the photocurrent of the oxynitride sample (~ 33 µA/ cm^2) is higher than that of the as-anodized oxide sample (~ 12 µA/ cm^2). However, the dark current increases in the oxynitride sample showing that there are trapped charges.

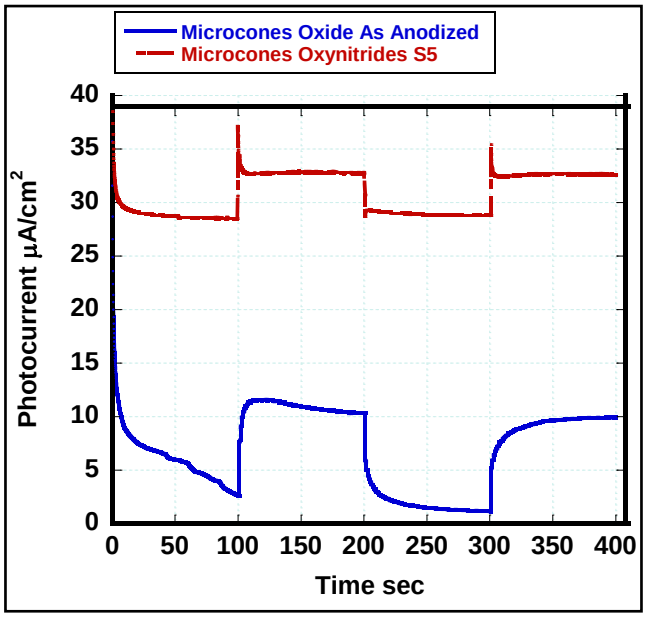

Figure 6-45: Photocurrent-time measurement of niobium oxynitride microcones S5 (annealed in ammonia at flow rate of 300 sccm for 1 hour) compared to niobium oxide sample (as anodized in 1 M NaF + 1 ml HF electrolyte at 40).

Note that the S5 sample produced the most consistent current among the other oxynitride samples. Despite the enhancement in the optical properties achieved by the formation of niobium oxynitride microcones with various amounts of nitrogen, the photoelectrochemical properties are still low to be considered as efficient photoanodes for solar-water splitting. Yet, It is much higher than the highest reported photocurrent for niobium oxynitride thin films [27]. Therefore, a thorough study of the charge dynamics is required to understand the trapping-detrapping mechanism in such newly-developed structures.

References

1. Ou, J. Z.; Rani, R. A.; Ham, M. H., Field, M. R.; Zhang, Y.; Zheng, H.; Reece, P.; Zhuiykov, S.; Sriram, S.; Bhaskaran, M.; Kaner, R. B., Kalantar-zadeh, K. Elevated Temperature Anodized Nb_2O_5: A Photoanode Material with Exceptionally Large Photoconversion Efficiencies. *ACS Nano* **2012**, 6, 4045-4053.
2. Jeong, B. Y.; Jung, E. H. Micro-Mountain and Nano-Forest Pancake Structure of Nb2O5 with Surface Nanowires for Dye-Sensitized Solar Cells. *Met. Mater. Int.* **2013**, 19, 617-622.
3. Polman, A.; Atwater, H. A. Photonic design principles for ultrahigh-efficiency photovoltaics. *Nature Materials* **2012**, 11, 174-177.
4. Atwater, H. A.; Polman, A. Plasmonics for improved photovoltaic devices. *Nature Materials* **2010**, 9, 205-213.
5. Kosten, E. D; Atwater, J. H; Parsons, J.; Polman, A.; Atwater, H. A. Highly efficient GaAs solar cells by limiting light emission angle. *Light: Science & Applications* **2013**, 2.
6. Allam, N. K.; Grimes, C. A. Room Temperature One-Step Polyol Synthesis of Anatase TiO_2 Nanotube Arrays: Photoelectrochemical Properties. *Langmuir* **2009**, 25, 7234–7240.
7. Karlinsey, R. L. Self-assembled Nb_2O_5 microcones with tailored crystallinity. *J. Mater. Sci.* **2006**, 41, 5017-5020.
8. Yang, S.; Aoki, Y.; Habazaki, H. Effect of electrolyte temperature on the formation of self-organized anodic niobium oxide microcones in hot phosphate–glycerol electrolyte. *Appl. Surf. Sci.* **2011**, 257, 8190-8195.

9. Yanga, S.; Habazakia, H.; Fujiia, T.; Aokia, Y.; Skeldonb, P.; Thompson, G. E. Control of morphology and surface wettability of anodic niobium oxide microcones formed in hot phosphate–glycerol electrolytes. *Electrochim. Acta* **2011**, 56, 7446-7453.
10. Liu, J.; Xue, D.; Li, K. Single-crystalline nanoporous Nb_2O_5 nanotubes *Nanoscale Res. Lett*, **2011**, 6, 138-146.
11. Mickova, I. Photoelectrochemical Study of Anodically Formed Oxide Films on Niobium Surfaces. *Croat. Chem. Acta* **2010**, 83, 113–120.
12. Zhao, Y.; Zhang, Z.; Lin, Y. Optical and dielectric properties of a nanostructured NbO_2 thin film prepared by thermal Oxidation. *J. Phys. D: Appl. Phys.* **2004**, 37, 3392–3395.
13. Weibin, Z.; Weidong, W.; Xueming, W.; Xinlu, C.; Dawei, Y.; Changle, S.; Liping, P.; Li, W. Y. B. The investigation of NbO_2 and Nb_2O_5 electronic structure by XPS, UPS and first principles methods. *Surf. Interface Anal.* **2013**, 45, 1206-1210.
14. Razinkin, A. S.; Shalaeva, E. V.; Kuznetsov, M. V. Photoelectron Spectroscopy and Diffraction of NbO*x*/Nb (110) Surface. *Phys. Met. Metallogr*. **2008**, 106, 56-66.
15. Vermilyea, D. A. The Crystallization of Anodic Tantalum Oxide Films in the Presence of a Strong Electric Fields. *J. Elechtrochem. Soc.* **1955**, 102, 207-214.
16. Habazaki, H.; Ogasawara, T.; Konno, H.; Shimizu, K.; Nagata, S.; Skeldon, P.; Thompson, G. E. Field crystallization of anodic niobia. *Corros. Sci.* **2007**, 49, 580–593.
17. Lim, J. H.; Park, G.; Choi, J. Synthesis of niobium oxide nanopowders by field-crystallization-assisted anodization *Curr. Appl. Phys.* **2012**, 12, 155-159.
18. Nico, C.; Rino, L.; Matos, M.; Monteiro, R.; Costa, F. M.; Monteiro, T.; Grac, M. P.F. NbO/Nb_2O_5 core–shells by thermal oxidation. *J. Eur. Ceram. Soc.* **2013**, 33, 3077-3083.

19. Fenker, M; Kappl, H.; Banakh, O.; Martin, N.; Pierson, J. F. Investigation of Niobium Oxynitride thin films deposited by reactive magnetron sputtering. *Surface & Coatings Technology* **2006**, 201, 4152-4157.

20. Matylitskaya, V. A.; Bock, W.; Thoma, K.; Kolbesen, B. O. Formation of niobium oxynitrides by rapid thermal processing (RTP). *Applied Surface Science* **2005**, 252, 205-210.

21. Yamada, K.; Masuda, H.; Sato, N.; Fujino, T. Synthesis and Crystal Structure of a New Niobium Oxynitride $Nb_2N_{0.88}O_{0.12}$. *Journal of Solid State Chemistry* **2000**, 150, 36-42.

22. Allam, N. K.; Shankar, K.; Grimes, C. A. Photoelectrochemical and water photoelectrolysis properties of ordered TiO_2 nanotubes fabricated by Ti anodization in fluoride-free HCl electrolytes. *J. Mater. Chem.* **2008**, 18, 2341–2348.

23. Boettcher, S. W; Warren, E. L.; Putnam, M. C.; Santori, E. A.; Turner-Evans, D.; Kelzenberg, M. D.; Walter, M. G.; McKone, J. R.; Brunschwig, B. S.; Atwater, H. A.; Lewis, N. S. Photoelectrochemical Hydrogen Evolution Using Si Microwire Arrays. *J. Am. Chem. Soc.* **2011**, 133, 1216–1219.

24. Hu, S.; Chi, C. –Y.; Fountaine, K. T.; Yao, M.; Atwater, H. A.; Dapkus, P. D.; Lewis, N. S.; Zhou, C. Optical, electrical, and solar energy-conversion properties of gallium arsenide nanowire-array Photoanodes. *Energy Environ. Sci.* **2013**, 6, 1879–1890.

25. Gfroerer, T. H. Photoluminescence in Analysis of Surfaces and Interfaces. *Encyclopedia of Analytical Chemistry* **2002**, 9209–9231.

26. Liu, J.; Xue, D.; Li, K. Single-crystalline nanoporous Nb_2O_5 nanotubes. *Nanoscale Research Letters* **2011**, 6, 138 – 146.

27. Ruffa, T.; Hahna, R.; Killiana, M.S.; Asohb, H.; Onob, S.; Schmuki, P. Visible light photo response from N-doped anodic niobium oxide after annealing in ammonia atmosphere, *Electrochimica Acta* **2012**, 62 402–407.

Chapter 7

Conclusions and Future Work

From the work presented in chapters 5 and 6, the following conclusions are drawn:

1- The mixed oxide system of Zn-Ti-O proved the same concept investigated in the core-shell structure that the difference in the band edge positions between ZnO and TiO_2 influences on the IPCE.

2- The vertically oriented ZnO/TiO_2 heterojunctions can offer a great potential as a material architecture for water oxidation due to their suitable band edge positions and high IPCE (~ 80 % higher than pure TiO_2 nanotubes).

3- Potentiostatic anodization of niobium results in the formation of a variety of niobium oxide morphologies; nanoporous, nanorods, nanochannels and microcones with nano-like wire structure by varying anodization parameters as electrolyte, voltage and time.

4- In-situ crystallization of as-anodized Nb_2O_5 microcones at room temperature is found to be affected by the electrolyte composition; specifically the concentration of sodium salt (NaF). Forming highly crystalline orthorhombic - Nb_2O_5 microcones from anodization can save additional processes for annealing. In addition, analysis of the annealed microcones in air (450 ^{0}C - 20 min) revealed the formation of mixed niobium oxide phases (Nb_2O_5 and NbO_2) which may be desirable for optoelectronics applications, however it might be unfavorable in photocatalytic applications.

5- Niobium oxynitride microcones with various nitrogen contents were formed by thermal ammonolysis, for the first time, at mild conditions. The absorption was dramatically enhanced reaching a maximum of 777 nm for niobium oxynitride annealed at ammonia flow rate of 200 sccm for 7 hours preserving the microcone structure. In addition, the intensity of PL emission at 470 nm is highly increased compared to niobium oxide microcones. The photoelectrochemical properties were still low, although they are higher than the oxide microcones and they are also higher than the best reported photocurrent for niobium oxynitride thin films.

Finally, here are some points that are suggested for future work:

1- Other combinations of Ti-Zn mixed oxides can be studied in attempt to further enhance the photocatalytic performance and get benefit from the difference in the band positions.
2- A thorough study is required to investigate the charge dynamics in niobium oxide and niobium oxynitride microcones.
3- Further development techniques can be investigated for niobium oxide photoanodes. Primary investigations were done for decorating Nb_2O_5 with plasmonic gold nanoparticles and rhodium (Rh). **Figure 7-1 and 7-2** show the FESEM images and EDX of Nb_2O_5 nanopores decorated with gold nanoparticles. **Figure 7-3** shows the UV-Vis absorption spectra of Au- Nb_2O_5 nanopores that reveal the plasmonic effect of the gold nanoparticles by showing absorption peak at ~ 550 nm. Enhancement in the optical absorption by Rh decoration is also shown in **Figure 7-4**.

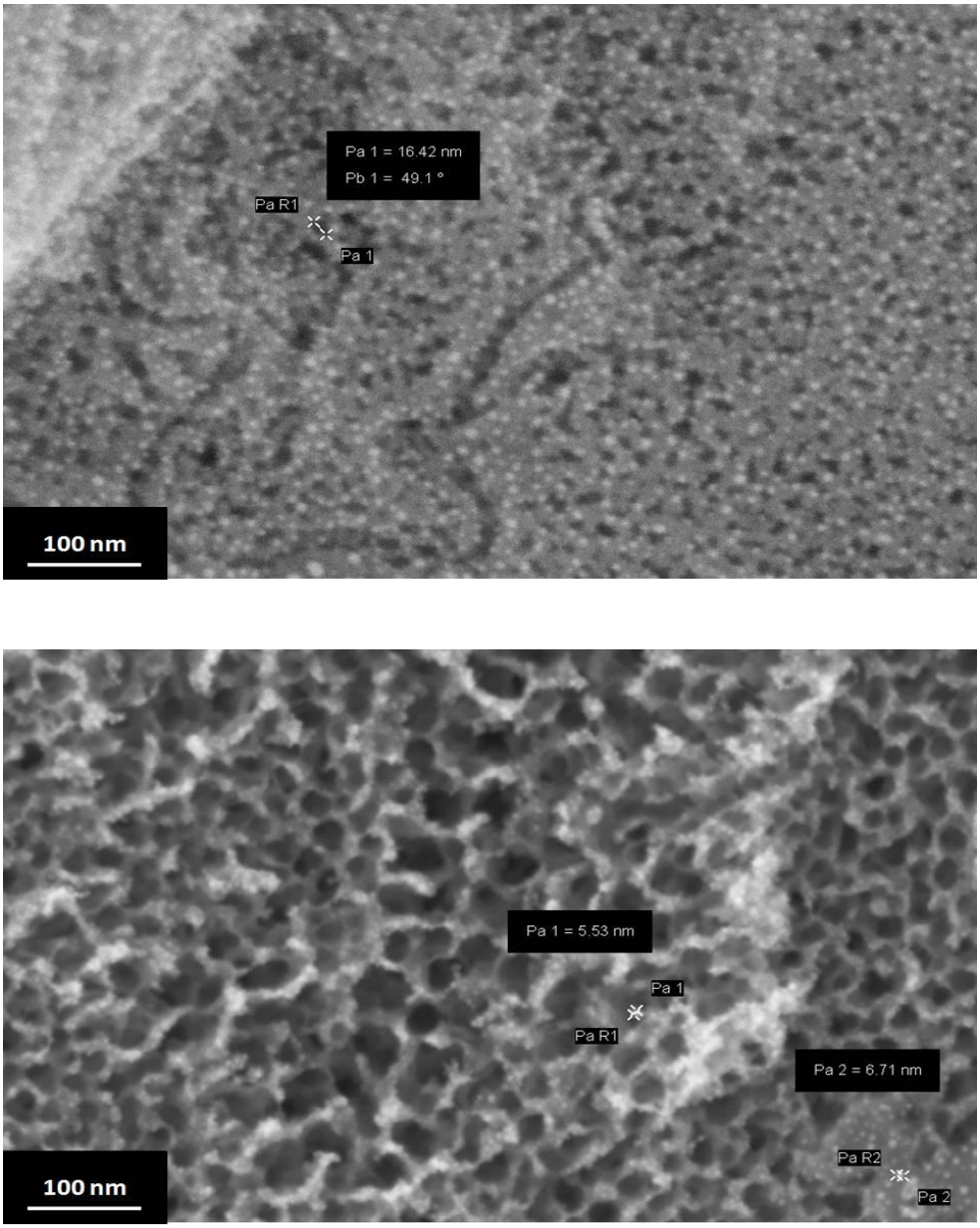

Figure 7-1: Nb_2O_5 nanopores with Au nanoparticles sputtered for 2 min at (above) 20 mA and (bottom) 10 mA.

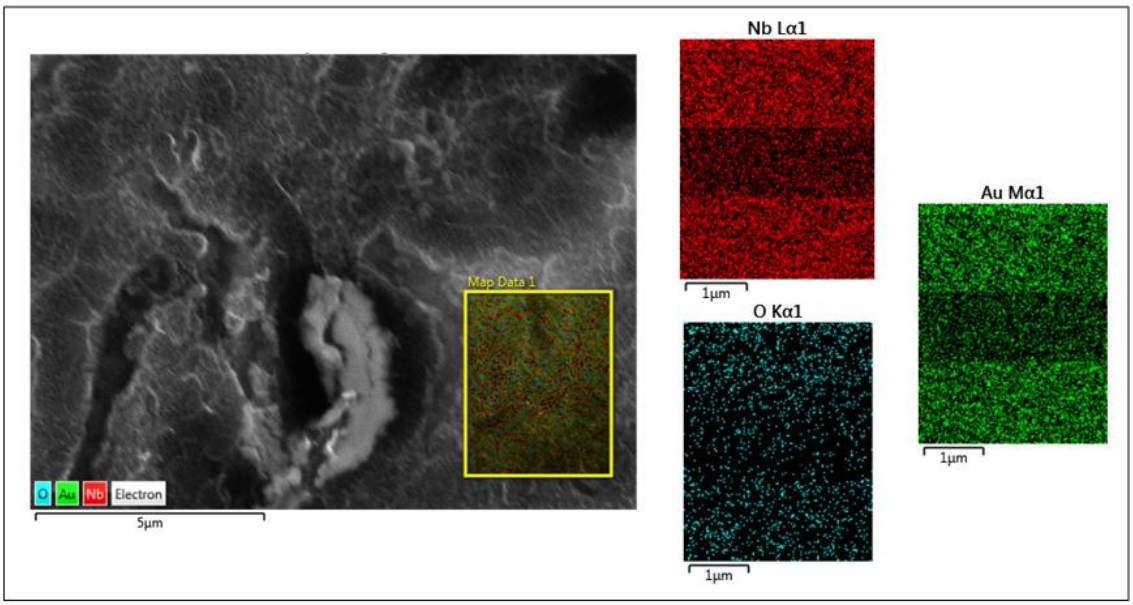

Figure 7-2: EDX spectra of Nb_2O_5 nanopores with Au nanoparticles sputtered for 2 min at 20 mA.

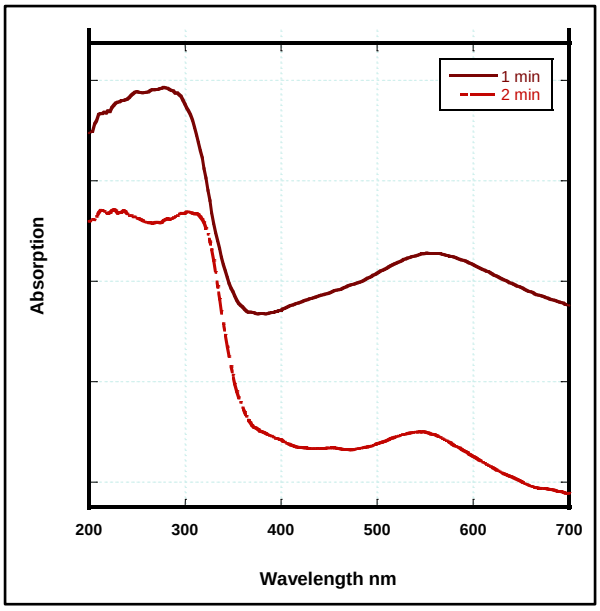

Figure 7-3: Absorption spectra of Nb_2O_5 nanopores decorated with Au nanoparticles sputtered at 20 mA for different durations.

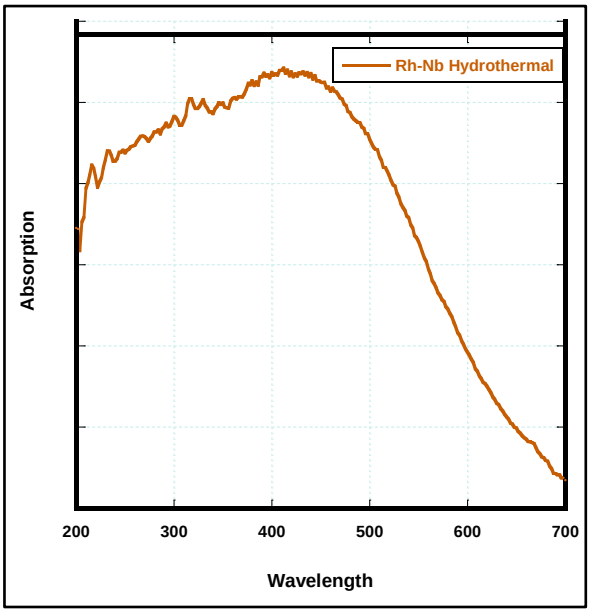

Figure 7-4: Absorption spectra of Nb_2O_5 nanopores decorated with Rh nanoparticles by anodization/ hydrothermal method.

Publications

1. Shaheen, B. S.; Salem, H. G.; El-Sayed, M. A.; Allam, N. K. Thermal/Electrochemical growth and characterization of one dimensional ZnO/TiO_2 hybrid nanoelectrodes for solar fuel production. *J. Phys. Chem C* **2013**, 117, 18502-18509.
2. Shaheen, B. S.; Salem, H. G.; Haile, S. M.; Allam, N. K. Room Temperature One-Step Electrochemical Synthesis of Crystalline Niobium Oxide Microcones. Under Submission.
3. Shaheen, B. S.; Haile, S. M.; Allam, N. K. Niobium Oxynitride Microcones with Enhanced Optical Properties. Under Preparation.